



AIAA Graduate Team Aircraft Competition 2018-2019

---

## DUCKAMPUS

### Autonomous Electric Vertical TakeOff and Landing Aircraft

---



**Duckteam**

May 2019



## Propeller

Canard: 5 telescopic blades  
Wing: 3 blades  
Cruise total thrust: 365 lbf

## Engines

(2) Magnax AXF185 on the canard  
Horsepower: 134 Hp each  
(2) Magnax AXF225 on the wing  
Horsepower: 228 Hp each



## Batteries

Energy density: 400 Wh/kg  
Total energy: 327 MJ  
Battery volume: 8 ft<sup>3</sup>  
Battery mass: 500 lb

## Dimensions

Wingspan: 32 feet  
Canardspan: 16 feet  
Length: 21 feet  
Height: 10 feet

## WEIGHTS

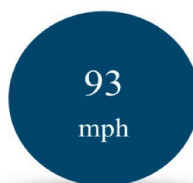
Gross equipped weight	3463 lb
Maximum useful Payload	800 lb
Maximum takeoff weight	4263 lb



Maximum Range



Maximum Cruise Speed



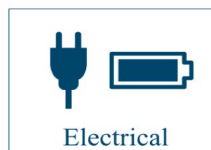
Stall Speed At cruise



Cruise Altitude





Aircraft Ceiling



# Duckteam

## Team Members :

Name	AIAA Member Number	Signature
Cawez Arnaud	977234	
Collette Axel	977232	
Cotteleer Léo	977322	
Crutzen Gilles	976904	
Delvaux Gregory	977244	
Lardinois François	977301	
Mahaudens Simon	976909	
Ranuschio Daniel	977307	



## Faculty advisors :

- Noels Ludovic
- Dimitriadis Grigorios

## Project advisors :

- Adrien Crovato
- Thomas Lambert

# Contents

<b>1</b>	<b>Introduction</b>	<b>1</b>
<b>2</b>	<b>Mission description and objectives</b>	<b>2</b>
<b>3</b>	<b>Configuration</b>	<b>3</b>
3.1	Alternative design and down-selection of concept . . . . .	3
3.2	Basic choices and technology . . . . .	4
3.2.1	Autonomous . . . . .	4
3.2.2	Aerodynamic surfaces . . . . .	5
3.2.3	Propulsion . . . . .	5
3.2.4	Tilt wing . . . . .	6
3.2.5	Telescopic blades . . . . .	6
3.3	Phases description . . . . .	7
3.4	Weight estimation . . . . .	8
3.5	Methodology . . . . .	8
3.6	Main characteristics of the Duckampus . . . . .	10
<b>4</b>	<b>Component design</b>	<b>12</b>
4.1	Propulsion and electrical systems . . . . .	12
4.1.1	Propeller design . . . . .	12
4.1.2	Engine choice . . . . .	14
4.1.3	Electrical systems . . . . .	15
4.1.4	Energy budget . . . . .	17
4.1.5	Battery . . . . .	19
4.2	Aerodynamic design . . . . .	20
4.2.1	Airfoil selection . . . . .	20
4.2.2	Dimensions of the lifting surfaces . . . . .	21
4.2.3	Battery storage - Battery integrated wing . . . . .	25
4.2.4	Fin . . . . .	25
4.3	Fuselage . . . . .	26
4.3.1	Choice of fuselage shape . . . . .	26

4.3.2	Internal layout . . . . .	27
4.3.3	Weight of the fuselage . . . . .	28
4.4	Landing gear . . . . .	29
4.4.1	Main features . . . . .	29
4.4.2	Geometric layout . . . . .	30
4.4.3	Weight . . . . .	30
4.5	Material choice . . . . .	31
4.5.1	Skins . . . . .	31
4.5.2	Frames of the aircraft . . . . .	31
4.5.3	Other components . . . . .	32
4.6	Center of gravity . . . . .	32
<b>5</b>	<b>Aircraft analysis</b>	<b>33</b>
5.1	Aerodynamics . . . . .	33
5.1.1	Statistical and Empirical drag study . . . . .	34
5.1.2	Computational fluid dynamics . . . . .	39
5.1.3	Comparison between analytical and CFD analysis . . . . .	41
5.2	Performance . . . . .	43
5.2.1	Payload-Range Diagram . . . . .	43
5.2.2	Placard Diagram . . . . .	44
5.2.3	Flight envelope . . . . .	45
5.2.4	Typical mission performance . . . . .	46
5.2.5	Point performance requirements . . . . .	47
5.3	Structure . . . . .	48
5.3.1	Maneuver envelope . . . . .	48
5.3.2	Aerodynamic and structural loads of the fuselage . . . . .	49
5.3.3	Aerodynamic loads at the wing root and at the canard root . . . . .	50
5.3.4	Structure of the aircraft . . . . .	51
5.3.5	Finite element structural analysis . . . . .	53
5.4	Static stability . . . . .	60
5.4.1	Neutral point . . . . .	60
5.4.2	Static margin estimations . . . . .	61
5.5	Dynamic stability . . . . .	61
5.5.1	Stability derivatives . . . . .	61

5.5.2	Control derivatives . . . . .	63
5.5.3	Longitudinal flying qualities . . . . .	65
5.5.4	Lateral flying qualities . . . . .	65
5.6	Transition phase . . . . .	66
5.6.1	Transition phase parameters variation . . . . .	66
5.6.2	Shaft sizing . . . . .	67
<b>6</b>	<b>Autonomous flight and navigation</b>	<b>68</b>
6.1	Safety justification . . . . .	68
6.2	Market justification . . . . .	69
6.3	Existing autonomous vehicles . . . . .	69
6.4	Level of autonomy . . . . .	69
6.5	Stabilization and piloting . . . . .	70
6.6	Navigation and guidance . . . . .	70
6.7	Takeoff and landing requirements . . . . .	70
6.8	Flight requirements . . . . .	71
6.9	Safety equipment . . . . .	71
6.10	Communication module . . . . .	71
6.11	Embedded systems . . . . .	72
6.12	Architecture . . . . .	72
<b>7</b>	<b>Trade-off study</b>	<b>72</b>
7.1	Combinations of modifications . . . . .	73
<b>8</b>	<b>Cost analysis</b>	<b>74</b>
8.1	Development and production costs . . . . .	74
8.2	Determination of a selling price . . . . .	77
8.3	Trip cost . . . . .	80
8.4	Profit analysis . . . . .	84
<b>9</b>	<b>Conclusion</b>	<b>85</b>

# Glossary

Symbol	Description	Units
AEVTOL	Autonomous Electrical Vertical TakeOff and Landing	
ODM	On-Demand Mobility	
UAM	Urban Air Mobility	
GTOW	Gross TakeOff Weight	
BEM	Blade Element Method	
DC	Direct Current	
AC	Alternative Current	
CG	Center of Gravity	
NP	Neutral Point	
GPS	Global Positioning System	
ATM	Air Traffic Management	
$P_{lost}$	Power loss in the electrical system	[W]
$\eta$	Efficiency	[-]
$E_{tot}$	Total energy consumed during sizing mission	[J]
$\alpha_0$	angle of attack leading to zero lift	[deg]
$C_{l_{max}}$	Maximum lift coefficient	[-]
$\alpha_{max}$	Angle of attack leading to maximum lift	[deg]
$C_{d_{min}}$	Minimum drag coefficient	[-]
$C_{l_{min}}$	Lift coefficient correspond to the minimum drag coefficient	[-]
$C_{D_0}$	Drag for zero-lift coefficient	[-]
AR	Aspect Ratio	[-]
$C_{L,i}$	Design-lift coefficient	[-]
$\Lambda$	Twist angle	[deg]
$\lambda$	Taper	[-]
$c_{l_\alpha}$	Two-dimensional lift coefficient slope	[deg <sup>-1</sup> ]
$C_{L_\alpha}$	Three-dimensional lift coefficient slope	[deg <sup>-1</sup> ]
$C_{L_c}$	Three-dimensional canard lift coefficient slope	[deg <sup>-1</sup> ]
$b_c$	Canard span	[ft]

<b>Symbol</b>	<b>Description</b>	<b>Units</b>
$S_c$	Canard surface	[ft <sup>2</sup> ]
$C_{L_w}$	Three-dimensional wing lift coefficient slope	[deg <sup>-1</sup> ]
$b_w$	Wing span	[ft]
$S_w$	Wing surface	[ft <sup>2</sup> ]
$V_{tot,batt}$	Available volume for battery	[ft <sup>3</sup> ]
$V_{batt}$	Needed volume of battery	[ft <sup>3</sup> ]
$b_F$	Fin span	[ft]
$c_{mean}$	Fin mean chord	[ft]
$c_{root}^F$	Fin root chord	[ft]
$c_{tip}^F$	Fin tip chord	[ft]
$S_F$	Fin surface	[ft <sup>2</sup> ]
$AR_F$	Fin aspect ratio	[-]
$\Lambda_{F,1/4}$	Fin swept angle	[deg]
$\lambda_F$	Fin taper	[-]
$F_m$	Force applied on main landing gear	[N]
$F_n$	Force applied on nose landing gear	[N]
$C_{D_J}$	Component J of drag coefficient	[-]
$C_f^{lam}$	Laminar skin friction coefficient for a flat plate	[-]
$C_f^{turb}$	Turbulent skin friction coefficient for a flat plate	[-]
$M_c$	Design cruise Mach number	[-]
$V_c$	Maximum cruise velocity	[mph]
$M_D$	Design diving Mach number	[-]
$V_{c,max}$	Max cruise velocity	[mph]
$V_{s,+}$	Cruise stall velocity	[mph]
$V_A$	Maneuvering velocity	[mph]
$V_B$	Maximum stall velocity	[mph]
$V_D$	Design diving velocity	[mph]
$n_+$	Maximum load factor	[-]
$n_-$	Minimum load factor	[-]
$n_{limit}$	Limit load factor	[-]
$n_{ultimate}$	Ultimate load factor	[-]
$A$	Boom area	[in <sup>2</sup> ]
$I_{yy}, I_{yz}, I_{zz}$	Second moment of inertia	[in <sup>4</sup> ]





# 1 Introduction

We all dream of not just flying, but moving up the city, landing on top of office buildings, getting rid of traffic jams and moving safely without constraints. Today, aviation is dedicated to worldwide connections, but tomorrow, VTOL aircraft, smaller, lighter and carrying fewer passengers, will open the perspective of intra-urban connecting flights.

Mankind is confronted with an ecological and energetic transition, with complaints about these revolutions rising all over the world. The rise of pollution in the air and climate change bring new constraints, but also new opportunities to industrial players. The transportation sector represents almost a quarter of greenhouse gas emissions and is the main cause of air pollution in cities, creating a huge need for environmentally friendly urban means of transport.

People have no more time to lose in traffic jams. Transportation experts [1] recently found that drivers are spending 164 hours a year in the congested traffic in Boston during peak time periods. The report concluded that the time and fuel wasted sitting in traffic costed the typical driver in this city over \$2,300 last year. Moreover, with the development of autonomous vehicles and general aviation, the market for Autonomous Electrical Vertical Takeoff and Landing (AEVTOL) aircraft will expand quickly in the next few years. Society changes provide new perspectives, wider than ever, to shape the future of mobility.

In this evolving context, the American Institute of Aeronautics and Astronautics launched a request for proposal for the design of an Autonomous Electrical Vertical Takeoff and Landing aircraft in the context of their Graduate Team competition. The goal is to design the flight vehicle to meet the On-Demand Mobility (ODM) or the Urban Air Mobility (UAM) concepts of operations requirements.

Featuring future-oriented technologies, such as tilt-wing, autonomous pilot, stall-proof configuration, lighter fast-charging batteries, vertical take-off and landing to reduce spatial requirements, the Duckampus will undoubtedly be the future of soft mobility, solving all the issues faced nowadays in urban mobility.

This report aims to summarize the work performed during the conceptual and preliminary design stages in the scope of the American Institute of Aeronautics and Astronautics Graduate Team competition. The first part is dedicated to the description of the sizing mission on which the design is based. Objectives and assumptions are also described in this part of the report. The EVTOL aircraft market is reviewed in the second part. Advantages and disadvantages of existing solutions are presented, as well as the justification of the design of the Duckampus. The next section





introduces new technologies that were imagined for the design of this aircraft. Moreover, the methodology of design iterations is given in details as well as the specifications of the final aircraft after convergence. CAD Models of the Duckampus are also included in this part of the report. Then, the components of the aircraft are developed in more detail including justifications of the results that are obtained in the performance section. The components include the propulsion system, propeller and engine choice, electrical system and battery associated. Aerodynamic surfaces (Canard, wing, fin), fuselage and internal layout are designed as well as the landing gear. Center of gravity computations are also described in this part of the report.

The performance of the aircraft is summarized in the next part of the report. An aerodynamic study is then performed, followed by the Placard diagram and flight envelope. Additional propulsive performances specified in the request for proposal are developed. Static and dynamic stability are then assessed and the transition phase is discussed.

Flight autonomy is then justified based on the market study and the required tools are explained. A trade-off study is carried out to justify the sizing, design features and the technologies selected to meet optimally requirements of the proposal. Finally, costs are evaluated, an optimal selling price is chosen to maximize profits and a long-term strategy is briefly mentioned.

## 2 Mission description and objectives

The design of the aircraft is based on the full payload sizing mission. Nevertheless, pitch stability is however considered with 1 to 4 passengers. Fig. 2.1 gives a schematic representation of the mission that is considered for the conceptual design stage.

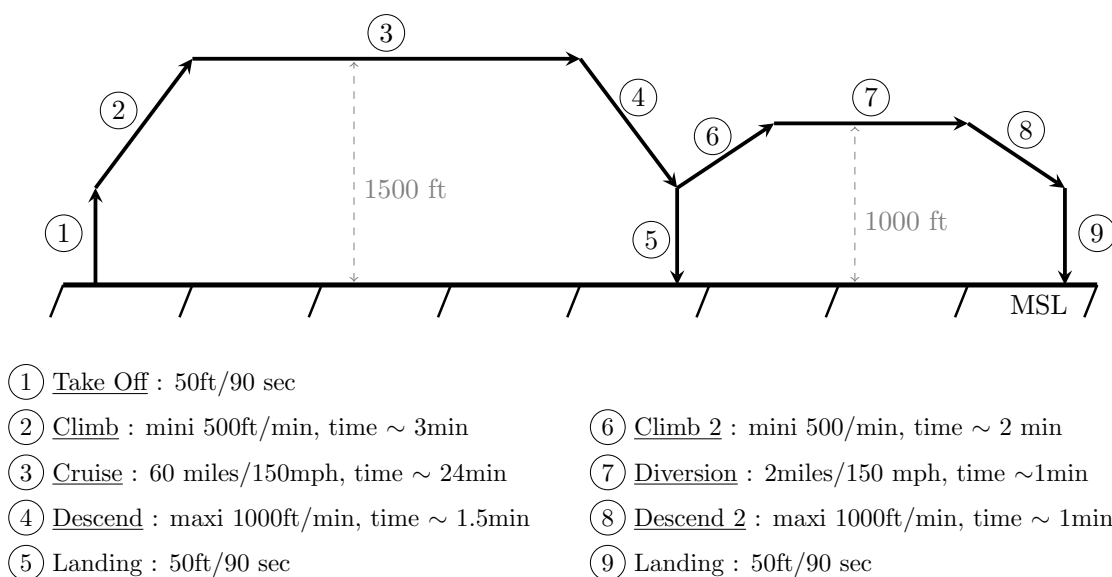


Figure 2.1: Sizing mission description.





The mission is outlined in the legend of Figure 2.1 under the following conditions : Standard atmosphere conditions (ISA+0), at sea level, zero wind speed. The technologies to be considered are those that will be available on the market in 2028, the service entry year.

For the conceptual and preliminary stages of the design, because of the symmetry of the mission, some assumptions are made. Firstly, because the average speed in the 2-4 segments is to 150 mph, the speed at each one of these segments is assumed to be equal to this value. In reality, descent may be faster than climb but it is assumed here that such differences will be averaged out. Secondly, segments 1, 5 and 9 are assumed to require the same energy. The climb-descent phase are as well computed making this assumption. In fact, since the energy required for the climb is computed exactly and the descent requires less energy, the needed energy is slightly overestimated, which contributes to the safety of the design.

In terms of airworthiness requirements, the design is carried out following regulation 14 CFR 23 [2]. The aircraft to be designed is assumed to be of Class I since it is a small light aircraft with low maneuverability. The operations performed by this EVTOL are of category B and C. Note that vertical takeoff and landings are the only phases of category C (terminal phases).

## 3 Configuration

### 3.1 Alternative design and down-selection of concept

The selection for the propulsive configuration was obviously mainly driven by the requested aircraft type, an EVTOL aircraft. This section aims to give all the configurations, technologies and basic designs that were considered during the selection of the aircraft geometry. The discussion mainly focuses on the choice of the propeller type, which represents the main feature of the design. In order to select a suitable solution for the problem, several different actual configurations were considered, and, for each, the advantages and disadvantages were identified under the constraint that the solution must be electric. To this end, three major configurations were analyzed:

- ① Several small propellers along the wing (tilt-motor).
- ② One large propeller (helicopter-like aircraft).
- ③ Two large propellers at the tip of the wing (tilt-motor) and a tilt-wing technology.



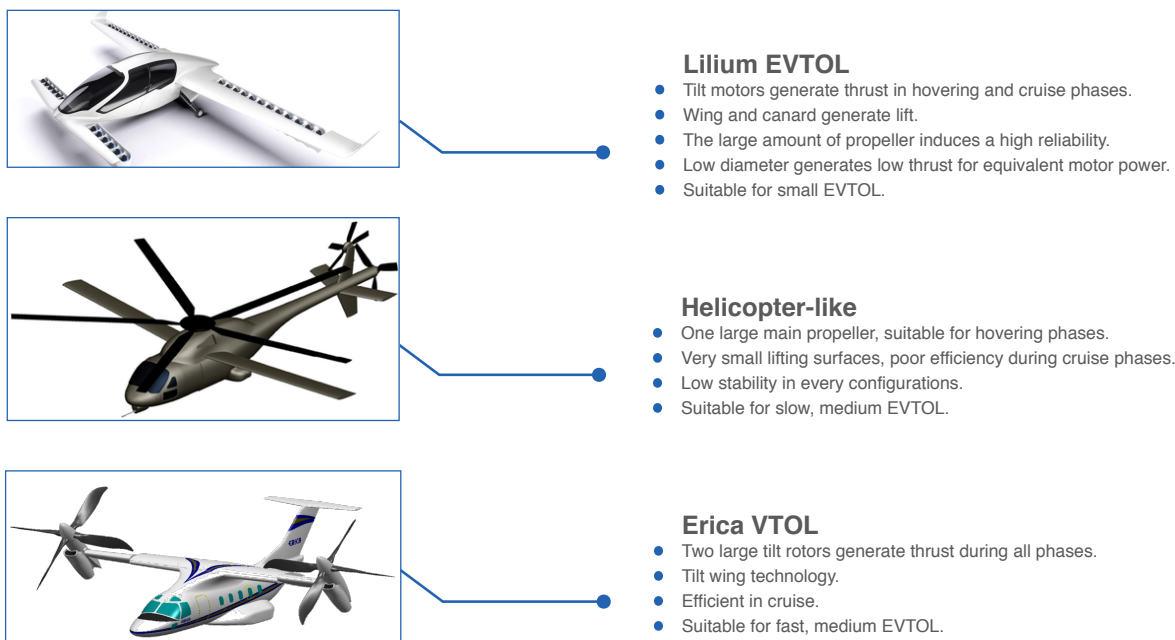


**Figure 3.1:** Configurations considered: Tilt-motor with several small propellers on the wing [3] - Helicopter-like configuration [4] - Tilt-wing with two propellers on the wing [5].

## 3.2 Basic choices and technology

The two main aspects that influence the design are the aerodynamic surfaces and the propulsion technology. In this project, the electric VTOL is chosen to be lifted by a wing-canard configuration and propelled using four large propellers. These choices are separately developed and justified. Based on these choices, the full configuration is computed using an iterative design methodology.

### 3.2.1 Autonomous

The autonomous field is nowadays in great expansion. Despite some technical issues and ethical problems, autonomous cars are currently under development and Unmanned Aerial Vehicle (UAV) are now used for military applications worldwide. The option of an autonomous aircraft is obviously retained for the Duckampus, in the context of a long term vision of mobility. During cruise, typical airliners are nowadays already highly assisted by different systems. In fact, the autopilot and the other automatic flight control system units already represent a certain level of autonomy. As will be discussed later, the only tasks that are not performed automatically are decisions. There are always humans behind the main decisions taken during the flight. In the present case, as the aircraft requires already an auto-pilot and an automatic flight control system for the take-off, landing and transition phases, the choice of an autonomous aircraft





only leads to the introduction of an additional decision center. The justification of the choice of autonomy in terms of economical and safety are discussed more extensively in Section 6.

### 3.2.2 Aerodynamic surfaces

A canard configuration is chosen in order to prevent stall. A canard configuration can be considered as stall-proofing, as the canard usually stalls before the main wing. The aircraft pitches nose-down and the angle of attack is reduced, preventing main wing stall. Another advantage of the configuration is that in stable level flight, the lift of the canard points upwards, in contrast to a downforce often generated by the conventional wing-horizontal tail configuration. This means the canard contributes to the total lift of the aircraft. Consequently, the vehicle can fly at a lower angle of attack in cruise, meaning less lift-induced drag and making the concept more efficient than conventional aircraft. A drawback of this configuration is the reduction of the downward visibility for the pilot. However, as the aircraft is autonomous, visibility is not a concern in this particular case.

### 3.2.3 Propulsion

The objectives of this section are to:

- identify and justify a propulsive configuration,
- estimate the dimensions of the main components (propellers, motors) in order to obtain a starting point for the analysis.

Since the main part of the design mission is the cruise, efficiency must be optimized for this flight phase. Thus, the chosen configuration for the propulsive system is a tilt-wing aircraft in order to allow vertical takeoff and landing, but also to have the possibility to direct the main thrust in the flight direction. The different phases are described in Section 3.3.

The main propellers are placed at the tips of the wing. As it is developed in Section 3.2.4, these propellers can be tilted, along with a section of the wing, during the transition phase and are the only components providing thrust for the entire mission. Since the aircraft has a canard configuration, two propellers are also placed at the tips of the canard. After the initial hovering phase, the primary propellers are tilted together with part of the wing to guarantee a cleaner flow and thus more thrust. In the meantime, the canard propellers are retracted to minimize the drag during other phases. This solution is chosen in order to guarantee higher controllability and safety during the hover and transition phases in which the system is arranged as in a multicopter.

Another advantage of having four propellers during the hovering phase is that the load can be divided between them.





This allows the choice of smaller primary propellers and thus the reduction of the load during the tilting phase, resulting in a decrease in the overall weight of the system.

### 3.2.4 Tilt wing

According to the mission requirements, different flight configurations have to be fulfilled. During the lift-off, the design of the plane has to reach the required vertical propulsion linked to the weight while during the cruise the horizontal one has to be sufficient to reach the required velocity as specified in the request for proposals. To that end, four propellers are considered. The rear propellers are able to rotate in the aim of providing a vertical/horizontal propulsion for the lift-off/cruise respectively while the front propellers are only used for vertical propulsion. It is thus important to select an appropriate technology in order to tilt the propulsion vector of the rear engines. The tilt wing is chosen for the following reasons.

Conventional tilt rotors rotate the engine nacelles at the wingtips, so that the rotors are horizontal during hover. This means that a significant part of the rotors' downwash is blocked by the wing, thus reducing the effect diameter of the rotors and, hence, their thrust. By rotating a section of the wing along with the nacelle, this effect is strongly reduced. Approximately half of the wing is rotated by means of the wing spar, which is circular and is rotated by motors placed inside the fuselage. A graphical representation of this is given in the section dedicated to the final configuration. A comparison with the "Erica Tiltwing Aircraft" [5] can be realized. The structure of the rotating part of the Duckampus has been inspired by this aircraft. From the calculation of the shaft size and the consideration of the whole rotation system, a final mass of 440 lb is found. The transition phase is analyzed in Section 5.6.

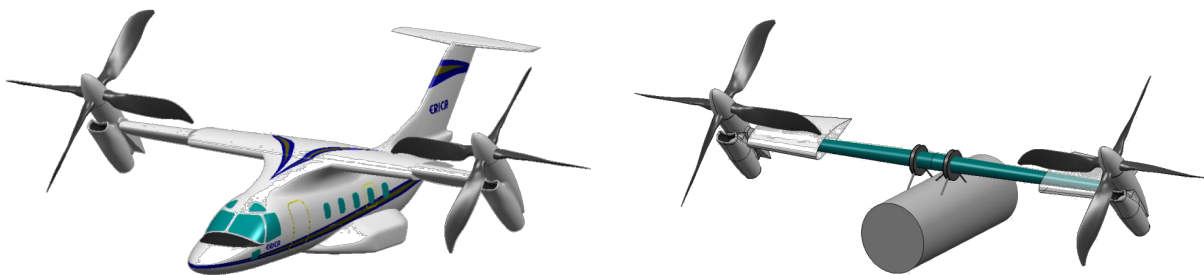


**Figure 3.2:** Example of the "Erica Tiltwing Aircraft" [5].

### 3.2.5 Telescopic blades

Given that the front propellers are a source of flow perturbation in forward flight, they have to be designed carefully. Since the front motors are not used during cruise, a solution must be found to reduce their drag. To this end, a variable diameter propeller technology is considered. This design is based upon telescopic blades which are deployed/folded up





under the effect of the centrifugal/centripetal force generated by a rotating motor [6] [7]. The following section aims at explaining this choice and provides details on the geometry.

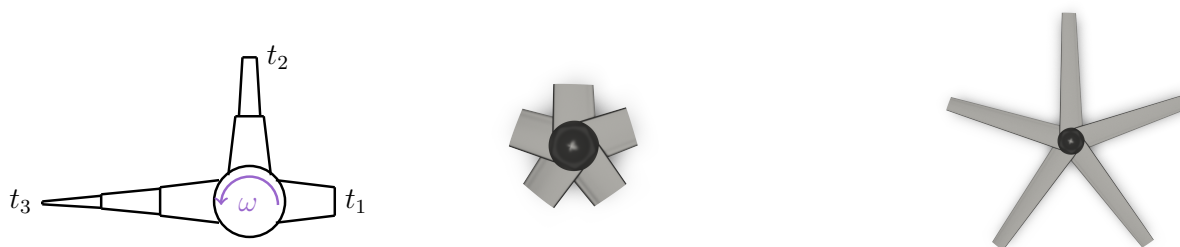


**Figure 3.3:** Scheme of a telescopic blade behaviour and representation of the actual telescopic blades (retracted and extended configurations).

The central device of the system is a rotating circular motor of angular speed  $\omega$  and different times  $t_1$ ,  $t_2$  and  $t_3$  are depicted schematically in Fig. 3.3. Illustrations of the actual telescopic blades in the retracted and deployed configuration are also given in this figure. The blade is made up of three sections which fit inside each other when retracted. A spring provides a restoring force such that the blade is retracted when the motor is at rest. When the motor rotates, the centrifugal force acting on sections 2 and 3 is higher than the spring restoring force, forcing them to deploy. Once the lift-off phase is ended, the motor stops to turn and the blades go back to their initial position, i.e inside the circular part. This system allows the aircraft to lift off vertically while avoiding flow perturbations due to the front propellers in cruise.

A study of the different options for telescopic blades and their respective performance was performed by the "United Aircraft Corporation" in 1973 [8]. By considering models as shown in Fig. 3.3, it turns out that this technology is really feasible and that it does not increase significantly the gross weight of the aircraft. Vibration and resonance issues are not problematic if taken into account in the design process. Currently, this technology is already used for gliders. It should be noted that telescopic blades impose a major constraint on the blade shape: the blade profile should be uniform and there should be no twist.

### 3.3 Phases description

The typical sequence of phases is described in this section. Before takeoff, the Duckampus is in hovering configuration but with retracted telescopic blades since the front motors are not rotating. The takeoff and landing phases are performed in the hovering configuration with the front propellers out. The rotating wing is oriented vertically and all four propellers are used. At cruise, only the back motors are used. During the transition from takeoff to climb, the rotating part of the wing is tilted horizontally to the cruise configuration. As the aircraft is accelerating, the lift increases and the required thrust of the front motors decreases. The front motors rotation speed decreases and the telescopic blades are slowly





retracted. They are staying in this retracted configuration during cruise since the front motor are completely shut down. As the aircraft is at its landing location, the front motors are put back on and the telescopic blades are extending until hovering configuration is reached. The last phase, the landing one, can then be performed in this last configuration. When the aircraft has landed safely, all motors are shut down and the front propeller are again retracted.

### 3.4 Weight estimation

In order to estimate an initial weight for the first iteration of the design loop, a significant number of existing EVTOL concepts have been compared. Fig. 3.4 represents the market review in terms of maximum takeoff weight and number of passengers. Note that in case of a non-autonomous aircraft, the pilot has been considered as a passenger.

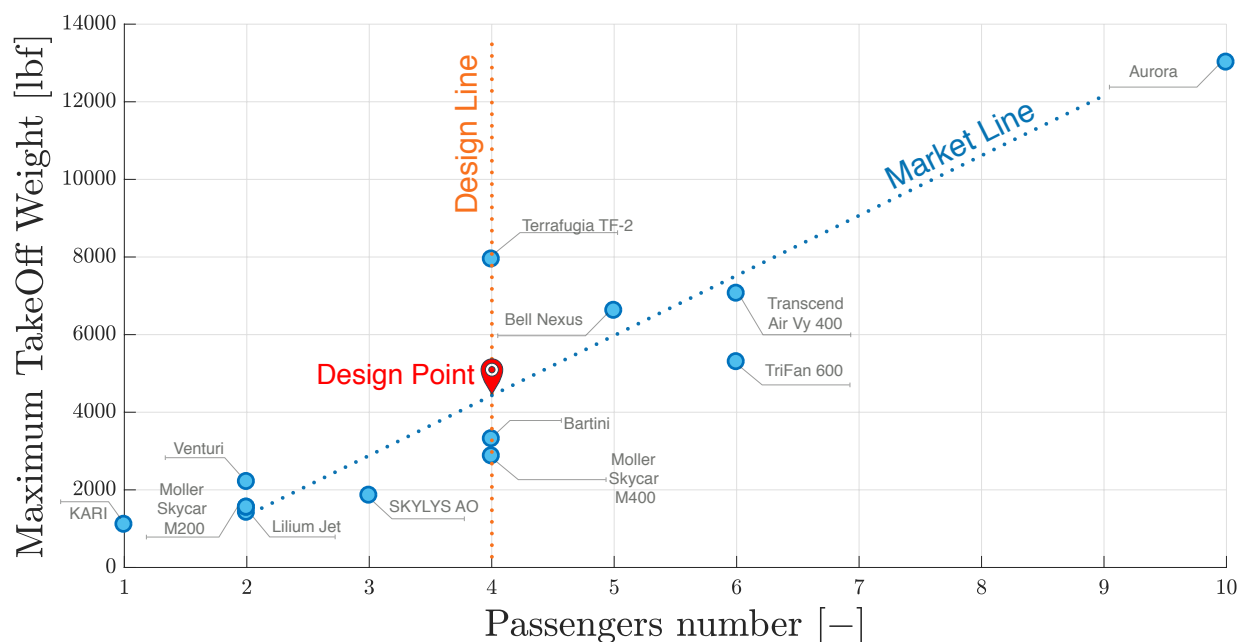


Figure 3.4: Design point estimation for initial loop weight value.

From Fig. 3.4, the initial weight has been estimated to approximately 4,500 lbf. This value was thus used as first basis for the choices of all the aircraft components.

### 3.5 Methodology

First, a series of design iterations for the aircraft mass was carried out in order to perform a so-called "One point optimization" in cruise. A representation of this design methodology is shown in Fig. 3.5. Starting from the given information of the "sizing mission" and taking all the considered technology into account as well as the initial conditions, the Gross TakeOff Weight (GTOW) is first estimated. The aerodynamic function calculates the characteristics of the







wing and the canard so that the lift is equal to the estimated weight. The drag is then computed and the aerodynamic loads are sent to the propulsion function. Since the motors are an input of the code, the propulsion function needs to ensure that sufficient power is generated during all flight phases. Moreover, this function also computes the battery mass required for the entire sizing mission.

The total mass is finally computed considering all aircraft components separately. If this new mass estimate is very similar to the estimate from the previous design iteration, then the design process has converged. The center of gravity can be obtained and the stability can be computed. If the mass difference is too large, other iterations are performed until convergence. The tolerance used for the convergence of the weight is fixed to 0.25 lbf.

The performance computation stage includes the generation of the payload diagram, the Placard diagram, the gust envelope and energy consumption per flight segment.

As a reminder, stability and the performance are observed outside of the design loop and the required changes are carried out manually in order to retain some control of the design process. Among the different changes that can be made, there are the geometry modification and the choice of the input characteristics of each aircraft component. Once the performance is judged to be appropriate, the outputs are displayed and graphs are plotted.

Once this first conceptual stage is completed, a full analysis of the aircraft is carried out during the preliminary design stage. The aerodynamics, the structure as well as the propeller are analyzed during this phase. Furthermore, the performance and the stability of the aircraft are studied in a more extensive way.

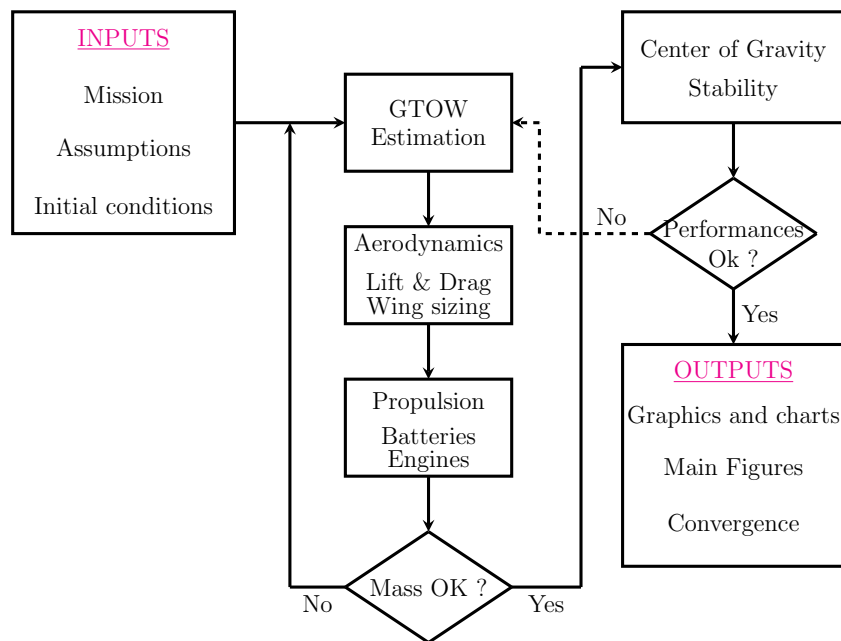


Figure 3.5: Flowchart of the MATLAB loop methodology. Adapted from [9].





### 3.6 Main characteristics of the Duckampus

A graphical representation of the Duckampus with the main dimensions [ft] is given in Fig. 3.6, 3.7, 3.8 and 3.9.

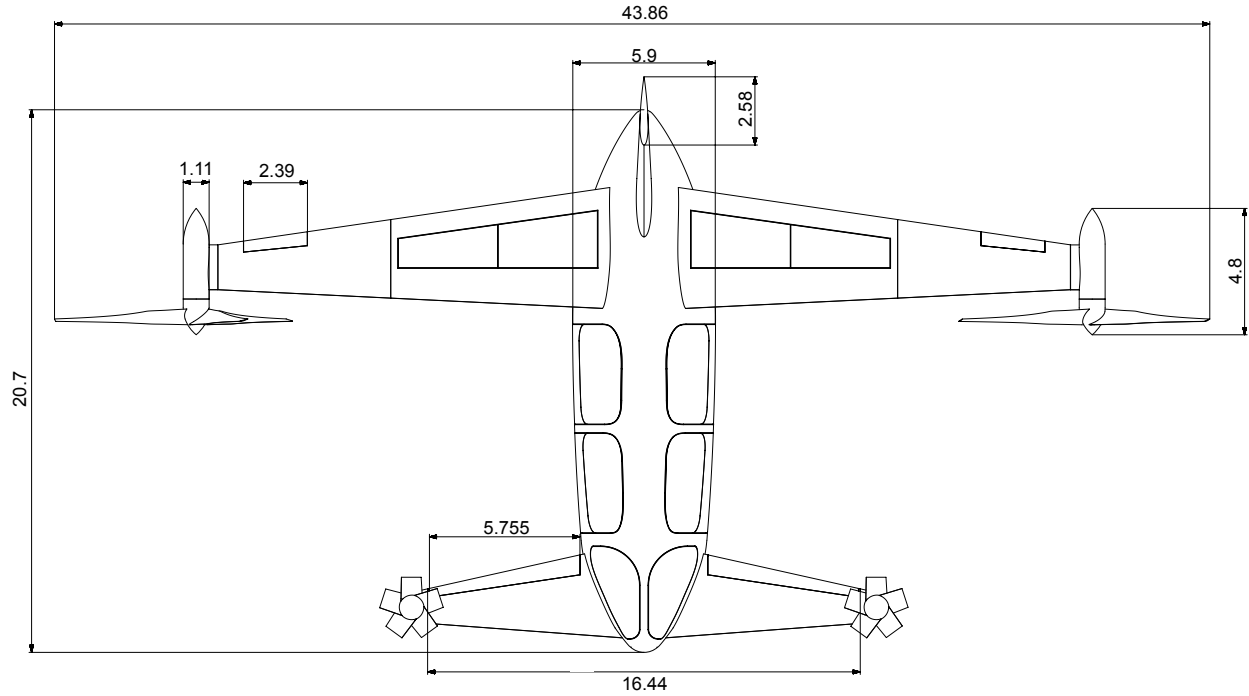


Figure 3.6: Top view of the aircraft - Cruise configuration - [ft].

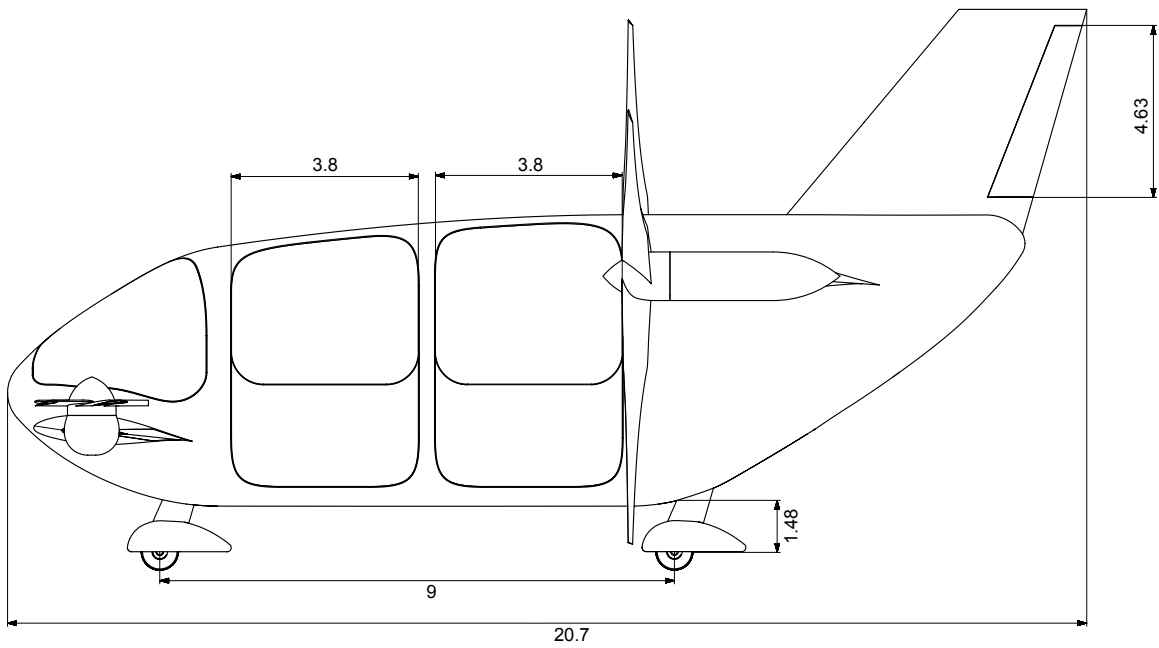
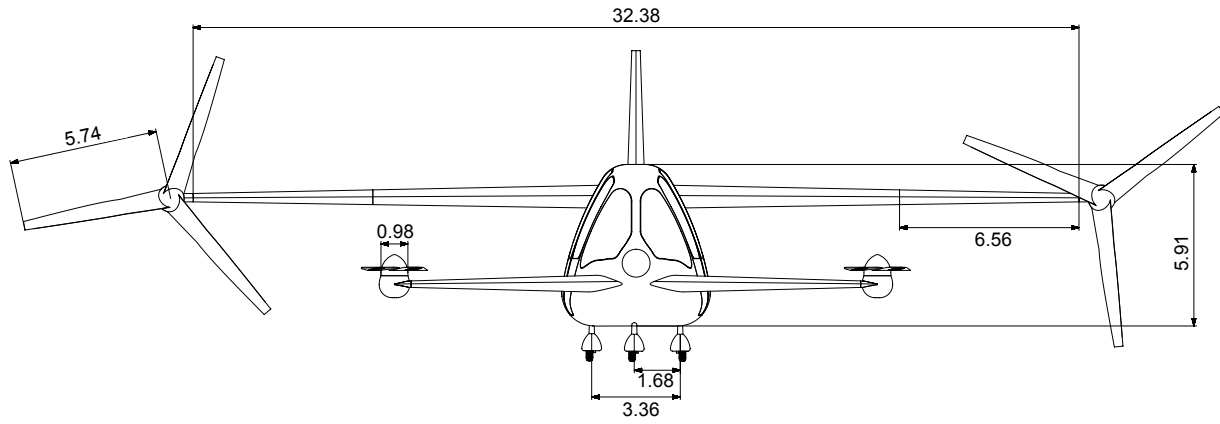
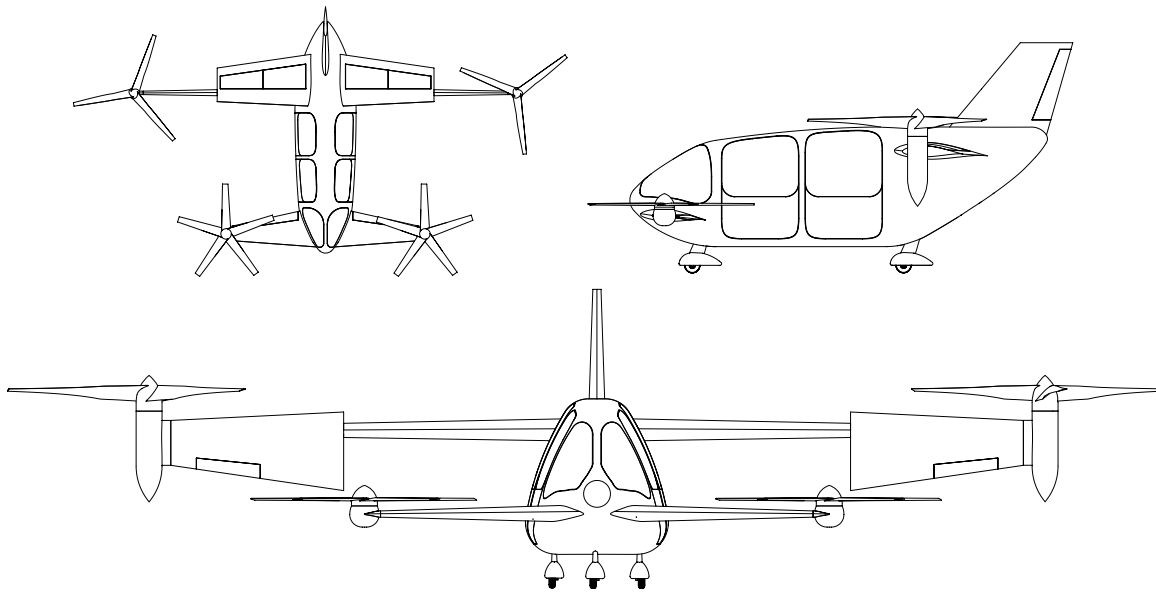


Figure 3.7: Right view of the aircraft - Cruise configuration - [ft].





**Figure 3.8:** Front view of the aircraft - Cruise configuration - [ft].



**Figure 3.9:** Top, right and front views of the aircraft - Takeoff configuration.

The main numerical characteristics of the aircraft are given in Table 3.1.

Variable	Numerical value	Variable	Numerical value
Wing span	32.4 ft	Length of the plane	20.7 ft
Canard span	16.5 ft	Diameter front propeller	8.20 ft
Wing surface	116.57 ft <sup>2</sup>	Diameter back propeller	11.48 ft
Canard surface	45 ft <sup>2</sup>	Maximum propulsive power	342, 523 W

**Table 3.1:** Summary of main numerical characteristics of the aircraft.





## 4 Component design

The chosen design configuration of the Duckampus involves then two main propellers fixed on the wing and the smaller ones fixed on the canard. This section aims at detailing the different components of the aircraft, starting with the propulsion system and the electric systems. Then, the design of the two lifting surfaces, the fuselage and the landing gear are discussed. Finally, the selected materials are discussed and the position of the center of gravity is calculated.

### 4.1 Propulsion and electrical systems

The design of the propulsion and electrical systems involves different components, namely: the propellers, the engines, the electric devices and finally the batteries. They are sized and justified in the following sub-sections. Every computation is based on the blade element momentum theory (BEM) which permits to compute the thrust, the power and the torque for different propeller configurations. In particular each blade is dividend into  $n$  elements along its span and for each of them the angle of attack is computed from the free stream airspeed, the local pitch angle and the rotation speed. It is then possible, knowing the aerodynamic characteristics ( $C_L(\alpha)$  and  $C_D(\alpha)$ ) of each element, to compute the generated lift and drag for each element. These are then projected on the propeller plane and perpendicular to it and integrated over the entire span to retrieve respectively the torque and the thrust of the single blade. Multiplying this times the number of plates gives the total thrust and torque. To obtain the power, the torque is multiplied by the rotation speed.

#### 4.1.1 Propeller design

Since the propulsion system has to be efficient during cruise while providing enough thrust for vertical takeoff, the design of the propeller is adapted to both these phases. The airfoil selection for each section of the blades is mainly driven by the local Mach number and the local angle of attack. Therefore, two different profiles have been chosen for the main propellers. The first 40% of the blade corresponds to a NACA 4412 airfoil, the lift and drag coefficients in function of the angle of attack and Mach number were digitalized from the appendix in "Introduction to flight" [10], in order to avoid stall and reduce drag at highly negative angles of attack which are reached during cruise near the blade root. As far as the external part of the blade is concerned, the NACA 16-709 airfoil is chosen because it is suitable for higher Mach number [11]. In fact, this aspect is very important during takeoff where in order to generate enough thrust high rotation speeds are required generating as a consequence higher Mach regions at the external part of the tips.

Subsequently, the blades shape is optimized fixing the ranges for the blade number, tip chord and collective pitch to realistic values. Then the power is computed for all the possible combinations of the characteristics, until an optimal value for the power is reached, while ensuring that enough thrust is produced (Tab. 4.1). The wing propellers are





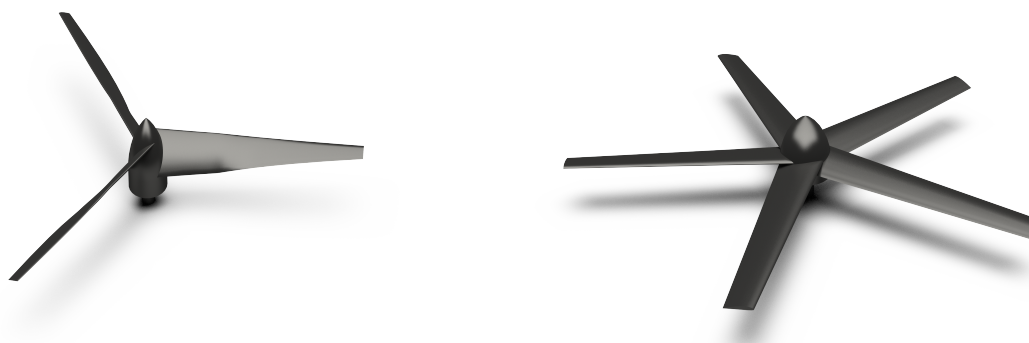
optimized for cruise while the canard propellers are optimized for the hover phase.

	Wing Propeller	Canard Propeller
Blade number	3	5
Propeller diameter	11.48 ft	8.20 ft
Ogive diameter	13.39 in	11.81 in
Root chord	11.81 in	9.84 in
Tip chord	6.69 in	5.91 in
Twist	Constant for the first 31% at 39.8° then decreases exponentially until 15° at the tip	No twist
Collective pitch	Variable between -12° during hover phase and 30° during cruise	7°
Rotation speed	1082 rpm during takeoff and 396 rpm during cruise	1036 rpm
Torque	650.5 ft·lbf during takeoff and 972.1 ft·lbf during cruise	175.5 ft·lbf

**Table 4.1:** Main characteristics of the propellers for the wing and the canard.

Finally, due to the retractable blades technology used for the canard propellers, the blades have no twist and only one profile, the NACA 16-709, is chosen (Fig. 4.1b). For the main propellers, it is necessary to install variable pitch blades since the operating regimes are too different (Fig. 4.1a). In particular, during takeoff, the collective pitch is set around  $-12^\circ$  while during cruise, it is set around  $30^\circ$  (these values come from the optimization). In fact during all mission phases both the collective pitch and the rotation speed are regulated in function of the free stream airspeed thanks to a close loop control in order to obtain  $\eta_{prop} = 0.86$  [12].





(a) Wing propeller.

(b) Canard propeller.

Figure 4.1: CAD model of the propellers (not to scale).

## 4.1.2 Engine choice

The driving point for the selection of the motors is the power density. This allows to reduce as much as possible the weight but also the dimensions of the engines themselves. Indeed, for the canard it is fundamental to reduce the axial dimensions since the engines are mounted with their rotational axis in the vertical direction. Thus a short motor decreases dramatically the drag during flight. The wing motor must be as small and light as possible in order to diminish the inertia which has to be overcome during the rotation of the wing and the propeller for the transition. Finally, the selected motor is the Magnax AXF185 for the canard and the Magnax AXF225 [13] for the wing. The main mechanical and electrical characteristics of these engines are available in the Table 4.2.

	AXF185	AXF225
Max. rpm	12,000	10,000
Diameter	7.28 in	8.86 in
Length	2.95 in	3.39 in
Weight	17.6 lb	30.9 lb
Peak power	100 kW	170 kW
Nominal power	50 kW	85 kW
Peak torque	73.8 ft·lbf	184.4 ft·lbf
Nominal torque	36.9 ft·lbf	98.1 ft·lbf
Nominal efficiency	95%	95%
Voltage	400/750 V	750 V

Table 4.2: MAGNAX motor specifications [14].





Analyzing the results of the BEM code, the use of gearboxes is mandatory for the wing as well as for the canard. In fact, the maximum output torque of the motors is 73.76 ft·lb for the AXF185 and 184.39 ft·lb for the AXF225. By comparison, the maximum torque that has to be applied to the shaft is around 175 ft·lbf on the front propellers and around 972 ft·lbf on the main propellers during cruise. This leads to the choice of a gearbox with a ratio of 3 for the front propellers and a gearbox with a ratio of 6 for the main propellers. Comparable gearboxes (GSB120 and GSB180) are already produced by FramoMorat and are capable of transferring the required torque and work at the desired input and output rotation speeds while assuring relatively low weight (31.5 lb and 62.4 lb) and dimensions. More detailed information is available on the manufacturer's website [15].

### 4.1.3 Electrical systems

In the aim of reducing as much as possible the weight and the losses through the transfer of energy high voltage levels are desirable. Indeed, higher voltage means lower current. As a consequence, it allows to select a smaller cable section area for the power transmission and the reduction of the weight. In addition, the losses are diminished since the power lost due to the Joule effect can be computed as  $P_{\text{lost}} = RI^2$  where  $R$  is the resistance of the line and  $I$  is the current. This shows that a reduction of the current has a greater impact than the reduction of the section area on the losses.

The input voltage of 750 V is suitable for both selected motors (Tab. 4.2). This value is considered as optimal since it is the nominal voltage of the two motors. Moreover, the latter is high enough to reduce significantly the current in each line, which is very important for reducing losses, as discussed earlier and recommended by C. Jung [16]. However, the voltage must be kept below 1 kV in order to avoid the necessity to install special types of insulation. Then, the inverter is selected appropriately since it is the driving component for all the motors. The inverter converts DC current from the batteries into AC (variable frequency) three phase current, allowing the variation of the rotation speed of the motor and thus the produced thrust thanks to the integrated controller. Looking at high performance solutions, such as, the ones used in the Formula E championships, it is possible to reach  $\eta_{\text{inverter}} = 0.99$  for systems with extremely high power density. The power density is assumed to be 11 kW/lb [17]. This value can be obtained only by employing SiC-based MOSFET inverters which, at high voltage, give better performance and at the same time gives lower switching and conduction losses. Furthermore, they enable to switch faster which results in cleaner output current and voltage levels [18] with respect to their Si-based counterparts.

Since each motor has to be controlled independently and because the control electronics for the motor is integrated in the inverter, it is mandatory to utilize four inverters : one for each motor. They are located as close as possible to the motor (the reason will be explained in the following paragraph). Looking at the maximum power needed by each motor and the assumed power density, it is possible to estimate the weight of the inverter for the motors placed on the canard to 2.7 lb and for the motors on the wing to 10 lb.





The power is distributed through DC lines in order to decrease the copper losses. In fact, distributing the power in AC would cause higher losses due to the high frequency needed for driving the motors. Due to the proximity and the skin effects, the current is not distributed evenly inside the cables resulting in high current-density regions with higher losses.

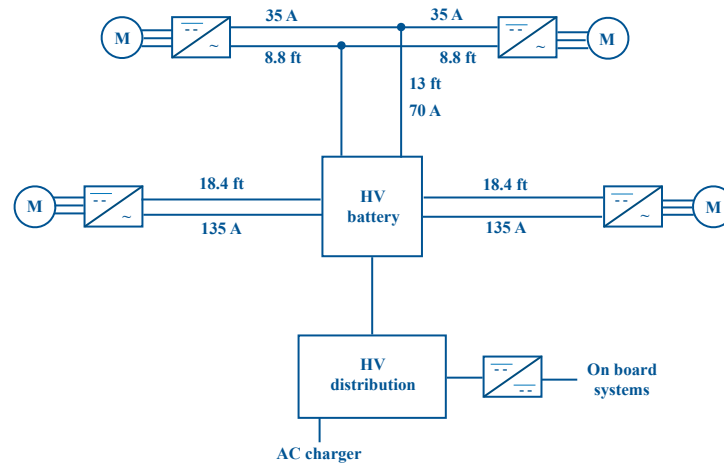


Figure 4.2: Electrical system schematic.

The layout and the features of the power distribution system are depicted in Fig. 4.2. According to C. Jung [16], it is possible to estimate suitable cross-sections (Tab. 4.3) for the cables by using the maximum current which passes through them. Note that the diameter considers only the copper core and not the insulation which composes the majority of the diameter due to the high voltage. The efficiency of the transmission can be easily computed from [19]

$$\eta_{cable} = 100 - \frac{200\rho lP}{SV^2} \quad (1)$$

where  $\rho$  is the resistivity of copper,  $l$  the length of the line (half of the cable length),  $P$  the power that has to be transmitted,  $S$  the cross section of the cable and  $V$  the voltage. Given the extremely high voltage level, the size of the cable and the short length, it can be observed that the losses on all parts of the line are much less than 1% and thus they can be neglected in the power computation.

Current	Diameter	Total weight [20]
135 A	0.26 in	18.3 lb
70 A	0.22 in	4.9 lb
35 A	0.18 in	4.6 lb

Table 4.3: Cable dimensions.







## 4.1.4 Energy budget

In addition to the standard mission, it is also important to consider the energy for emergency situations. These are stated in the proposal and consist in a reclimb to an altitude of 1000 ft MSL after interrupting the final hovering phase at 50 ft. Then, the cruise to another landing zone at a maximum distance of 2 statute miles and the final descent into the hovering phase must also be taken into account. On top of that, an extra 10 % of the energy needed for the sizing mission has to be added in order to account for the fact that the batteries will be charged only to 90 % of their capacity to avoid damage.

The power required for vertical climb and hovering can again be computed after dividing the required thrust between the four propellers in order to guarantee the rotational equilibrium around the pitch and the roll axes. The total thrust is equal to the weight of the aircraft plus a constant component in order to achieve a constant vertical acceleration. After convergence of the weight of the aircraft at a value of 4,263.1 lbf, the thrust for the primary propeller is around 1,518 lbf each. The secondary propellers are loaded with 618.2 lbf each. These values allow the computation of the propulsive power  $P$  through the BEM code. This power is integrated during the entire hovering phase since it depends on the free stream airspeed which varies continuously.

In order to compute the power for the climbing phase, making the assumption that the vertical speed is 500 ft/min and the speed along the path is 150 mph, it is necessary to evaluate vertical and horizontal equilibrium. From this equilibrium it is possible to evaluate the required thrust and thanks to the BEM code the required power. It is assumed that the velocity during the climb remains constant and thus the thrust and the required power are also constant. This allows to simplify the computation of the total consumed energy.

The power required for cruise can be computed from BEM analysis and is considered constant since the velocity is also constant. The correct rotational speed of the propellers is computed iteratively until the generated thrust is high enough to balance the drag, the collective pitch is set around the value obtained from the optimization. Knowing the desired cruise velocity and the required total distance to be covered, the duration of the cruise can be easily computed. It also simplifies the computation of the total consumed energy.

The powers computed during the BEM analysis are propulsive powers. This means that before computing the energy, it is necessary to transform them into electrical power by considering the aerodynamic losses, the mechanical losses and the electrical losses. This is done by considering the propulsive efficiency  $\eta_{prop} = 0.86$  and the electromechanical efficiency  $\eta_{em} = \eta_{motor} \eta_{gearbox} \eta_{inverter} \eta_{cables}$ , where  $\eta_{motor} = 0.95$  (see Table 4.2),  $\eta_{gearbox} = 0.98$  (see [15]),  $\eta_{inverter} = 0.99$  and  $\eta_{cable} = 1$ .





The total power consumed during the sizing mission can be computed as following

$$E_{tot} = \sum_{n=1}^9 \left( \int_{t_n} P_n(t) dt \right) \tag{2}$$

where  $n$  identifies the different phases of the mission. Note that the mission is considered as "symmetrical". This means that the mean power and the consumed energy are assumed to be the same during the descending and the climbing phases.

This results in the total consumption of 297 MJ, its breakdown in the different phases can be seen in Fig. 4.3. After adding the 10% margin the total amount of energy for which the battery will be sized is 326.7 MJ.

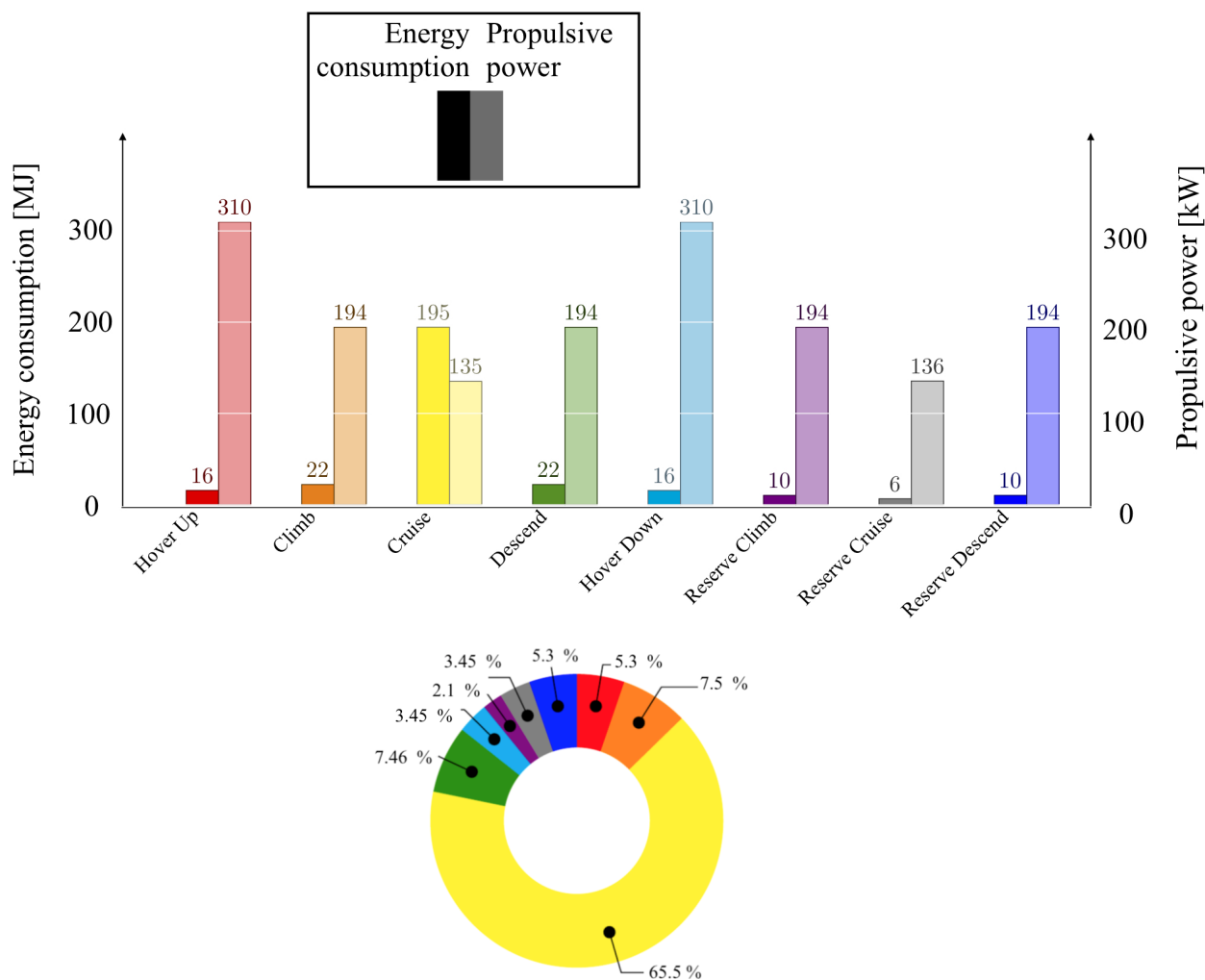


Figure 4.3: Energy budget.

It can be observed that the majority of the energy, over 60 %, is required for the cruise phase. This underlines the importance of optimizing the propellers mounted on the wing for this phase and not for the hovering phase.





## 4.1.5 Battery

Another component which has to be carefully chosen for an electric aircraft is obviously the battery. Many different technologies are available but they are not all suited for this type of use. Thereby, it is very important to maximize the gravimetric and volumetric energy density in order to minimize the batteries' mass and size.

Looking at Fig. 4.4, it is decided to utilize a Lithium-Sulfur battery which is already available, because this technology is characterized by very good specifications [21].

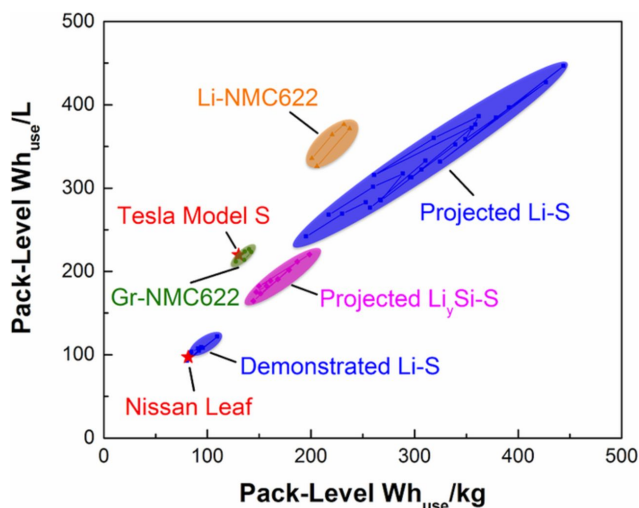


Figure 4.4: Battery technology [21].

In the scope of the design, the gravimetric energy density is assumed to be 82.28 Wh/lb while the volumetric energy density is assumed to be 11.3 kWh/ft<sup>3</sup>. This technology guarantees extremely high energy density with respect to conventional Lithium-Ion technologies. Finally, the total mass and total volume occupied by the batteries are estimated as 500.1 lb and 8.01 ft<sup>3</sup>, respectively.

After computing the weight, it is essential to investigate the maximum power that can be requested by the system to the batteries. Consequently, the batteries must be capable of generating around 300 kW during the hovering phase without overheating or being damaged. According to Nagata Hiroshi and Chikusa Yasuo [22], power densities can reach values around 5,000 W/lb. However, this limit is not a problem. In fact, by looking at the battery mass installed, it is clear that the limit is not reached, since it is sufficient to have 760 W/lb to produce enough power (this value is also in line with the maximum values for the energy density given by the request for proposal).

Finally, the life duration of this type of batteries will be discussed. In particular Li-S suffer from extreme capacity fading due to the dissolution of lithium polysulfides. This leads to a loss of 20 % of the capacity after only 180 cycles (in a controlled environment)[23]. This problem can be mitigated by encapsulating the lithium polysulfides with anthraquinone, an organic molecule. It prevents the dissolution and extends the battery life guaranteeing a low capacity decay of 0.019% per cycle for 300 cycles and retention of 81.7 % over 500 cycles [24]. Thus, the life of the battery





is expected to be around 500 cycles considering a retention of 80% of the capacity as the limit. This value is actually lower than for Li-ion batteries and could cause extreme costs. However, thanks to the abundance of S in nature, their cost is much lower [23], in fact Li-S are expected to cost 100 \$/kWh.

## 4.2 Aerodynamic design

### 4.2.1 Airfoil selection

The total mass obtained for the battery and control system is about approximately 500 lb. This important quantity of devices must be stocked while ensuring the aircraft's stability. This storage can be achieved using a battery-integrated wing configuration. As the wing is tilted at half-span, the available volume inside the wing is drastically reduced. Therefore, the choice of the airfoil is directly influenced by its aerodynamic characteristics. The volume needed for the battery storage is such that thick airfoils are selected.

According to Hoerner [25], the NACA 6-series are characterized by a relatively high maximum lift coefficient and low minimum drag coefficient while sustaining extensive laminar flow. This kind of airfoil is thus considered and the final selection is made according to the aerodynamic characteristics. The different aerodynamic parameters which are studied are the zero lift angle of attack ( $\alpha_0$ ), the maximum lift coefficient ( $c_{l_{max}}$ ) as well as the corresponding angle of attack ( $\alpha_{max}$ ), the minimum drag coefficient ( $c_{d_{min}}$ ), the corresponding lift coefficient ( $c_{l_{d_{min}}}$ ) and finally the maximum lift-to-drag ratio. The analysis results to the selection of the NACA 64(3)-418 airfoil.

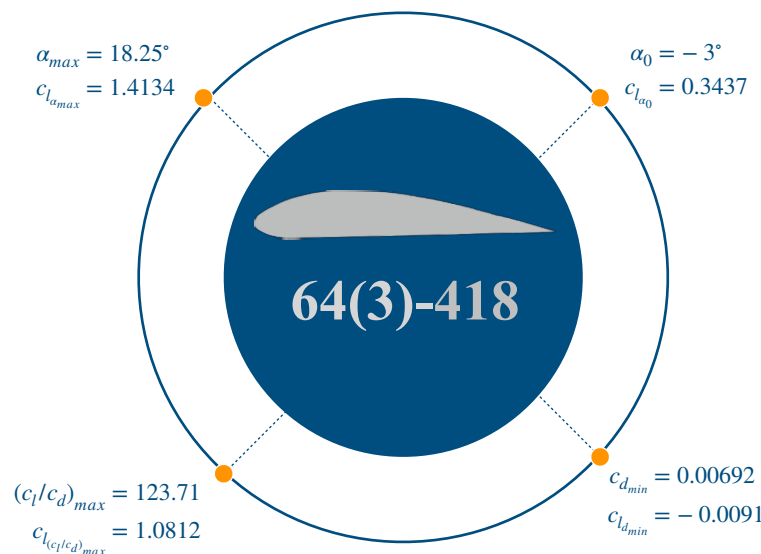


Figure 4.5: Aerodynamic parameters of the NACA 64(3)-418 airfoil.





## 4.2.2 Dimensions of the lifting surfaces

The Duckampus is constituted of two different lifting surfaces, a wing and a canard. To maximize the performance of the airplane during cruise, 70 % of the lift is produced by the wing while the remaining 30 % is produced by the canard. This weighting is a key choice for the design and is further examined in the trade-off study (Section 7). It is assumed that the lift is generated exclusively by the wing and canard. Fuselage may also generate some lift, but it is assumed to be negligible in comparison to the influence of the wing and canard.

The calculation of the geometric dimensions of the lifting surfaces are carried out following the flowchart in Fig. 4.6.

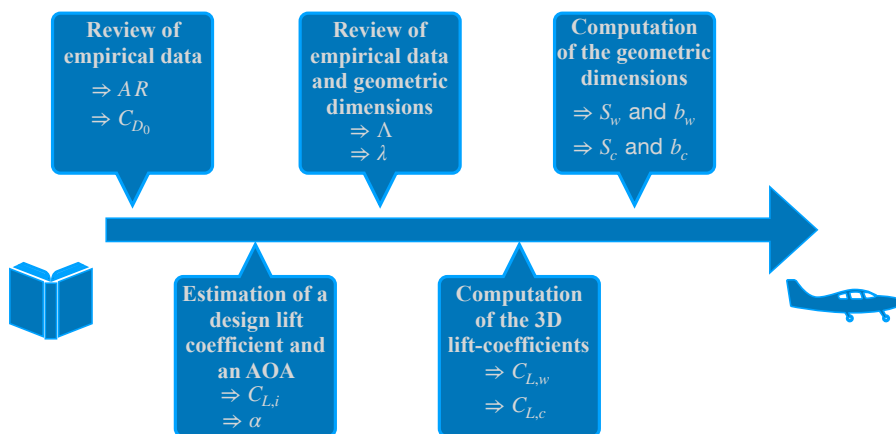


**Figure 4.6:** Flowchart of the geometric dimensions computation of the lifting surfaces.

According to empirical data [26], the **aspect ratio** is fixed to  $AR = 9$  according to a trade-off between performances and the structural properties of the airplane. In addition, the zero-lift drag coefficient can be considered equal to that of a small single engine aircraft with retractable landing gear such that  $C_{D_0} = 0.03$  :

$$e = 1.78 \cdot (1 - 0.45 \cdot AR^{0.68}) - 0.64 = 0.7831 \quad \text{and} \quad C_D = C_{D_0} + \frac{C_L^2}{\pi AR e} \quad (3)$$

From this quadratic drag model can be estimated the design-lift coefficient  $C_{L,i}$  and the angle of incidence of the wing and the canard. It can be seen in Fig. 4.7 that the lift-to-drag ratio of the airplane reaches maximum values in the range  $C_L \in [0.65 \ 1]$ . Hence, the design-lift coefficient of the Duckampus is fixed to  $C_{L,i} = 0.7$ . This value corresponds to a lift-drag ratio of 13.3 and an angle of attack of  $4^\circ$  (See Fig. 4.8).



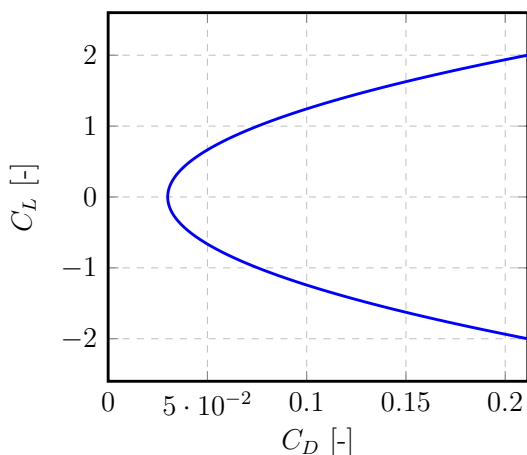


**Figure 4.7:** Polar of the conceptual design of the aircraft.

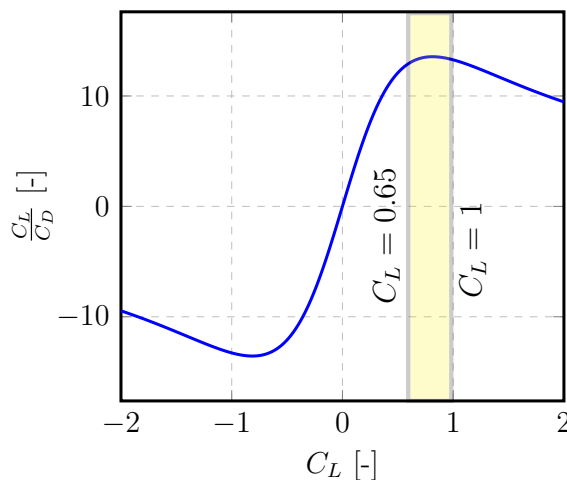


**Figure 4.8:** Decision graph of the optimal lift to drag ratio of the airplane.

The **angle of incidence** of the wing is selected in order to increase the lift coefficient during the cruise part of the flight. The angle of incidence of the wing is chosen equal to  $3^\circ$  i.e right before the optimum. For the stability of the aircraft, the canard needs to stall before the wing. To achieve this, the angle of incidence of the canard is higher than the angle of incidence of the wing. It is then chosen to  $5^\circ$ . As the limit of the drag bucket of the NACA 64<sub>3</sub> – 418 airfoil occurs approximately for an angle of attack of  $12^\circ$ , the stall would occur for the canard when the angle of attack reaches  $12 - 5 = 7^\circ$  and finally for the wing when the angle of attack is equal to  $12 - 3 = 9^\circ$ .

The **twist angle** ( $\Lambda$ ) is fixed to  $-2^\circ$ . For manufacturing ease, the same airfoil profile is chosen along the span. The twist is only geometric and the aerodynamic twist equals  $0^\circ$ . The goal of such a configuration is to ensure that the tip of the wing stalls after the root. The rotors being placed at the end of the wing stall must be prevented in this region.

The **taper ratio** ( $\lambda$ ) is chosen to reduce induced drag. For an aspect ratio of 9, it can be found in the literature [26] that  $\lambda = 0.35$  maximizes the Oswald efficiency.

Using the experimental data provided by the Abbott (Fig. 4.9), the two-dimensional lift curve slope  $c_{l_\alpha}$  can be computed. Consequently, the three-dimensional lift coefficient  $C_{L_\alpha}$  can be computed from Torenbeek [26] :

$$C_{L_\alpha} = 0.995 \frac{c_{l_\alpha}}{E + \frac{c_{l_\alpha}}{\pi AR}} \quad \text{where} \quad E = 1 + \frac{2\lambda}{AR(1 + \lambda)} \quad (4)$$



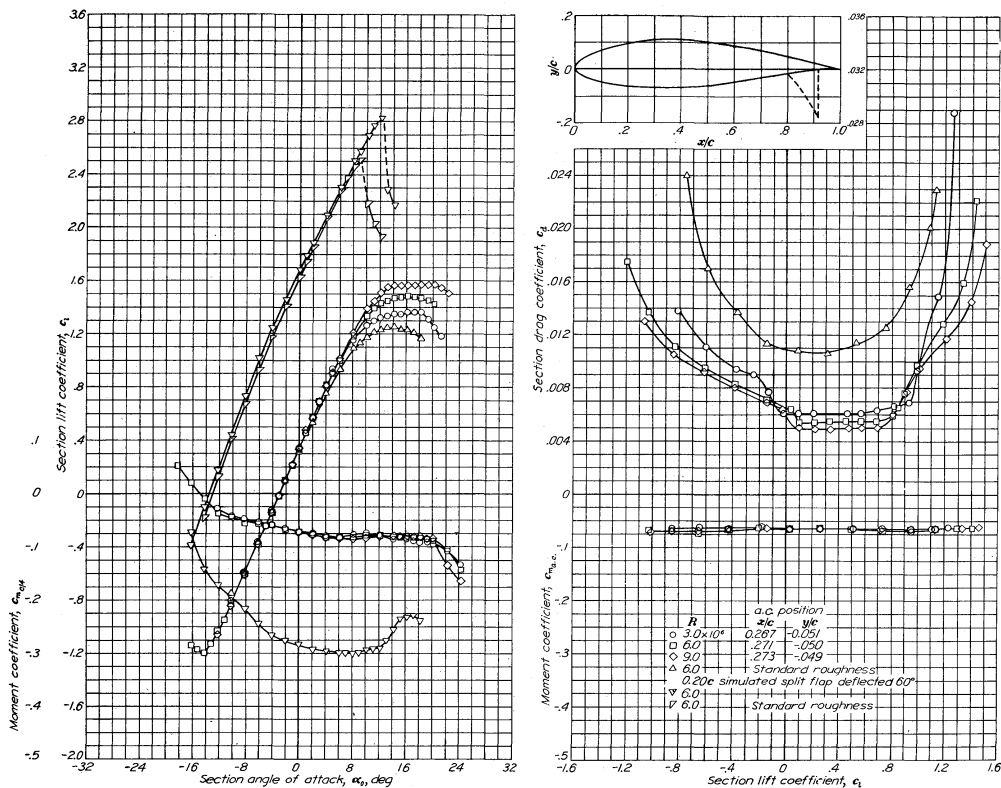


**Figure 4.9:** Variation of the lift coefficient  $c_l$  with respect to the angle of attack  $\alpha$  (left) and Polar diagram (right) for a NACA643 – 418 airfoil [27].

Finally, the lift coefficients of the lifting surfaces can be computed :

$$C_L^w = 0.529 \quad \text{and} \quad C_L^c = 0.5865 \quad (5)$$

By the definition of the lift coefficient and of the aspect ratio, the surfaces and the spans of the lifting surfaces are :

$$(b_w, S_w) = (9.87, 10.83) \quad \text{and} \quad (b_c, S_c) = (5.01, 4.19) \quad (6)$$

Consequently, the lift coefficient of the Duckampus is given by :

$$C_L^{\text{plane}} = C_L^w + C_L^c \frac{S_c}{S_w} = 0.74 \quad (7)$$

This value is then really near from the design lift coefficient  $C_{L,i}$ . The latter may seem high comparing to the lift coefficient needed to balance the weight and the lift :

$$C_L^{W=L} = \frac{W}{\frac{1}{2} \rho V_{cr}^2 S_w} = 0.65 \quad (8)$$





However, every previous computations have been made assuming no downwash due to the canard. The airplane lift coefficient is then selected considering a safety margin.

The results obtained after convergence are presented graphically in Fig. 4.10. The main parameters are also presented in Table 4.4.

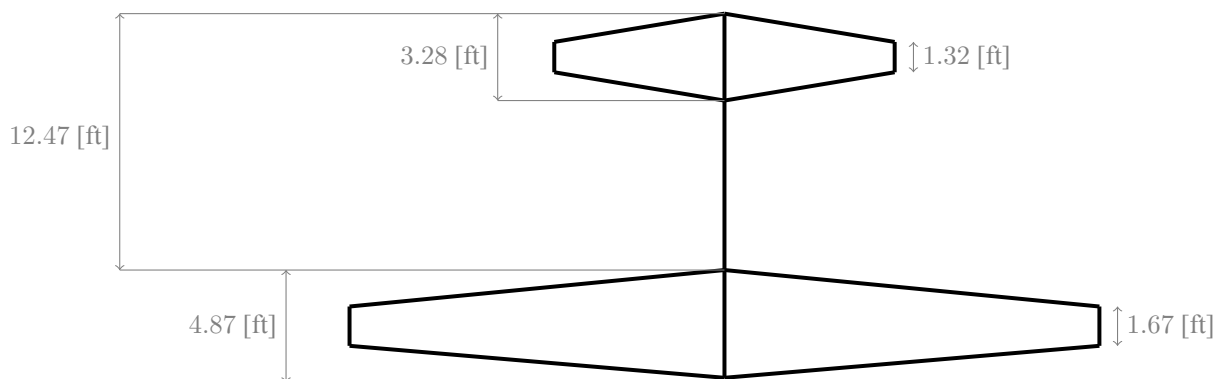


**Figure 4.10:** Schematic representation of the wing.

Name of the property	Dimension	
	Wing	Canard
Span	32.38 ft	16.44 ft
Surface	116.57 ft <sup>2</sup>	45.10 ft <sup>2</sup>
Mean chord	3.61 ft	2.76 ft
Aspect ratio	9	6
Taper	0.35	0.35
Chord at root	4.872 ft	3.77 ft
Chord at tip	1.706 ft	1.616 ft
Wetted surface	240.14 ft <sup>2</sup>	92.89 ft <sup>2</sup>
Twist	-2°	-2°
Angle of incidence	3°	5°
Sweep at quarter-chord	0°	0°
Mass	582.46 [lb]	220.7 [lb]

**Table 4.4:** Summary of the dimensions of the wing.







### 4.2.3 Battery storage - Battery integrated wing

The chosen airfoil has a thickness to chord ratio of 18 % which may seem quite large. However this thickness is very useful for battery storage. The half wing is composed of 13 ribs and 2 spars (see Fig. 4.11). The tilt mechanism being located at the half-span, only a certain volume of the wing can be used for battery storage. The remaining volume is approximately 10.24 ft<sup>3</sup> per wing.

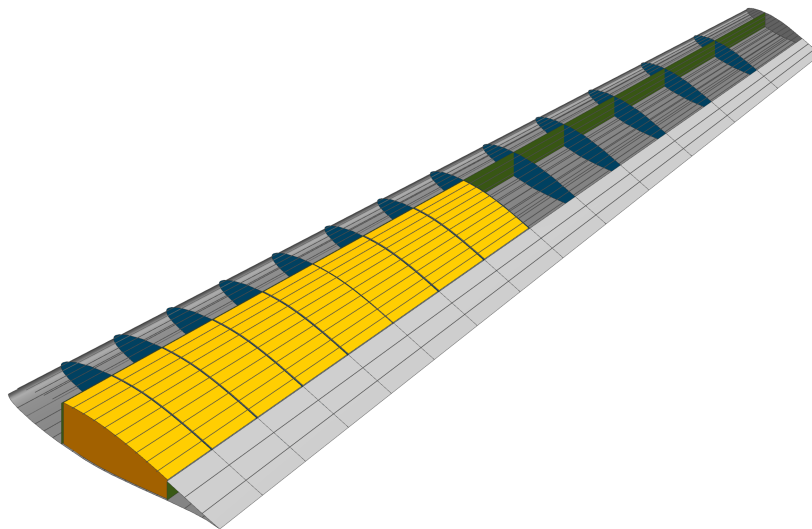


**Figure 4.11:** CAD of the wing structure.

The total battery volume is  $V_{\text{tot,batt}} = 7 \text{ ft}^3$  while the dimensions of each battery are  $5.7 \times 3 \times 0.4 \text{ [in]}$ , i.e.  $V_{\text{batt}} = 4 \times 10^{-3} \text{ ft}^3$ .

In addition, the batteries must be stored in cases. The latter have dimensions compatible with the geometry of the wing (see yellow boxes in Fig. 4.11). Given that the battery case is an integral part of the aircraft's wing structure, access panels for routine maintenance and inspection are required. Furthermore, the batteries are distributed equally between the two halves of the wing.

### 4.2.4 Fin

The final section of the aerodynamic design aims at ensuring the lateral stability of the aircraft and controlling side slip. To this end, a fin or vertical stabilizer is added to the aircraft. Note that no horizontal stabilizer is mounted on the aircraft given that a canard is already present. Finally, in order to control the yaw of the airplane, a rudder is designed.





The chosen airfoil for the fin must be symmetric and the thickness must be reduced as much as possible to decrease the drag produced by the fin. Consequently, the best suitable airfoil is a NACA 0012. In addition, the aspect ratio, the taper and the sweep angle of the fin are imposed to 1.2, 0.5 and  $35^\circ$  respectively using bibliographical reviews of similar aircraft.

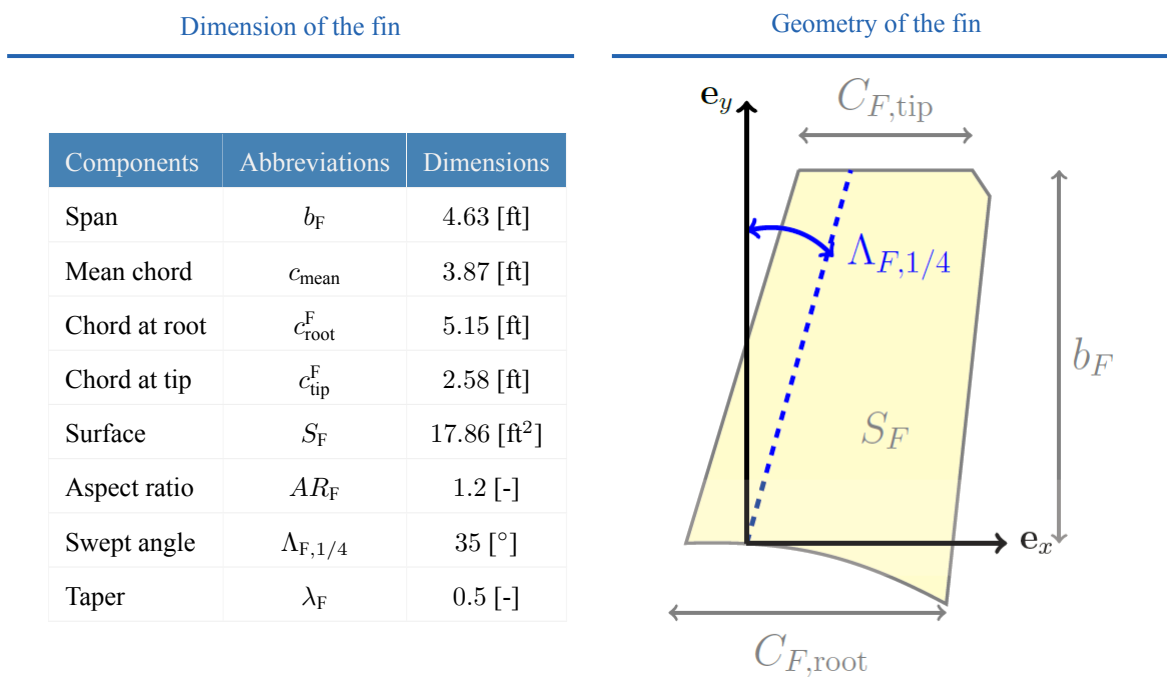


Figure 4.12: Summary of the geometry and the dimensions of the fin.

## 4.3 Fuselage

The fuselage is the main body section of an aircraft and provides a volume which holds the passengers and many components. It also contributes to the stability of the aircraft. The choice of the fuselage shape results from a trade-off between aerodynamics and price.

### 4.3.1 Choice of fuselage shape

The chosen fuselage configuration is a tube fuselage [28]. Indeed, this type of fuselage owns several advantages. The first one is the reduction of the drag compared to the frustrum fuselage [28]. The second advantage is that such fuselages are less expensive than the tadpole fuselage. Moreover, in the present case the flight altitude is low and thus the fuselage does not have to be pressurized. Hence, its cross-sectional shape does not have to be circular.





### 4.3.2 Internal layout

The internal layout of the aircraft is depicted in Fig. 4.13a. The Duckampus has a car-liker internal design i.e two front seats and two back seats. As it is designed to fly over short periods, it is assessed that there is no need for walking space or a toilet. Moreover, the Duckampus:

- ✓ offers comfort with high-quality leather seats and enough legroom (Fig. 4.13b);
- ✓ provides entertainment with four tablets connected to new-technology transparent screens;
- ✓ makes some interesting features available for its clients such as phone recharging devices, cup-holder, table to lay a newspaper, book or computer on it.

It can also be highlighted that the autonomous system allows to board one additional passenger and reduces the space dedicated to the cockpit. This does not only result in weight savings, but it also allows to sell the aircraft at a higher price as will be discussed in Section 8.

From a technical point of view, the Duckampus must ensure thermal and acoustic insulation of the cabin. In addition, the coating material must be durable and it must provide fire, static resistance and maximum cleanability. All these features should be satisfied without increasing too much the weight. The selected material for the interior components is then the composite shown in Table 4.5.

Facing	Core	Adhesive	Finishing
Phenolic resin	Honeycomb aramid fibre	Epoxy	Polyvinyl chloride

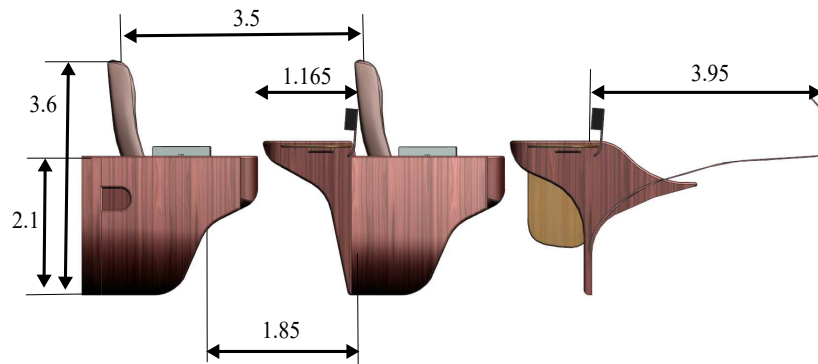
**Table 4.5:** Composite materials description for the interior components.

Finally, luggage is stored at the back of the cabin. The passengers can access this storage room using a door located at the back of the aircraft.

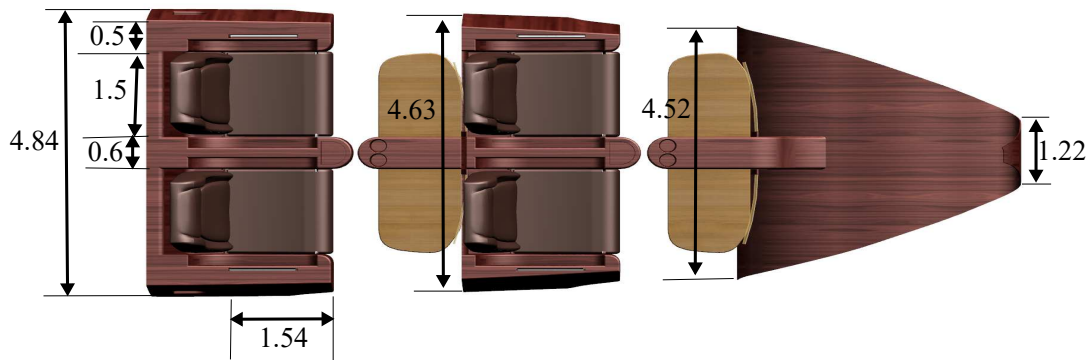




(a) Internal layout.



(b) Side view.



(c) Top view.

Figure 4.13: Design and dimensions [ft] of the internal layout of the fuselage.

### 4.3.3 Weight of the fuselage

Assuming a circular-like shape for the fuselage with a 0.039 in-thick skin, discussed in Section 5.3.4, made of Carbon fiber reinforced polymer (CFRP), the weight of the fuselage can be estimated to around 149 lbf. However, in this first approximation, only the coating part of the fuselage is considered. In that way, its total weight can be three times more, by taking into account stringers, thermal insulators, etc. All this leads to a final weight of about 450 lbf.





## 4.4 Landing gear

The aim of this section is to review all landing gear requirements in order to select the optimal configuration.

### 4.4.1 Main features

VTOL aircraft can be described as unconventional since they do not lift off in the same way as typical aircraft do. This may have a direct consequence on the choice of the landing gear as skids and rocket-like landing gear may be considered instead of classical wheels. Nevertheless, a wheeled landing gear is selected for the present aircraft. Indeed, even if they are a bit heavier, wheels enable to increase the stability of the whole aircraft. Indeed, the main advantage is that wheels enhance the grip on the ground that could turn out essential depending on the use of the aircraft. For instance, if the landing is occurring on an uneven ground, wheels are appropriated. Besides, only wheels allow to maneuver the aircraft because they are much more willing to taxi than other landing gear types. In the end, classical wheels with type III tires made up of maraging steel are selected. Their dimensions are shown in Fig. 4.14

In the aim of determining the most suitable landing gear configuration. The tricycle configuration is chosen. Indeed, the tricycle layout is preferred for the Duckampus as the wing, located behind the CG, is the main load and it requires heavy supports during landing. That is why there are two wheels at the back of the fuselage and one at the front. Another advantage of the tricycle is that it is stable on the ground and that enables to maneuver in an easy way. [28].

For the Duckampus design, the distribution of the load between the main and nose landing gear is as follows:

- Main landing gear:  $F_m = 3,943$  lbf
- Nose landing gear:  $F_n = 556$  lbf

The configuration is now determined but two options remain : either the landing gear is fixed or retractable. The former adds some drag since it remains exposed to the slipstream while the aircraft is flying. This results in a decrease in the velocity for a given power which decreases the performances of the aircraft. However, this drawback is not of great importance regarding the Duckampus since it flies at low speed and for short journeys. Moreover, the added drag can be reduced by adding streamlined fairings. On the other side, a fixed landing gear requires a less complex mechanical system than a retractable and thus saves some weight. A direct consequence is that fixed landing gears are less expensive. For all these reasons, a fixed landing gear is selected for the Duckampus. Thereby, since the weight of this technology is relatively small, it confirms that it would not be advantageous to use other type of landing gear such as skids.

To link the wheels to the airframe, oleo-pneumatic trailing-link shock absorbers are chosen for their high efficiency and energy dissipation. They are recovered by streamlined fairings with expanded fillet around the wheels (Fig. 4.14).





## 4.4.2 Geometric layout

The distance between the main and nose landing gear as well as the distance between the two main wheels, called wheelbase and wheel track respectively, are chosen so as to provide a stable (longitudinal and lateral) position for the aircraft when it lands on the ground. To compute them, the basic layout of the structure has to be considered. The wheel track is the maximum distance where the wheels can be placed while remaining on the fuselage, i.e. 3.36 ft. It is decided to dispose the nose landing gear below the canard to be close to the nose of the aircraft. This means it is located 3 ft away from the nose of the fuselage. The lower part of the aircraft is depicted in Fig. 4.14.

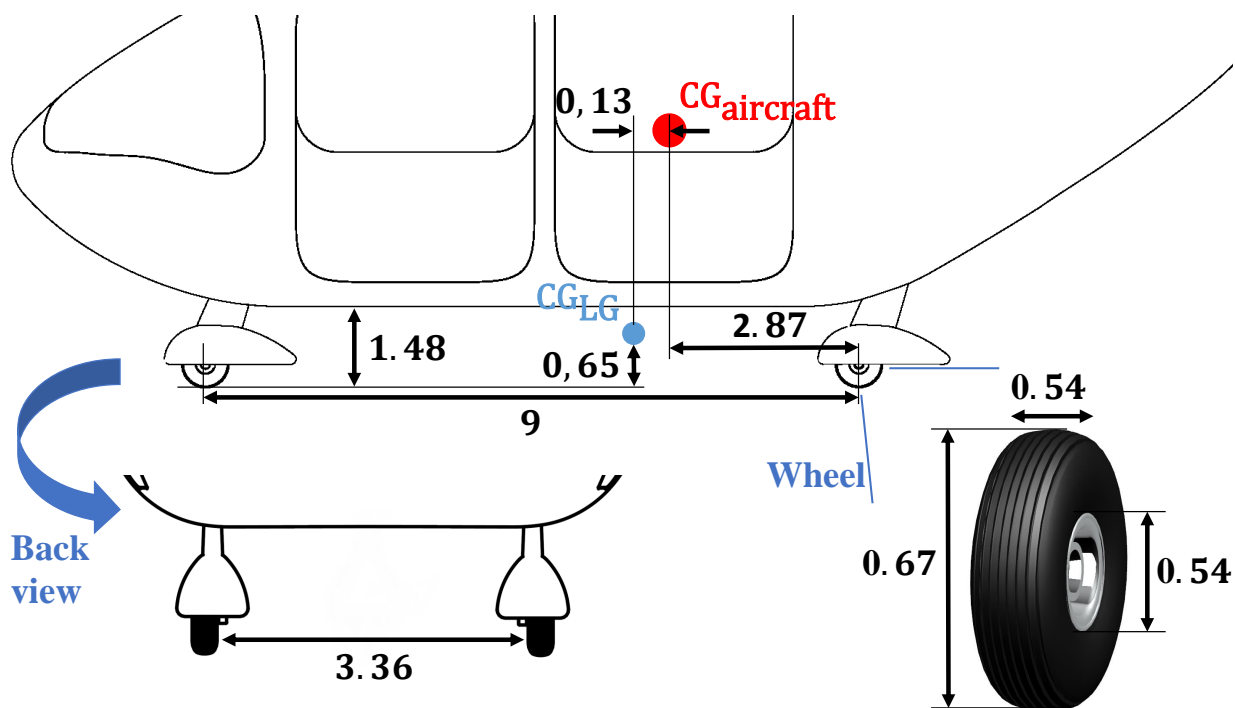


Figure 4.14: Landing gear layout [ft].

## 4.4.3 Weight

The mass of the landing gear is directly related to the total mass of the aircraft as it must support the latter during landing and takeoff. This weight depends on the diameter of the tires and the material used. In that way, it represents typically 5% of the total weight [29] of the first design iteration. As a pessimistic approach is considered, the actual weight of the landing gear is  $W_{LG} = 225$  lbf.





## 4.5 Material choice

Materials employed for the conception of the aircraft are described in this section. The selection of materials is crucial for the design and for the cost study since they influence widely the price of the entire structure.

### 4.5.1 Skins

The first part of the aircraft that is analyzed is the skin of the fuselage, the wing the canard and the rudder. And the choice of the material is driven by:

- **Low weight:** engineers are more and more preoccupied to reduce the weight of the aircraft to be able to achieve battery savings.
- **High static strength:** some parts of the aircraft and particularly the wing skin have to withstand high forces such as wind shear or other external loading.
- **Good fatigue performance:** the lifetime of the aircraft components largely depends on the fatigue performance. Thereby, if the fatigue properties are good, it increases the lifespan of the plane and thus, needs in maintenance and costs can be reduced.
- **Good fracture toughness:** the fracture toughness or the resistance of a material to the propagation crack must be high. In fact, a small crack in the structure can not grow too quickly that would lead to a sudden failure. [30]

By performing a study that meets all the requirements with the *CES* software [31], the selected material for the skin of the wings, the canard, the fuselage and the rudder is the CFRP (epoxy matrix) or Carbon Fiber Reinforced Polymer. This is a light and strong composite based on carbon. The use of composite for the skin is useful since joints and rivets are not needed anymore because a skin made of composite is directly built in one piece. That leads to better performance in terms of fatigue resistance [30].

### 4.5.2 Frames of the aircraft

The frame of the aircraft is typically composed of spars, ribs and stringers. For all these, the choice of the material is driven by:

- **Weight:** for energy saving purposes, the aircraft must be as light as possible.
- **Fracture toughness:** it is still important that a small crack does not propagate too quickly in the stringers, spars and ribs in order to avoid plastic deformations or even worse, a break.





- **Stiffness:** the stiffness must be high to resist deformation in response to an applied force.

By performing a *CES* study [31], CFRP is chosen.

### 4.5.3 Other components

For the landing gear, it is important that the tensile strength and the fracture toughness are high. And a material that performs well for the two criteria is the maraging steel. It is well suited for this application and especially for safety-critical aircraft structures that need damage tolerance that is high [32]. Moreover, it is easier to machine and to weld whereas its corrosion resistance is really good. However, maraging steel can not be exploited for too many components of the aircraft since it is generally three times more expensive than the typical carbon-alloy materials.

Moreover, concerning the blades of the engines, there are made of Carbon fiber reinforced epoxy that allows them to become stronger and more durable. Thereby, this material enables to reduce the inertia of the blade that permits to rotate easier. To end up with, the windshield is made of acrylic.

### 4.6 Center of gravity

At this point of the design, all components of the aircraft are chosen. The different component weights and their locations on the aircraft are summarized in Fig. 4.15. All these values and all the locations are very important when dealing with stability.

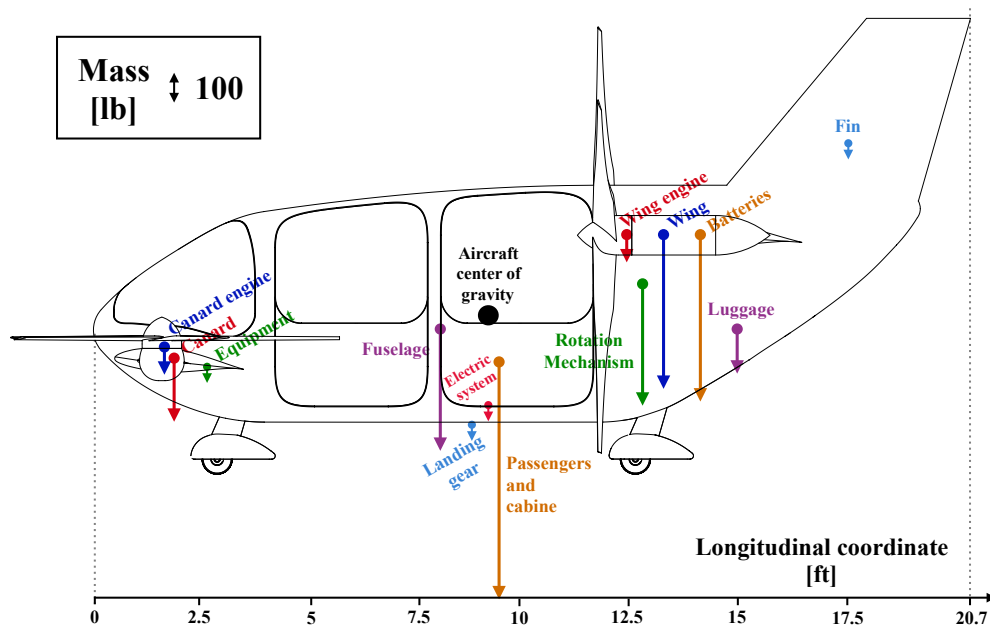


Figure 4.15: Representation of all component weights/masses and their locations on the aircraft. Full payload case.







# 5 Aircraft analysis

## 5.1 Aerodynamics

This section details the aerodynamic analysis of the Duckampus. In particular, the polar graph of the aircraft, linking lift and drag, will be computed. The total drag can be subdivided into different components (Fig. 5.1). At the stage where the layout and main geometric dimensions of the aircraft have been defined, a deeper aerodynamic analysis can be performed with more accurate tools. Two approaches have been considered :

- ① A study based on statistical and experimental data. The complete discussion is based on Appendix F of Torenbeek (1988) [26] and allows the estimation of the airplane drag at subsonic speed in the en-route configuration.
- ② A numerical study using Tranair, which is a commercial software used to model wings and aircraft, solving the Full Potential Equation with viscous-inviscid interaction corrections. This software is implemented as an iterative process with a coupling between a solution for a potential equation and boundary layer equations. The solution of the boundary layer equations is derived from pressure and velocity distribution of the inviscid case and the solution of the former equations provides a set of boundary conditions for the inviscid computation, with the addition of a blowing velocity. The solution of the boundary layer equations is driven by the pressure field (or velocity distribution) on the configuration surfaces. The boundary layer solution provides a set of actualized boundary conditions for the inviscid solver.

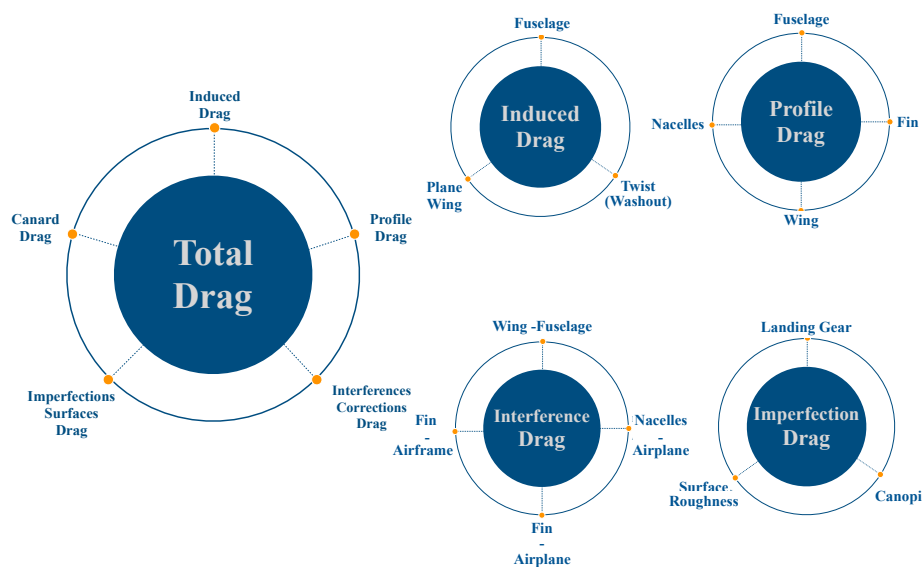


Figure 5.1: Total drag breakdown and subdivision of the different drag components.





## 5.1.1 Statistical and Empirical drag study

Each of the drag components can also be subdivided into several components (Fig 5.1). The polar graph of the airplane can then be plotted by computation and summation of all these drag subdivisions :

$$C_D = \sum_j A_j + \sum_j B_j C_L + \sum_j D_j C_L^2 \quad (9)$$

where  $A_j$ ,  $B_j$  and  $D_j$  are coefficients representing the contribution of drag subdivision  $j$  to the total drag  $C_D$ . Finally, the drag components are expressed as "counts"; 1 count is  $\Delta C_D = .0001$  and the reference area is the gross wing area  $S_w$ .

### A. Induced Drag

The induced drag corresponds to the lift-dependent drag associated to the trailing vortices generated by the loss of kinetic energy in the system behind the aircraft. Two main parts of the aircraft generate induced-drag i.e the wing, the canard and the fuselage.

As far as the wing and the canard are concerned, provided that they are assumed to be isolated bodies, the drag can be estimated using potential flow theory, particularly lifting line theory. However, due to limitation of this theory the drag induced by the wing has been divided in two different contribution. First, the drag coefficient is computed assuming an untwisted plane wing/canard ( $C_{D,i}^{\text{plane}}$ ) and then a correction term is added to take into account the wing washout due to the twist angle ( $C_{D,i}^{\text{twist}}$ ).

Regarding the fuselage, the latter can be considered as an isolated body of revolution. Due to its shape, the drag generated by the fuselage is far more due to viscous effect and then boundary layer than by induced-drag. Hence, the induced drag of the fuselage ( $C_{D,i}^{\text{fus}}$ ) is expected to not be very high.

Detailed computations result in the numerical values of the coefficients  $A_i$ ,  $B_i$  and  $D_i$  (see Eq. (9)). Furthermore, the proportions to the induced-drag for each component

$$C_{D,i} = C_{D,i}^{\text{plane,w}} + C_{D,i}^{\text{plane,c}} + C_{D,i}^{\text{twist,w}} + C_{D,i}^{\text{twist,c}} + C_{D,i}^{\text{fus}} \quad (10)$$

are computed using the cruise lift coefficient ( $C_{L_{cr}} = 0.75$ ).





$$C_{D,i} = \sum_i A_i + \sum_i B_i C_L + \sum_i D_i C_L^2$$

$$C_{D,i}^{cruise} = C_{D,i}(C_L = 0.75) = 0.02866$$

	$A_i$	$B_i$	$D_i$
$C_{D,i}^{plane,w}$	0	0	357
$C_{D,i}^{plane,c}$	0	0	137
$C_{D,i}^{twist,w}$	0.75	1.02	0
$C_{D,i}^{twist,c}$	0.29	0.39	0
$C_{D,i}^{fus}$	1.47	-12.28	25.58
$\sum$	2.51	-10.87	519.58

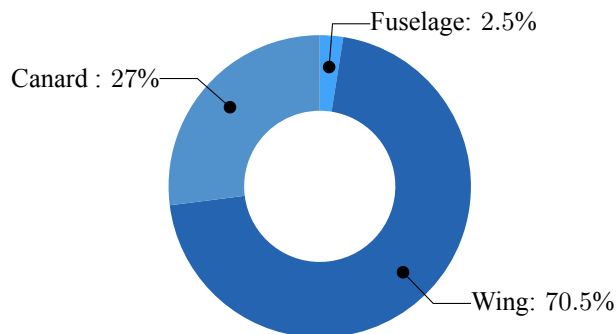


**Figure 5.2:** Breakdown of the induced drag, numerical values for each coefficient and proportion of each component for the cruise phase  $C_L^{cr} = 0.75$ . The coefficients A,B and D are expressed in count drag (.0001).

### B. Profile Drag

The profile drag is composed of the skin friction and the pressure drag due to the viscous effects. The main parts of the airplane leading to drag are wing ( $C_{D,p}^{wing}$ ), canard ( $C_{D,p}^{can}$ ), fuselage ( $C_{D,p}^{fus}$ ), nacelles ( $C_{D,p}^{nac}$ ) and fin ( $C_{D,p}^{fin}$ ) are assumed to be smooth isolated streamline bodies. Furthermore, corrections are made to take into account the interaction with the flow field, the protuberances or the surface roughness.

Under the assumption of a well streamlined component, an analogy can be made between the profile drag of the component and an equivalent flat plate. The skin friction coefficient of a flat plate can be derived analytically :

$$C_f^{lam} = \frac{1.628}{\sqrt{Re}} \quad \text{and} \quad C_f^{turb} = \frac{0.455}{(\log_{10} Re)^{2.56} [1 + 0.144 M^2]^{0.65}} \quad (11)$$

where the characteristic length used for the Reynolds number depends on the component studied. The skin friction coefficient is then computed as a weighted sum of the laminar and the turbulent coefficients.

As far as the wing, the canard and the fin are concerned, the characteristic length is the mean aerodynamic chord while the transition points  $x_{tr}^{wing}$ ,  $x_{tr}^{can}$  and  $x_{tr}^{fin}$  can be estimated as the points of minimum pressure. After computation on XFoil version 1.1, it can be found that  $x_{tr}^{wing} = 0.26$ ,  $x_{tr}^{can} = 0.1$  and  $x_{tr}^{fin} = 0.42$ . All transition points have been normalized by the chord.

Regarding the fuselage and the nacelles, the characteristic length is the total length of the fuselage i.e the sum of the nose, cabin and after-body lengths and the effective length of the nacelle while the transition point for the fuselage





is  $x_{tr}^{fus} = 0$  and flow is assumed to be fully laminar for the nacelles  $x_{tr}^{nac} = 1$ .

The computations lead to the numerical values of the coefficients  $A_p, B_p$  and  $D_p$  (see Eq. (9)). Furthermore, the proportion of the profile drag for each component

$$C_{D,p} = C_{D,p}^{wing} + C_{D,p}^{can} + C_{D,p}^{fus} + C_{D,p}^{fin} + C_{D,p}^{nac} \quad (12)$$

is computed using the cruise lift coefficient ( $C_{L_{cr}} = 0.75$ ).

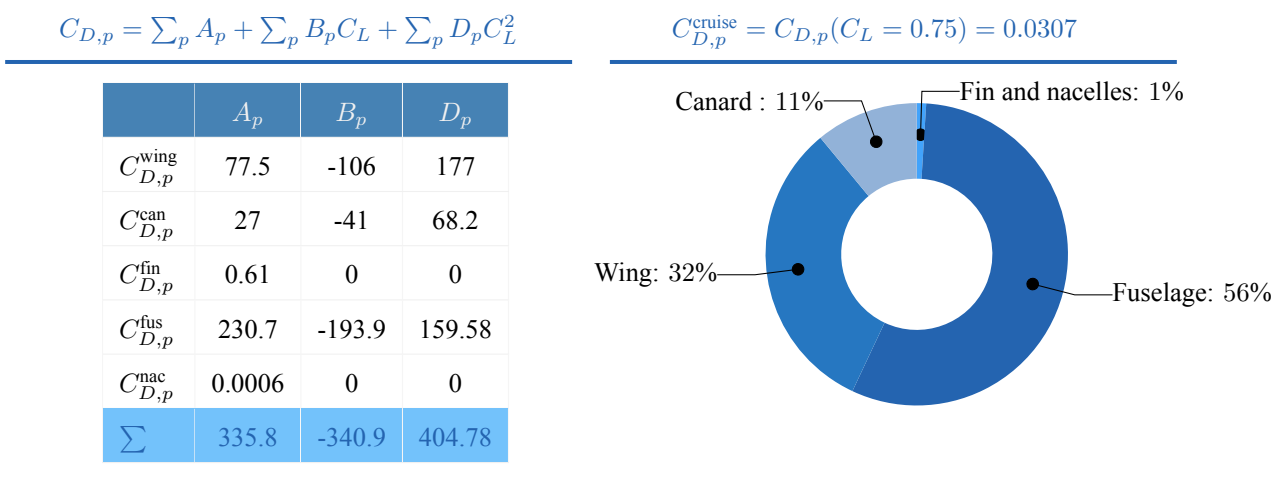


**Figure 5.3:** Breakdown of the profile drag, numerical values for each coefficient and proportion of each component for the cruise phase  $C_L^{cr} = 0.75$ . The coefficients A,B and D are expressed in count drag (.0001).

### C. Interference Drag

This component of drag allows to take into account the interactions of the flow fields around the main parts of the airplane. Two main subdivisions are studied, the interference between lifting surfaces and fuselage and the interference between the nacelle and the wing. These corrections can be either due to the modification in the lift distribution or due to the viscous effects at the junctions.

At the lifting surfaces-fuselage junction, the lifting surfaces generate a disturbance in the lift distribution. The body nose will be subject to a lift increment while the after-body will be subject to a reduction in lift. Furthermore, the thickness of the boundary layer at the junction increases as well as the local flow velocity. Both phenomena lead to a drag correction ( $\Delta C_D^{w/f}$ ) and ( $\Delta C_D^{c/f}$ ).

The same corrections can be made for the nacelles. Indeed, the installation of the propellers leads to a local change in lift and interferences between the boundary layers of the nacelles and the wing occurs. These phenomena lead in





correction for the drag coefficient ( $\Delta C_D^{w/n}$ ).

The calculations lead to the numerical values for coefficients  $A_\Delta, B_\Delta$  and  $D_\Delta$  (see Eq. (9)). Furthermore, the proportion to the interference drag for each component

$$C_{D,\Delta} = \Delta C_D^{w/f} + \Delta C_D^{c/f} + \Delta C_D^{w/n} \quad (13)$$

is computed using the cruise lift coefficient ( $C_{L_{cr}} = 0.75$ ).

$$C_{D,\Delta} = \sum_{\Delta} A_{\Delta} + \sum_{\Delta} B_{\Delta} C_L + \sum_{\Delta} D_{\Delta} C_L^2$$

$$C_{D,\Delta}^{cruise} = C_{D,\Delta} (C_L = 0.75) = 0.0066$$

	$A_{\Delta}$	$B_{\Delta}$	$D_{\Delta}$
$\Delta C_D^{w/f}$	10	28.6	0
$\Delta C_D^{c/f}$	4.75	28.64	0
$\Delta C_D^{w/n}$	2.65	7.95	0
$\Sigma$	17.4	65.15	0

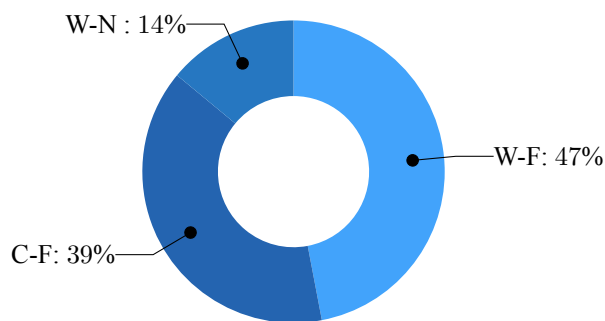


**Figure 5.4:** Breakdown of the interference drag, numerical values for each coefficient and proportion of each component for the cruise phase  $C_L^{cr} = 0.75$ . The coefficients A,B and D are expressed in count drag (.0001).

### D. Imperfection Drag

Imperfection drag involves additional contributions to the drag due to protuberances such as the windows of the canopy ( $C_{D,im}^{can}$ ) or the landing gear ( $C_{D,im}^{gear}$ ).

These computations lead to numerical values for coefficients  $A_{im}, B_{im}$  and  $D_{im}$  (see Eq.(9)). Furthermore, the proportion to the imperfection drag for each component

$$C_{D,im} = \Delta C_{D,im}^{can} + \Delta C_{D,im}^{gear} \quad (14)$$

is computed using the cruise lift coefficient ( $C_{L_{cr}} = 0.75$ ).





$$C_{D,im} = \sum_{im} A_{im} + \sum_{im} B_{im} C_L + \sum_{im} D_{im} C_L^2$$

$$C_{D,im}^{cruise} = C_{D,im}(C_L = 0.75) = 0.0015$$

	$A_{im}$	$B_{im}$	$D_{im}$
$\Delta C_{D,im}^{can}$	10.96	0	0
$\Delta C_{D,im}^{gear}$	4.15	0	0
$\Sigma$	15.11	0	0

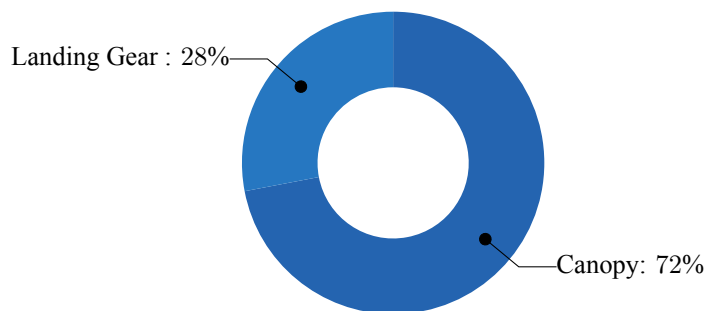


**Figure 5.5:** Breakdown of the imperfection drag, numerical values for each coefficient and proportion of each component for the cruise phase  $C_L^{cr} = 0.75$ . The coefficients A,B and D are expressed in count drag (.0001).

### E. Summary and numerical values of the quadratic model

After the computation of the drag coefficient associated to each component of the aircraft it yields the quadratic equation :

$$C_D = \sum_j A_j + \sum_j B_j C_L + \sum_j D_j C_L^2$$

$$= 0.0426 - 0.0364 C_L + 0.1257 C_L^2 \quad (15)$$

From this equation can be deduced the zero-lift drag coefficient ( $C_{D_0}$ ), the minimum drag coefficient ( $C_{D_{min}}$ ) and the associated lift coefficient ( $C_{L_{min,D}}$ ) as well as the maximum lift-to-drag ratio  $(C_L/C_D)_{max}$  and the associated lift coefficient ( $C_{L_{(C_L/C_D)_{max}}}$ ). The numerical results are available in Tab.5.1.

$C_{D_0}$	$C_{D_{min}}$	$C_{L_{min,D}}$	$(C_L/C_D)_{max}$	$C_{L_{(C_L/C_D)_{max}}}$
0.0376	0.0352	0.2	11.4	0.66

**Table 5.1:** Main aerodynamic parameters deduced from the polar graph using the quadratic model.

The total drag coefficient of the whole airplane during the cruise phase is  $C_D^{cr} = 0.0673$ . The proportions of the different sources of drag can be investigated (Fig. 5.6). First, the drag is broken down in the different parts of the airplane i.e the wing, the fuselage, the nacelle, the canard and the other parts such as the canopy or the landing gear. Then, the drag is broken down in the different physical phenomenons that lead to drag i.e the induced drag, the profile drag and finally the interference and imperfection corrections.



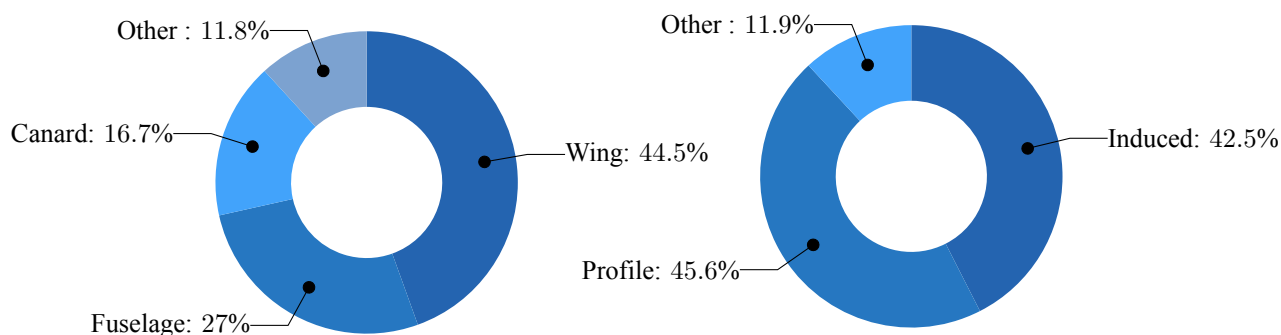


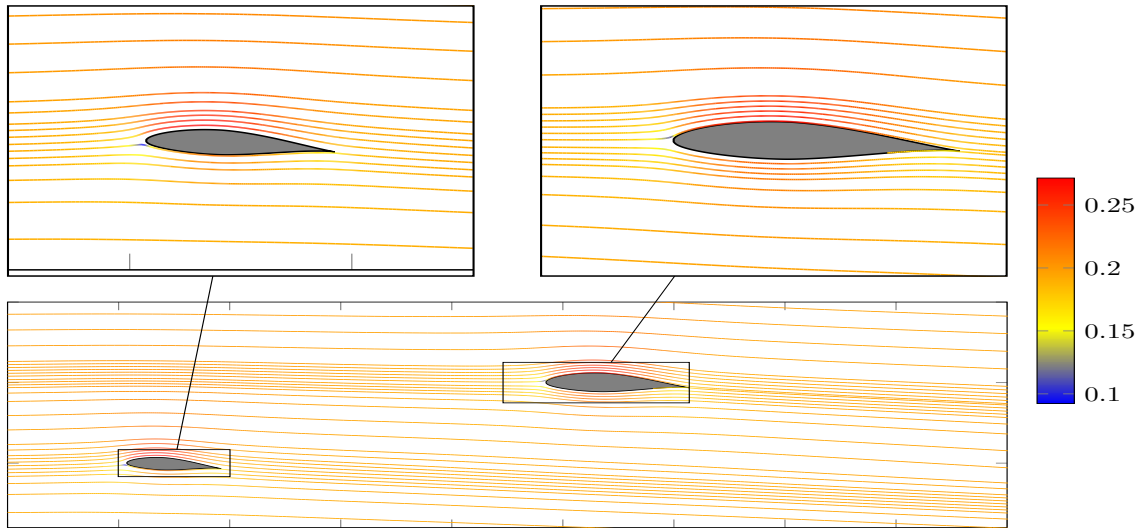
Figure 5.6: Proportions of the different sources of drag and drag quadratic model graph.

## 5.1.2 Computational fluid dynamics

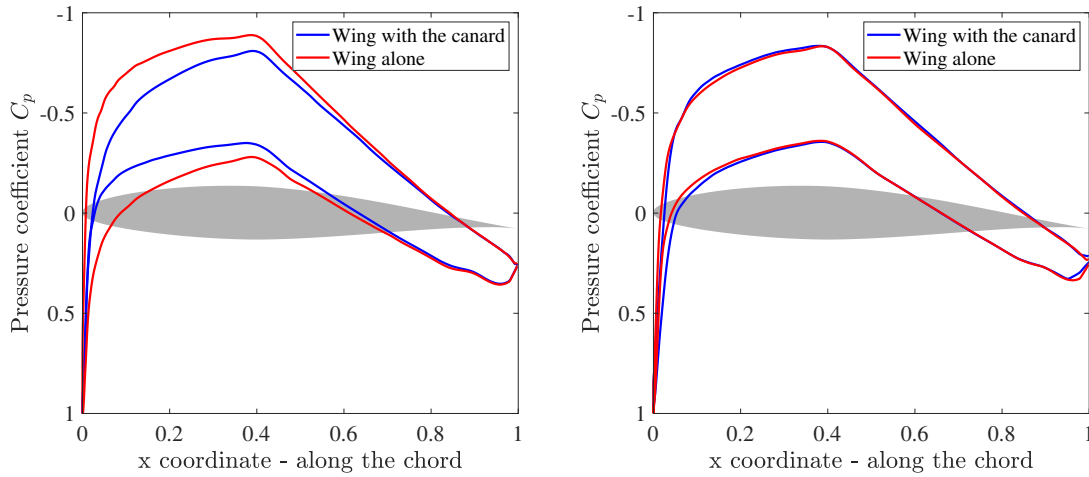
The computational fluid dynamics is performed using *Tranair* software. For sake of simplicity, only the canard and the wing are modelled in the computational domain. Full potentials equations are solved with viscous-inviscid interaction corrections at different angles of attack in the range  $[-20^\circ; 20^\circ]$ . The numerical simulations allow to analyze the flow behavior and the variation of different aerodynamic parameters around the lifting surfaces. In particular, the effect of the canard on the aft wing is studied. Finally, a comparison between the polar graph obtained by the empirical analysis and the numerical one is performed (Fig. 5.11).

First of all, the canard disturbs the flow seen by the wing, such that the effective angle of attack of the wing is decreased. The downwash is depicted using the streamlines in Figure 5.7a. The variation in the effective angle of attack is  $-2$  degrees at the root. As a direct consequence of this angle of attack reduction, the pressure coefficient ( $C_p$ ) is increased on the upper surface and decreased on the lower surface of the wing (Fig. 5.7b and c), leading to a decrease in lift. Further investigations of the streamlines distribution over the wingspan show that downwash effects start at the root of the wing up to a distance equal to the half-span of the canard and a light upwash can be seen at the tip of the wing.





(a) Streamlines of the flow field on a plane located for  $y = 1m$  and colormap of the Mach number along the streamlines.



(b) Variation of the pressure coefficient along the chord of the wing with and without a canard at the root. (c) Variation of the pressure coefficient along the chord of the wing with and without a canard at the tip.

**Figure 5.7:** Analysis of the effect of the canard on the aft wing. Numerical simulations performed at 150 mph at ground level at  $\alpha = 0^\circ$  using the software *Tranair*.

This phenomenon can be described by looking at the pressure distribution on the wing. Excluding effects due to recirculation at the tip, the pressure distribution is similar on each section. On the opposite side, some effects can be observed near the root of the wing. The pressure is decreased in this point caused by a decrease in the angle of attack linked to the downwash created by the canard.

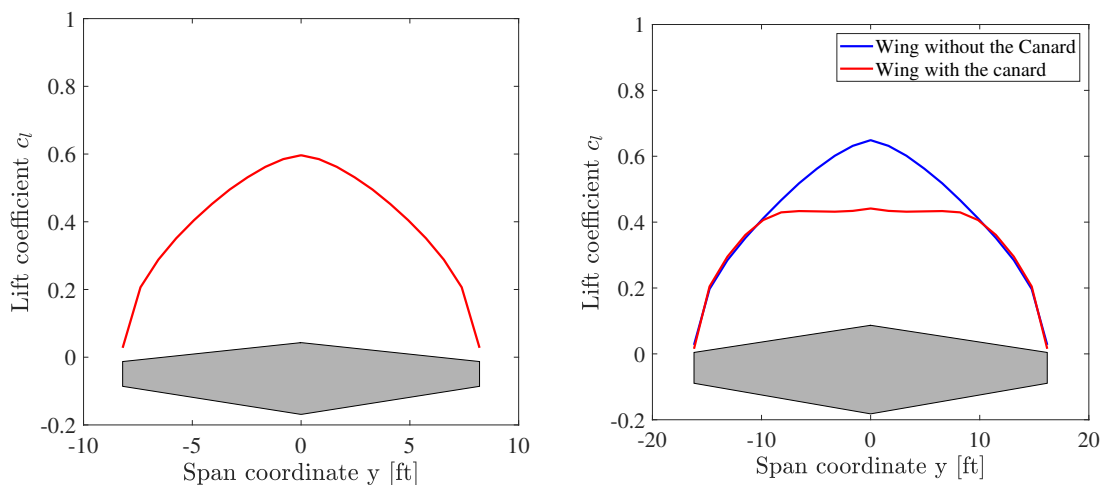
The variation of the sectional lift coefficient  $c_L^c$  of the canard is depicted in Figure 5.8a. The lift and drag are normalized with respect to the surface of the canard. This curve has a traditional shape, with a lift coefficient of about 0.6 at the root. The variation of the sectional lift coefficient of the wing with and without the effect of the canard is depicted in Figure 5.8b. The downwash effect is clearly visible, with a decrease of the lift coefficient at the root of about







50 % due to the reduction in effective angle of attack. At spanwise distances greater than 2.5 meters, the sectional lift coefficient becomes identical with or without the canard, as the flow is not disturbed anymore due to the fact that the span of the canard is smaller than the one of the wing. Note that the 3D lift coefficient of the wing is decrease by almost 18 % due to the influence of the canard.



(a) Spanwise distribution of the sectional lift coefficient of the canard. (b) Spanwise distribution of the sectional lift coefficient of the wing, with and without the influence of a canard.

**Figure 5.8:** Analysis of the spanwise sectional lift coefficient distribution and analysis of the influence of the canard at  $\alpha = 0^\circ$ .

### 5.1.3 Comparison between analytical and CFD analysis

Figure 5.9 shows the comparison between the 3D lift coefficient computed analytically during the conceptual design stage (Section 4.2) and the `Tranair` results. First of all, it is important to note that `Tranair` solve the Full Potential Equations and therefore is not able to describe the stall. The zone of confidence of the software results is between  $-10^\circ$  and  $10^\circ$  as simulations converge far from stall. The conceptual design lift estimates are higher than the `Tranair` results by approximately 10 % at cruise conditions ( $0^\circ$  angle of attack). This is due to the fact that the conceptual design method does not take into account the lift decrease in the wing due to the downwash created by the canard.



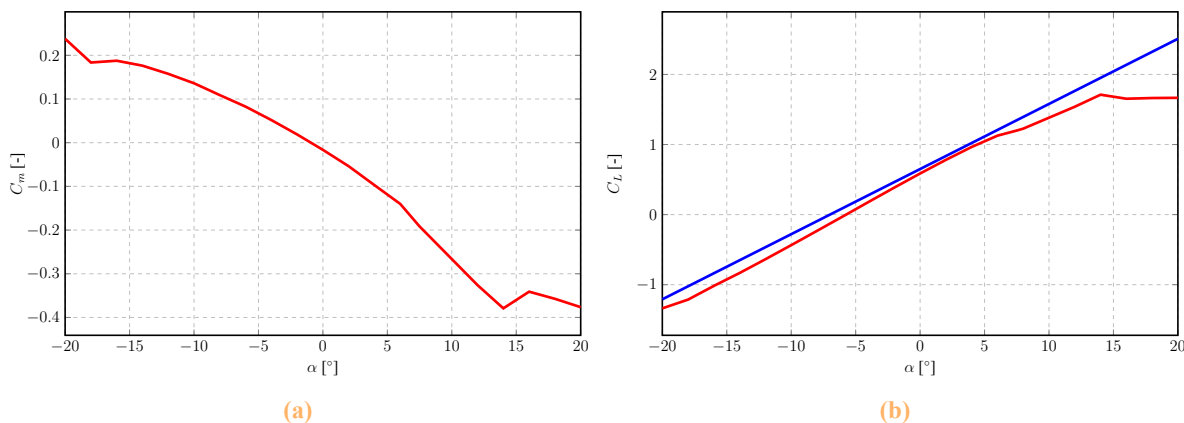


**Figure 5.9:** Comparison of the variation of Lift coefficient  $C_L$  and the pitching moment coefficient  $C_m$  with respect to the angle of attack using Tranair software (red) and analytical results (blue).

The  $C_m$  coefficient is computed around the center of gravity of the airplane and normalized by the product of the mean aerodynamic chord of the wing and the surface of the wing. It can be seen that the optimal lift-to-drag ratio is obtained when the angle of attack  $\alpha$  is equal to zero, corresponding to cruise conditions. For this value, we have a lift-to-drag ratio of 19.

It can be seen in Figure 5.10 and 5.11 that the preliminary design fit quite well the preliminary one. Indeed, both design methods provide more or less the same lift-to-drag ratio and polar curves. The difference with Tranair is a direct consequence of the lower drag predicted by the software.

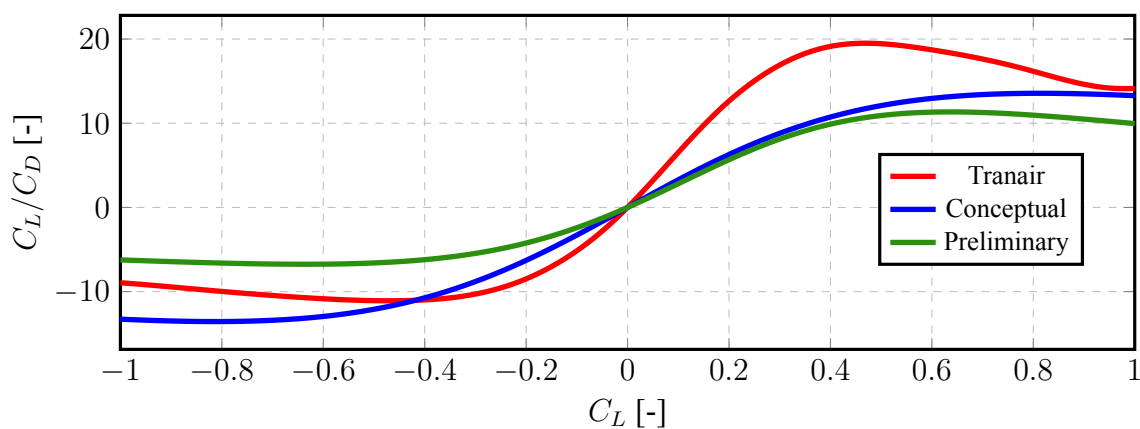


**Figure 5.10:** Comparison of the lift-to-drag ratio for the conceptual design, Tranair software and the preliminary design.

As far as the polar graph is concerned, obviously the same remarks can be made. Tranair under-estimates the drag because the analysis only considers the lifting surfaces. Finally, the preliminary design analyses yields to a symmetrical parabolic graph which emphasised the limitation of the model.



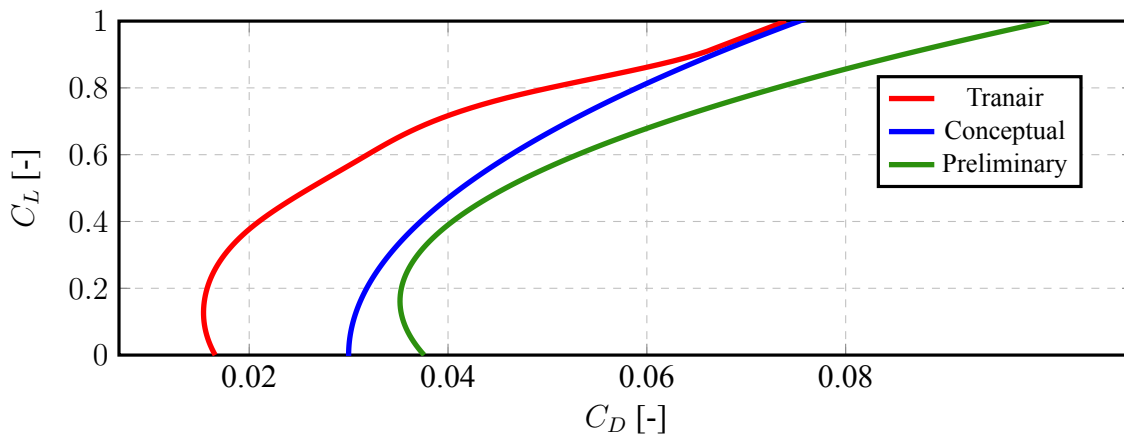


Figure 5.11: Comparison of the polar graph for the conceptual design, Tranair software and the preliminary design.

## 5.2 Performance

### 5.2.1 Payload-Range Diagram

After the computation of the total energy available (326.7 MJ), considering the fully loaded aircraft with four passengers and luggage, the total required battery mass is computed. In Figure 5.12, the Payload-Range Diagram shows how the maximum range evolves when the number of passengers varies. It is computed subtracting each time the weight of one passenger and its luggage from the total weight. Additionally to the diminishing of the energy consumed during takeoff and landing due to the reduced weight, there is also a reduction in the needed lift. This allows to mitigate the  $C_L$  and  $C_D$ . All this goes in the favor of the range which will be increased.

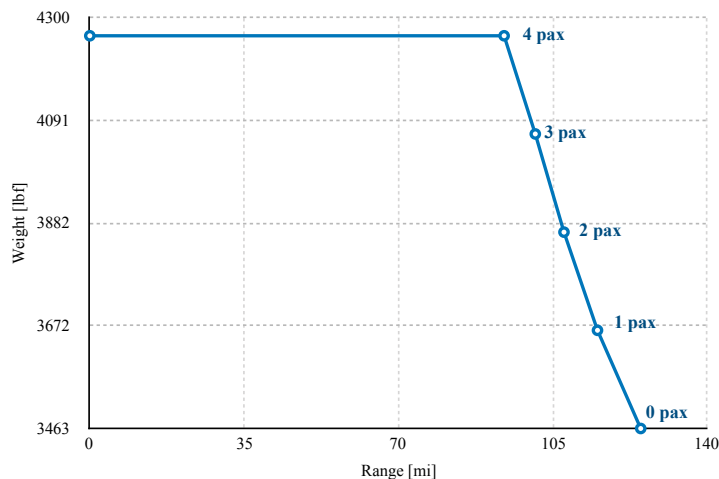


Figure 5.12: Payload-Range Diagram.





The diagram in Figure 5.12 takes into account only the distance covered during a standard mission. In addition to this range, energy is still available for emergency situations. In particular under the assumptions of the proposal for the reserve mission the energy allows to fly for 5 other minutes. Note that the high difference between the maximum range in the diagram and the sizing range in the proposal is due to the fact that the here also the distance traveled during climb and the transition phase while this is not considered during the sizing.

## 5.2.2 Placard Diagram

The variation of the design cruise Mach number  $M_c$  with altitude is depicted in the Placard diagram (see Fig. 5.13). This Mach number is based on the maximum cruise velocity reachable by the aircraft  $V_c = 208$  mph. This velocity is computed considering the maximum thrust reachable without altering the efficiency of the blade tips.

The diagram is divided in three regions :

- **First Region : 0 to 50 ft**

In this altitude range, the aircraft carries out its vertical takeoff during the hovering phase. The design Mach number related is equal to zero. While the aircraft does not have horizontal velocity, the thrust produced by the four engines is oriented in the vertical direction and has no other goal than elevating the aircraft.

- **Second Region : 50 to 1,500 ft**

Between 50 and 1,500 ft, the transition of the wing engines from the takeoff configuration to the cruise configuration limits the design cruise velocity. Moreover, the variation of the density and the temperature with the altitude influence also the design cruise Mach.

- **Third Region : 1,500 to 14,000 ft**

The design altitude is set to 1,500 ft. At this altitude, the design cruise Mach number is  $M_c = 0.27$ . Beyond this altitude, the Mach number slowly increases until reaching 0.28 at the ceiling (i.e. 14,000 ft).

Notice that the ceiling can be reached only if the aircraft carries no passengers. Indeed, according to the regulation 14 CFR at paragraph 25.841(a) : *”pressurized cabins and compartments to be occupied must be equipped to provide a cabin pressure altitude of not more than 8,000 ft at the maximum operating altitude of the airplane under normal operating conditions”*, the aircraft cannot exceed the maximum altitude of 8,000 feet for non pressurized cabin while clients are on board.



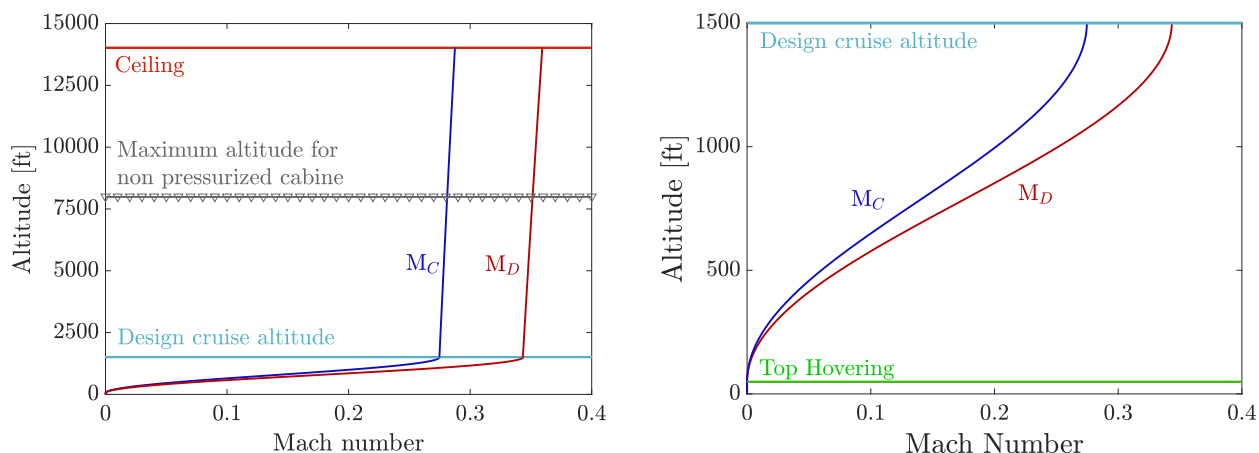


Figure 5.13: Placard diagram.

## 5.2.3 Flight envelope

The performance of the aircraft is demonstrated through the flight envelope. Characteristic velocities at cruise as well as characteristic load factors are given. The diagram is based on the design cruise velocity  $V_{c,max} = 208$  mph obtained when the engines produce the maximum thrust. The following characteristics can be read from the diagram :

- Stall velocity at cruise altitude for normal operating condition ( $n = 1$ ):

The stall velocity at cruise altitude is  $V_{s,+} = 91.7$  mph

- Maneuvering velocity :

Under the maneuvering speed, the aircraft must withstand the full deflection of control surfaces. The diagram shows that  $V_A = 158.9$  mph.

- Maximum stall velocity :

The maximum stall velocity is  $V_B = 163.4$  mph.

- Design diving velocity :

The design diving velocity is  $V_D = 260$  mph.

- Maximum and minimum load factors :

$n_+$  and  $n_-$  are imposed by the regulation 14 CFR 23. Based on the knowledge of the mission,  $n_+$  is imposed at 3 which is smaller than the minimum value defined by the expression of the regulation at paragraph 23.337(a). This choice is supported by paragraph 23.337(c) and the fact that the autonomous system is able to avoid maneuvers inducing load factors higher than 3. Then  $n_-$  is computed and its value is -1.2.





- Limit load factor :

The limit load factor is reach at the maximum stall velocity.  $n_{\text{limit}} = 3.17$

- Ultimate load factor :

The ultimate load factor which should not be exceeded by the aircraft is defined with a security factor of 1.5.

$$n_{\text{ultimate}} = 4.75$$

It can be verified that a minimum average velocity of 150 mph can be reached during the cruise phase as it is required in the request for proposal.

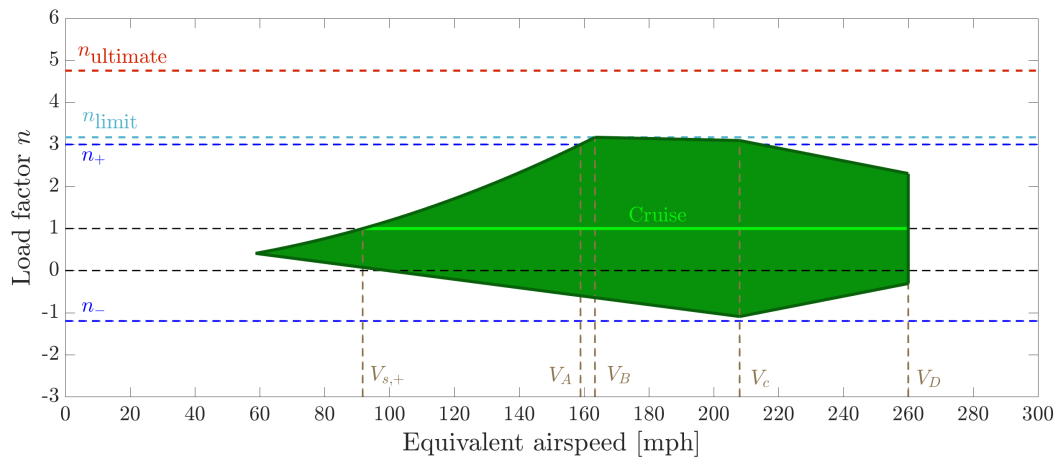


Figure 5.14: Flight envelope.

## 5.2.4 Typical mission performance

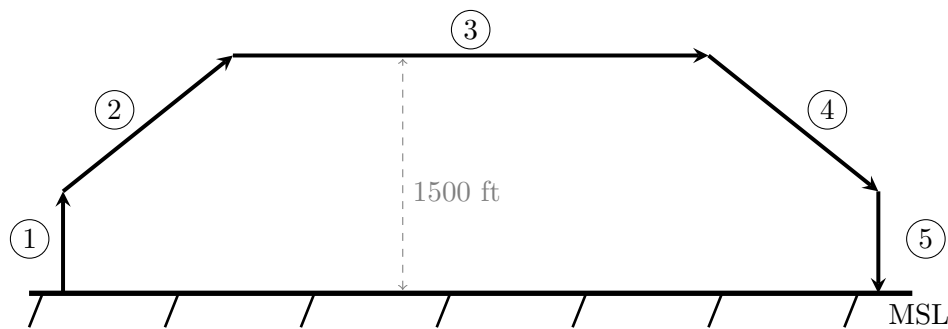


Figure 5.15: Different phases of the economical mission.





Mission phase	Time [s]	Mean Horizontal Speed [mph]	Mean Vertical Speed [ft/min]	Energy [MJ]	Lift to Drag Ratio [-]
Boarding	300	/	/	/	/
① - Hover up	30	0	100	15.55	/
② - Climb	174	150	500	33.81	10.96
③ - Cruise	720	150	0	97.23	11.14
④ - Descent	174	150	500	33.81	10.96
⑤ - Hover down	30	0	100	15.55	/
Unboarding	300	/	/	/	/
Charging time	480	/	/	/	/
<b>Total</b>	2208	/	/	215.45	/

**Table 5.2:** Performances of different phases of the economical mission.

A new mission is defined to assess the performance of the aircraft. This mission is closer to the reality than the sizing mission, which is far more restrictive. This mission is also the base of the pricing strategy and the assessment of costs relative to the electricity and the battery replacement. It is important to highlight that the lift to drag ratio is calculated according to the analytically drag study (Section 5.1.1). Power and energy requirements for different phases are displayed in Section 4.1.4.

## 5.2.5 Point performance requirements

In order to demonstrate the required point performances, it was necessary to verify, through the described BEM code (Section 4.1), that the motor and the batteries are able to provide enough power to satisfy the requirements for the following "tasks":

- Demonstrate "High, hot" takeoff and hover at 5,000 ft MSL with ISA +10 °C
- Demonstrate "High, hot" transition and climb with full payload after 50 ft hover at 5,000 ft MSL with ISA + 10 °C
- Demonstrate maximum speed of at least 176 mph with 50% of payload at a selected altitude between 1,500 - 3,500 ft MSL

For the "High, hot" takeoff and hover, it has been computed that the required power is around 127 kW for the motors on the wing and 32.5 kW for the motors on the canard. In comparison, in normal conditions at 0 ft MSL, they would be around 100 kW and 26 kW. However, the motors are powerful enough to meet requirements. Moreover, the total power





which will be required from the batteries is around 340 kW, also meeting the requirement since the 500.1 lb battery pack can provide a maximum of 390 kW.

For the "High, hot" transition and climb, the highest stress is put on the motor on the wing since, during the transition, it has to provide more thrust to overcome the loss in vertical force due to its rotation. In fact, the maximum power which is requested is 147.9 kW which is still under the peak power which can be provided by the motor. It is also important to analyze the total power requested by the batteries which, in this case, is around 380 kW which is at the limit of the capabilities of the battery pack.

Finally the maximum speed with 50% of the payload at an altitude of 2,000 ft is computed. In this case, the limiting factor is not the power of the motor, since it is massively overpowered due to the VTOL requirement. Instead, the maximum amount of torque which the motor is capable to transmit is limiting the maximum speed. Applying the motor's maximum torque, 184.4 ft·lbf, which through the gearbox becomes 1,106.4 ft·lbf, thanks to the BEM analysis, it is possible to demonstrate a maximum speed of 186.6 mph.

## 5.3 Structure

The structural analysis of the aircraft aims at designing the structural part of the aircraft. At first, the aerodynamic loads are computed. These loads directly influence the structure of the aircraft since the latter has to sustain to shear stress and the bending induced by these forces. Indeed, according to the magnitude of the loads, the number of stringers, the thickness of the fuselage skin and the number of frames are adapted. Finally, a finite element analysis based on the structural configuration defined analytically is performed.

For every computation, the Duckampus is considered as a mid-configuration between an acrobatic and a transporter aircraft. Therefore, the maximum pitching moment  $\ddot{\theta}$  is fixed to 60 deg/s and the maximum angle of yaw  $\psi$  is fixed to 22.5°. Moreover, for the computation of the skin thickness and the stringer section, another assumption is made. In fact, to get a value of the yield strength, it is compelled to employed a quasi-isotropic material. To achieve that, the material can be considered as a succession of layers oriented in different ways to be as isotropic as possible. It means that a fixed value of the yield stress can be used and is typically 43,511 psi

### 5.3.1 Maneuver envelope

For each component of the aircraft (wing, canard and fuselage), the loads are computed for several operating points. These points are defined by the maneuver envelope (see Figure 5.16) and each of them are labelled from A to F.





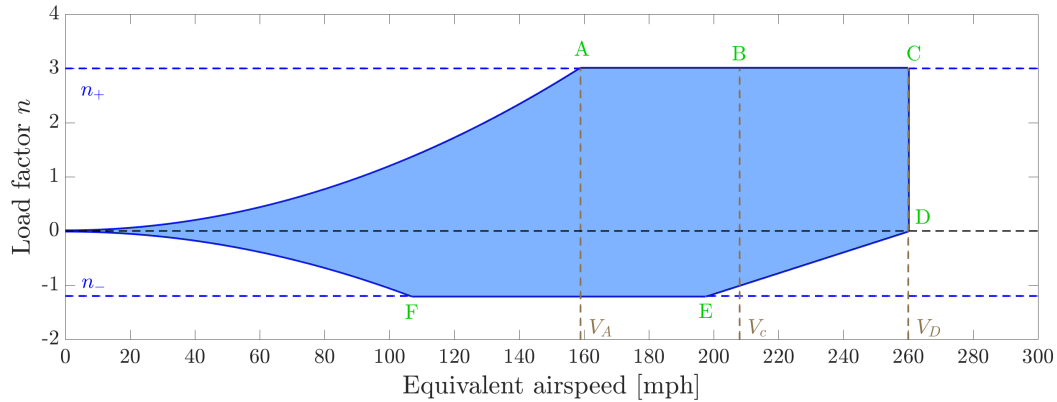


Figure 5.16: Maneuver envelope.

### 5.3.2 Aerodynamic and structural loads of the fuselage

At first, the aerodynamic loads of the fuselage must be computed. To do so, the different forces applied on the aircraft are depicted in Figure 5.17, where  $\gamma$  is the mounting angle of the wing.

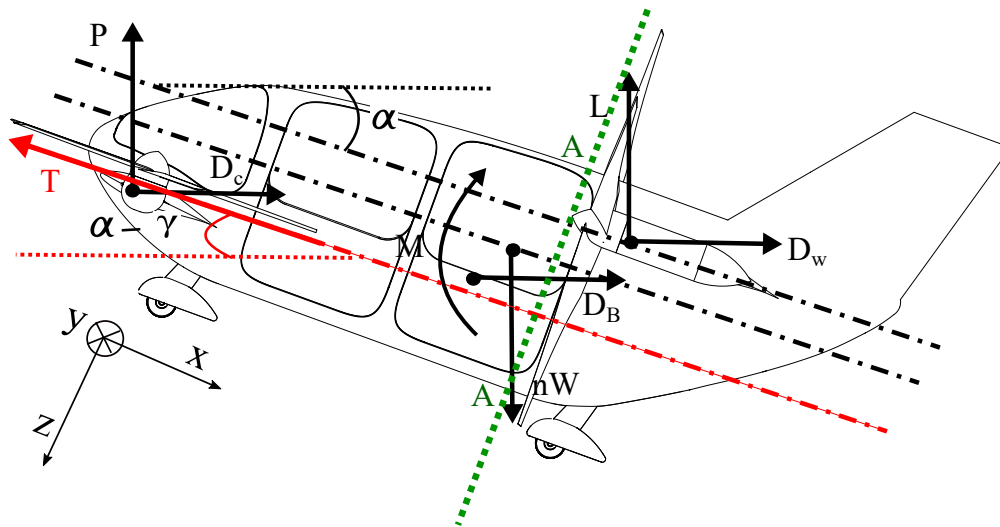


Figure 5.17: Layout of internal forces in the aircraft.

By applying force and moment equilibria, the aerodynamic loads ( $L$ ,  $P$  and  $M_{fus}$ ) corresponding to different configurations of the maneuver envelope are determined. Then, a cut is performed just before the wing and the reaction forces  $T_i$  and the bending moments  $M_i$  with  $i = x, y, z$  are calculated from the loads but only for the fuselage at 11.8 ft from the nose of the aircraft which stands for the AA-section. The numerical values are available in Tab. 5.3 and only the non-zero components are tabulated.





Case	$n$ [-]	$\alpha$ [°]	$L$ [lbf]	$P$ [lbf]	$M_{fus}$ [lbf.ft]	$T_x$ [lbf]	$T_z$ [lbf]	$M_y$ [lbf.ft]
A	3	15.6	10491	2330	4759	-977	-5388	-12348
B	3	11.68	10510	2383	5874	-606	-5496	-13112
C	3	5.68	10470	2512	9178	-8	-5658	-14593
D	0	-5	1368	-1281	9178	-181	1370	15173
E	-1.2	-12.39	-2093	-2892	5302	-1250	4104	27139
F	-1.2	-23.07	-1769	-2867	2168	-1995	3770	25059

**Table 5.3:** Aerodynamic and structural loads of the fuselage for different points of the flight envelope.

where  $T_y$ ,  $M_x$  and  $M_z$  are zero in all the flight configurations for the front part of the fuselage. This is normal since the moment caused by the fin offsets the moment of the wing.

### 5.3.3 Aerodynamic loads at the wing root and at the canard root

Now, in order to determine the loads at the wing and the canard roots, they are considered as beams upon which loads are applied. At first, loads acting on the wing are typically its self-weight and the weight of the batteries, the thrust and the weight of the engines, the lift and the drag of the wing. However, even if the lift and the drag are applied to the aerodynamic center of the wing, this latter is difficult to find since the distribution of lift on the wing is not analytically known. Therefore, the location of the point of application of the lift is found thanks to Tranair software. Let us note that the reference frame is composed of a  $x$ -axis pointing in the chord direction, a  $y$ -axis pointing towards the fuselage and the  $z$ -axis is perpendicular to both other axes. The loads at the wing root are depicted in Table 5.4

Case	$T_x$ [lbf]	$T_y$ [lbf]	$T_z$ [lbf]	$M_x$ [lbf.ft]	$M_y$ [lbf.ft]	$M_z$ [lbf.ft]
A	-1062	0	-3387	-19123	2379	-10514
B	-770	0	-3462	-19361	2937	-8391
C	-266	0	-3547	-19315	4589	-4687
D	-17	0	-896	-4157	4589	-3239
E	-376	0	140	1117	2651	-6276
F	-657	0	33	-100	1084	-10221

**Table 5.4:** Aerodynamic and structural loads at the wing root for different points of the flight envelope.

Concerning the canard, loads are different. In fact, the canard is submitted to its self-weight and the weight of the engines, its lift and drag. The reference frame is the same as the one of the wing. The loads at the canard root are depicted in Table 5.5





Case	$T_x$ [lbf]	$T_y$ [lbf]	$T_z$ [lbf]	$M_x$ [lbf.ft]	$M_y$ [lbf.ft]	$M_z$ [lbf.ft]
A	-111	0	-776	-1406	2379	-215
B	-64	0	-838	-1540	2937	-117
C	20	0	-982	-1702	4589	71
D	-82	0	430	1957	4589	-253
E	-359	0	1085	3438	2651	-1029
F	-578	0	1054	3141	1084	-1651

**Table 5.5:** Aerodynamic and structural loads at the canard root for different points of the flight envelope.

### 5.3.4 Structure of the aircraft

A first approximation of the aircraft structure (the number of stringers, the stringer areas, the skin thickness, the number of spars, the number of flanges, etc) is made for the Duckampus in order to withstand the computed loads. To perform this analysis in a fast and efficient way, the problem is idealized by using the panel and booms idealization. This method consists in replacing a skin panel with stringers by two booms that carry the direct stresses induced by the bending loads and one skin panel that carries the shear stresses induced by the shear and torque loads. Therefore, since the distances between two booms are small, the shear flow  $q$  is constant on each panel. This corresponds to an average of the exact shear flow distribution along the panel.

The stringers, idealized by booms, are made of CFRP and their area  $A_{boom}$  is a function of the material. Since the latter must only carry bending stress, the area is given by :

$$A = \frac{\max(\sigma_{xx}^i A)}{\sigma_{max}^{Alu}} \quad \text{with} \quad \sigma_{xx}^i A = \frac{(I_{zz/A} M_y + I_{yz/A} M_z) z_i - (I_{yz/A} M_y + I_{yy/A} M_z) y_i}{I_{yy/A} I_{zz/A} - I_{yz/A}^2} \quad (16)$$

where  $I_{yy/A}, I_{zz/A}$  are the equivalent second moment of inertia and  $i$  runs from 1 to  $N_b$ , the number of booms.

#### A. Stringer section and skin of the wing and canard

A flange is located at the most critical location which is the quarter-chord close to the aerodynamic center where the lift and drag (the loads) are applied. Then, after calculation of the worst loading case (Table 5.4 and 5.5) and using Eq. (16) with CFRP values, the minimum boom area is  $0.031 \text{ in}^2$  for the canard and  $0.1085 \text{ in}^2$  for the wing. The minimum thickness of the panels is also calculated from the shear flow computation for a closed thin-walled section. The methodology consists in computing with the Eq. (17) the shear flow of the two cells (c=I,II) by cutting them :





$$q_{0,c}^p = -\frac{I_{zz}T_z - I_{yz}T_y}{I_{yy}I_{zz} - I_{yz}^2} \left[ A \sum_{i:s_i \leq s} z_i \right] - \frac{I_{yy}T_y - I_{yz}T_z}{I_{yy}I_{zz} - I_{yz}^2} \left[ A \sum_{i:s_i \leq s} y_i \right] \quad (17)$$

where  $q_{0,c}^p$  is the shear flow of panel  $p$  of cell  $c$ . Then, a cut correction is computed by considering that the loads are applied to the shear center. That implies the torsion twist rate is zero. Finally,  $q^I$  and  $q^{II}$  are computed by adding the correction to all  $q_{0,c}^p$  in the corresponding cell. After calculating the shear center of the canard (or wing), the torsion moment contribution is added and the maximum shear flow of the canard (or wing) is computed. By considering the shearing strength value, the minimum thickness of the skin is  $t_{\min,c} = 5.512 \text{ th}^1$  for the canard and  $t_{\min,w} = 6.693 \text{ th}$  for the wing.

### B. Stringer section of the fuselage

The total structure of the front fuselage consists in stringers connected to one another and a skin of a given thickness. To ensure the aircraft to withstand loads whatever the maneuver envelope configuration, the worst case is once again considered for the computation (Tab. 5.3).

If the fuselage is assumed to be perfectly circular and thus symmetric, the area for all the booms is given by :

$$B = \left( \frac{M_y}{I_{yy}} z_{\text{boom}} - \frac{M_z}{I_{zz}} y_{\text{boom}} \right) \frac{1}{\sigma_{\max}} \quad (18)$$

where  $\sigma_{\max}$  stands for the maximum stress allowed in the stringers and B for the area of the booms. In the scope of this project, it is decided to work with CFRP stringers and with a safety factor of 1.5 to ensure the stability of the results. Using 36 zee-shaped stringers to avoid buckling, this yields a final value for the booms' area of  $0.0186 \text{ in}^2$ .

### C. Fuselage skin thickness

The skin of the fuselage must be thick enough to sustain the loads that are acting on the structure. To this end, the shear flow is evaluated for the worst loading case given that there is a discontinuity in shear flow while the shear flow is constant between two booms :

$$q^{i+1} - q^i = -\frac{T_z}{I_{yy}} B_i z_i - \frac{T_y}{I_{zz}} B_i z_i \quad (19)$$

This expression allows to take into account the shear flow due to both  $T_y$  and  $T_z$ . To these terms, a third has to be added which is the shear flow due to the torque but this term is not considered since  $M_x$  is zero.

All this development enables to find the maximum shear flow to end up with the minimum thickness for stringers. In fact, even if their number is quite large to avoid buckling, they must be able to sustain loads. And thus, the minimum thickness, that is directly related to  $q_{\max}$  and  $\tau_{\max}$ , is  $5.9 \text{ th}$ . In that sense, the final value of the thickness that is employed is about  $39 \text{ th}$  for the FEM analysis.

<sup>1</sup> 1 thou = 0.001 in





### 5.3.5 Finite element structural analysis

The CAD models of the lifting surfaces and fuselage are given in Figures 5.18, 5.19 and 5.20. whereas the structure characteristics are based on the analytical study previously done. This analysis is performed thanks to Siemens NX.

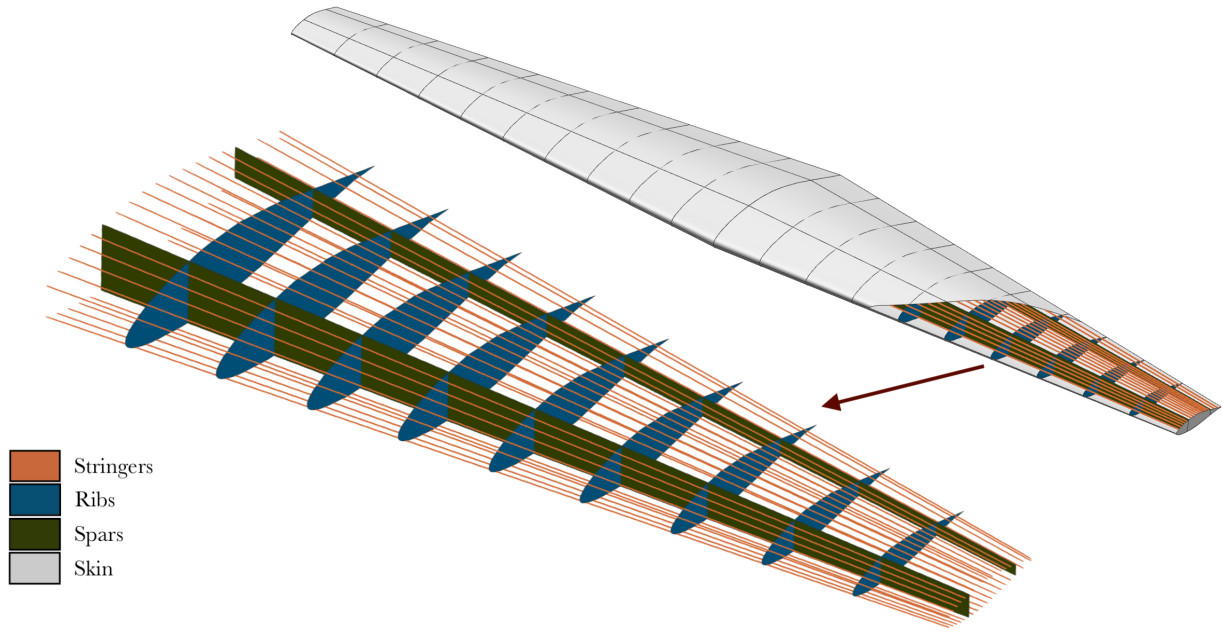


Figure 5.18: Canard CAD model provided by Siemens NX software.

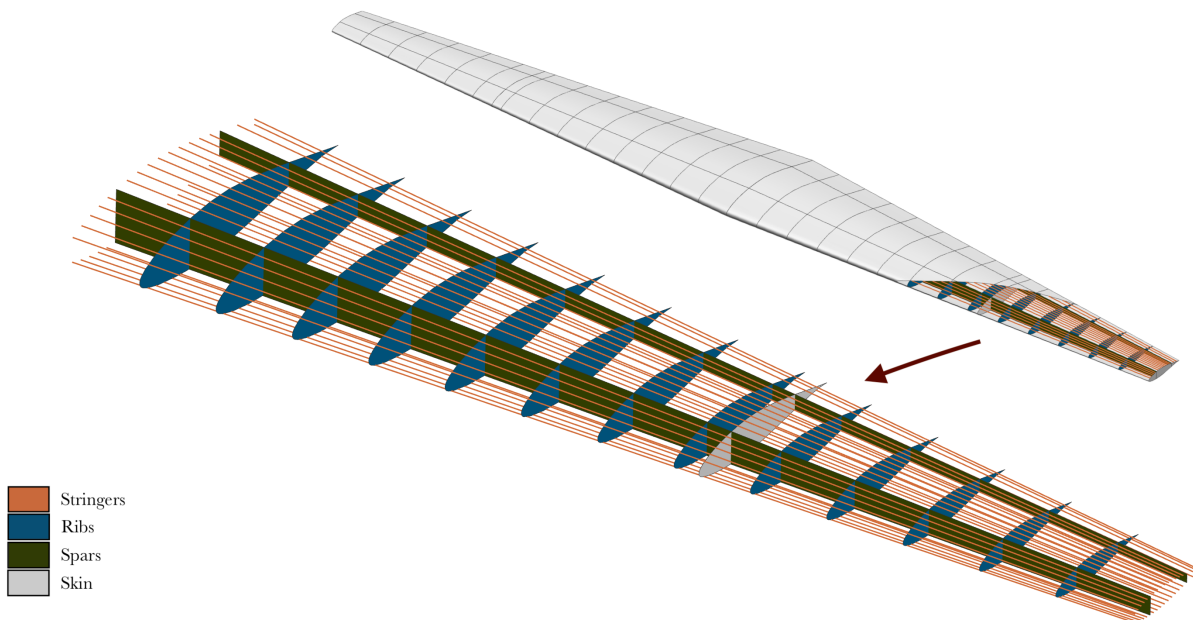
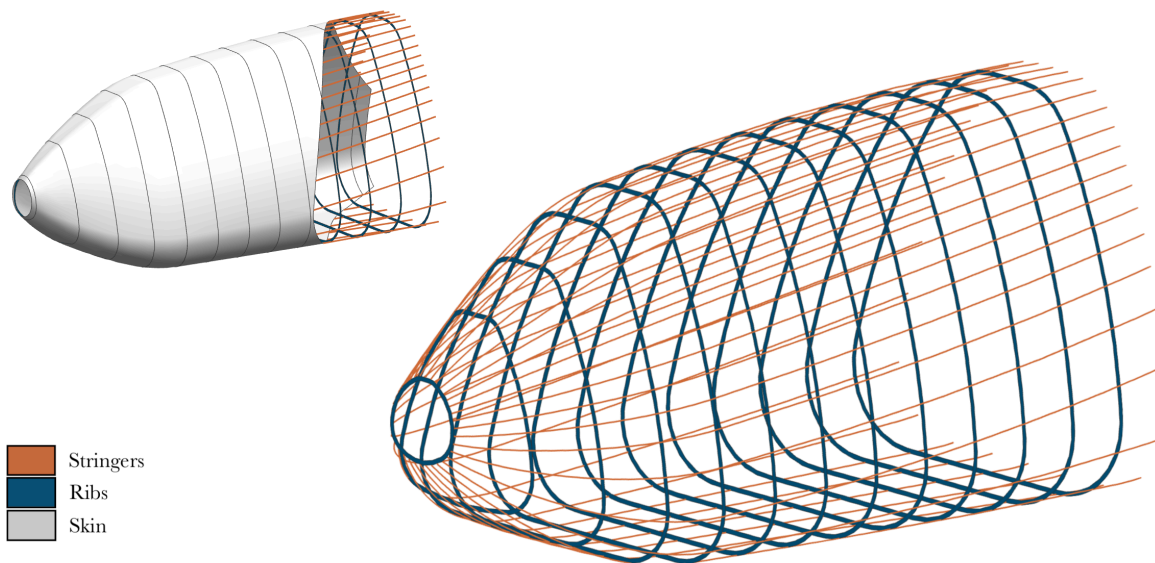


Figure 5.19: Wing CAD model provided by Siemens NX software.





**Figure 5.20:** Fuselage CAD model provided by Siemens NX software.

As it is defined previously, all the structural components of the lifting surfaces and the fuselage are made of CFRP and the zee-shaped stringers are chosen in the catalog provided by *Aircraft Extrusion Co.* [33].

### A. Canard

The material parameters implemented in the FE model for the canard are given in the Figure 5.21.

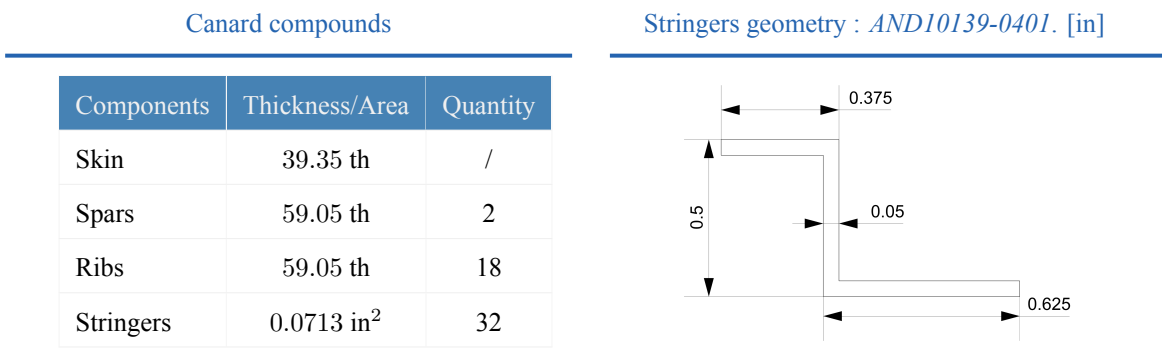


**Figure 5.21:** Summary of the canard compounds geometry.

Let us consider that the canard is fixed to the fuselage at its root and that the loads applied on the canard are its own weight, the weight of the motors at the tips and pressure forces. The pressure distribution corresponds to a case where the angle of attack of the aircraft is  $14^\circ$  and is provided by *Trana.ir*. The latter is multiplied by the maximal load factor sustained by the aircraft in order to study the most critical case. Finally, no additional loads are induced by the motors since they are shut down during the cruise phase.





According to the deformation displayed in Figure 5.22, it can be concluded that the most significant displacements are in the  $z$ -direction. These deformations are due to the bending induced along the span. Moreover, the maximum deflection is located at the tips of the canard and its value reaches 0.47 in.

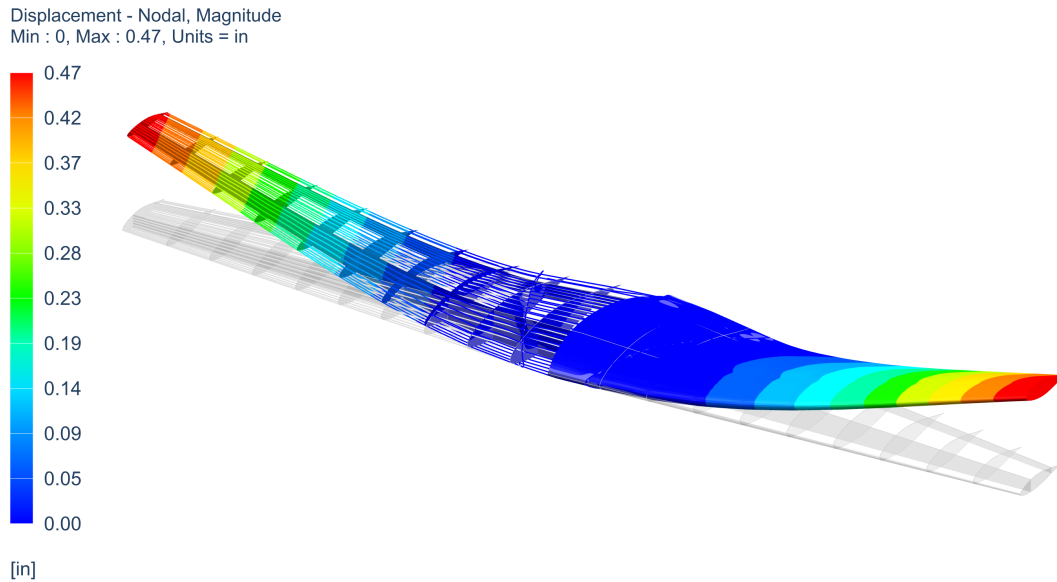


**Figure 5.22:** Displacements undergone by the canard structure for the most critical case compared to the unload case (gray part). Scaling of the displacements of 10% of the model size.

For their part, the principal stress values vary between  $-40,610.6$  psi and  $42,060.9$  psi (Figure 5.23). These values fit well with what is obtained in the analytical analysis. In fact, in this latter, it was considered that the yield strength of the CFRP was above the limit measurement of the FEM analysis. The figure also demonstrates that the maximum principal stress appears in the spars. They are located on a line which is clamped since it represents the connection between the canard and the fuselage. Once again, the value reached there is below the tensile strength of selected material.



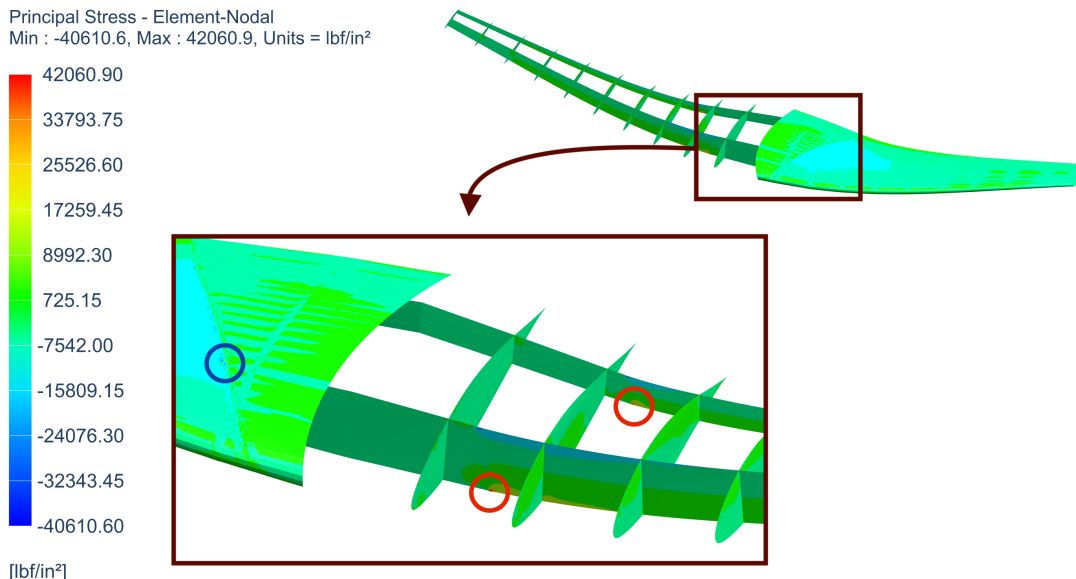


**Figure 5.23:** Principal stress distribution through the canard structure for the most critical case. The maximum values reached through the skin and the structure are highlighted with thick red circles whereas the minimal ones are highlighted with thick blue circles.

### B. Wing

The material parameters implemented in the FE model for the wing are given in the table in Fig. 5.24.

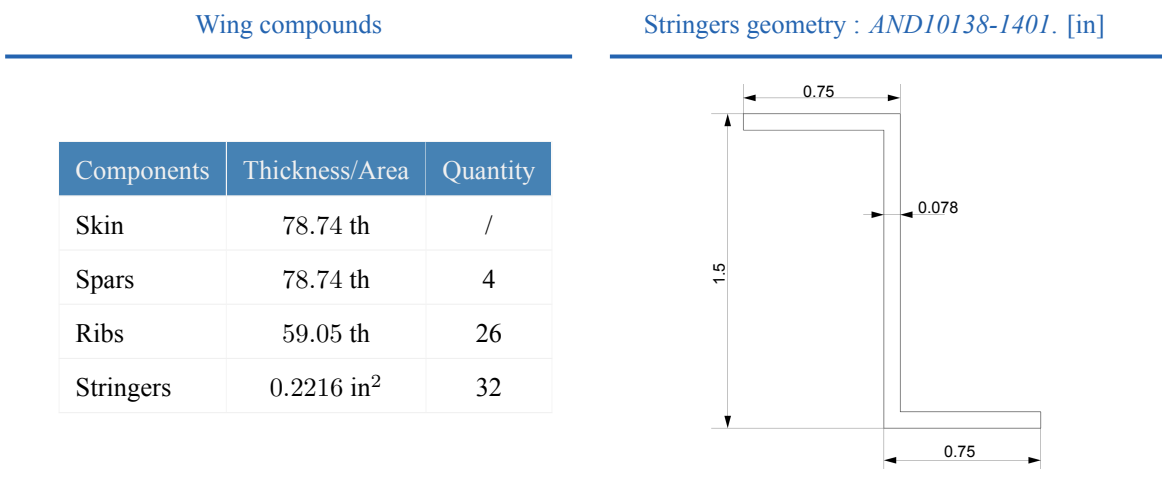


**Figure 5.24:** Summary of the wing compounds geometry.

The model of the wing includes the fact that the wing is composed of two parts : a fixed and a rotating. In order to simulate the connection between the two parts with the shaft, a common section is fixed. Moreover, the repartition of the 26 ribs among the the parts is the following : the fixed part contains 16 ribs and the rotating one contains the 10 remaining.

The boundary conditions are the same as for the canard, i.e., the wing is clamped at the junction with the fuselage.







The loads applied on the wing are its own weight and the weights of the motors at the tips. In addition, a reaction torque due to the rotation of the motors must be considered. Besides, the motors produce the thrust needed for the cruise phase and it must be added at the wingtips. To perform the analysis, the reaction torques and the thrust are chosen as the maximum reachable by the motors in order to work with the most critical case. These values are available in Table 4.2. Moreover, since the batteries are stored in the wing, the total battery weight is then added and distributed over the storage area. The pressure distribution is imported from `Tranair` and corresponds to a case where the angle of attack of the aircraft is  $14^\circ$  and then is multiplied by the maximal load factor sustained by the aircraft.

Once again, the deformations are mostly along the  $z$ -axis due to the contribution of the lift distribution and the reaction torque (Figure 5.25). The maximum deflection is located at the wingtips and its value reaches 2.16 in.

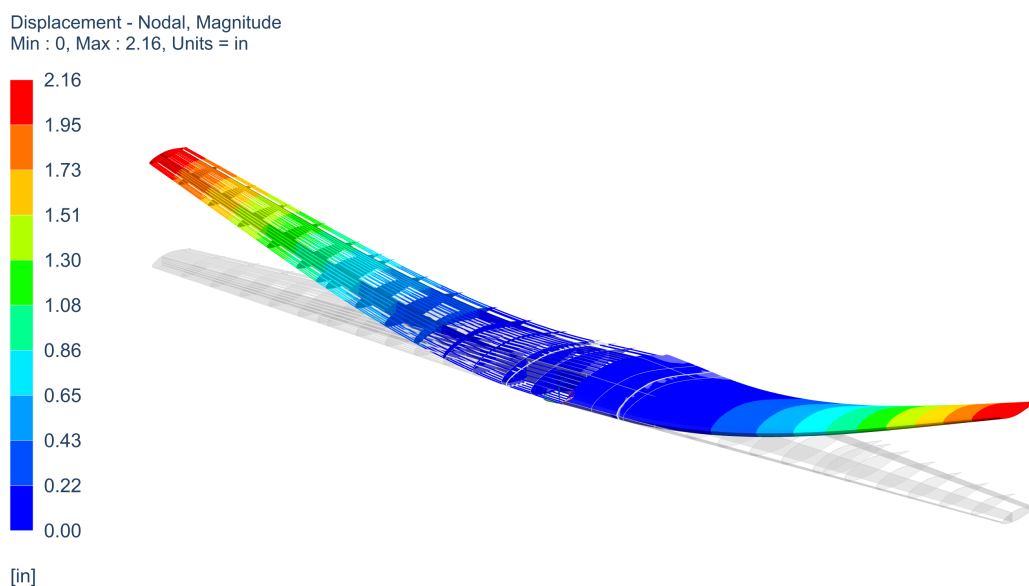


**Figure 5.25:** Displacements undergone by the wing structure for the most critical case compared to the unload case (gray part). Scaling of the displacements of 10% of the model size.

The principal stress values vary between  $-24,626.6$  psi and  $39185.1$  psi. The maximum principal stress on the skin is located on the bottom side of the wing. It can also be seen that the maximum principal stress appears in the spar located near the leading edge of the wing. The maximal value reached over the structure is far below the tensile strength of CFRP.



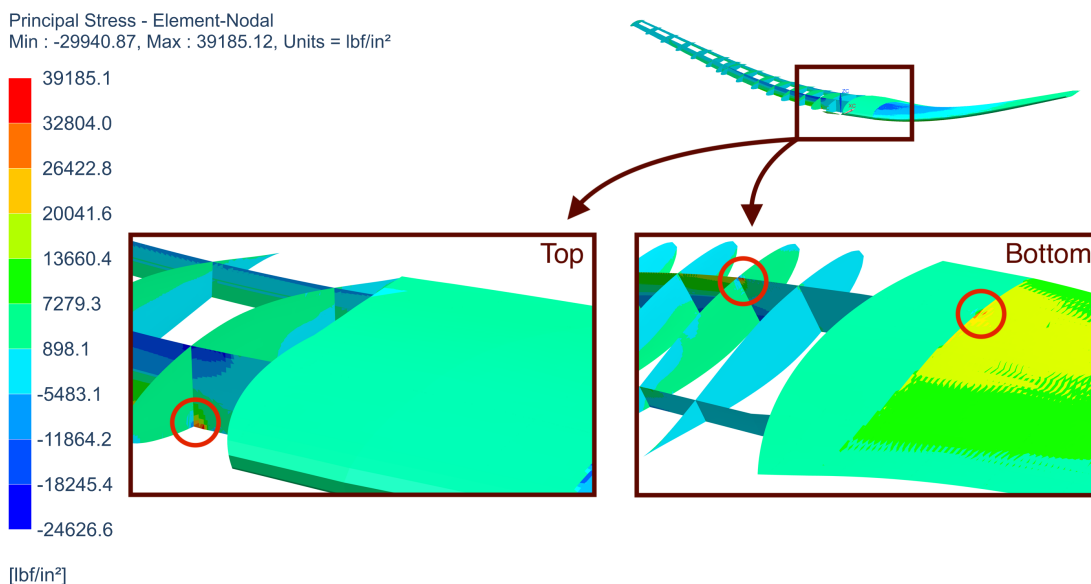


**Figure 5.26:** Principal stress distribution through the wing structure for the most critical case. The maximum values reached though the skin and the structure are highlighted with thick red circles.

### C. Analysis of the fuselage

The material parameters implemented in the FE model for the fuselage are given in the Table of Fig. 5.27.

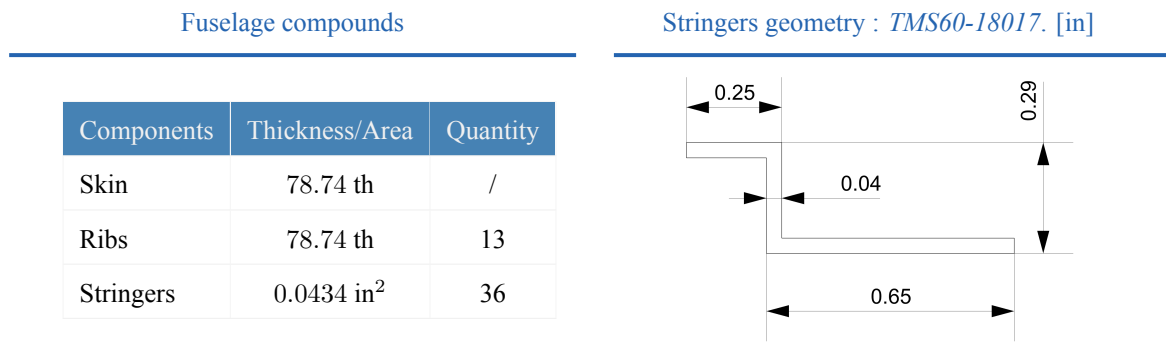


**Figure 5.27:** Summary of the Fuselage compounds geometry.

The loads applied directly on the front section of the fuselage is its own weight and an acceleration along the  $z$ -axis corresponding to  $3g$  since the section of the fuselage is analyzed when it undergoes the most critical loads. The weight of the canard is added to the model as well as the lift it produces. The motors mounted on the canard tips are taken into account through the addition of their weight and a torque at the connection between the fuselage and the canard. The weight of the passengers is also added.

Figure 5.28 depicts the deformations of the structure when it is submitted to the previously defined loads. The maximum displacement is located at the middle section of the fuselage and reaches 0.19 in. The distribution of the displacements emphasizes that the deformation near the nose of the aircraft is really small.



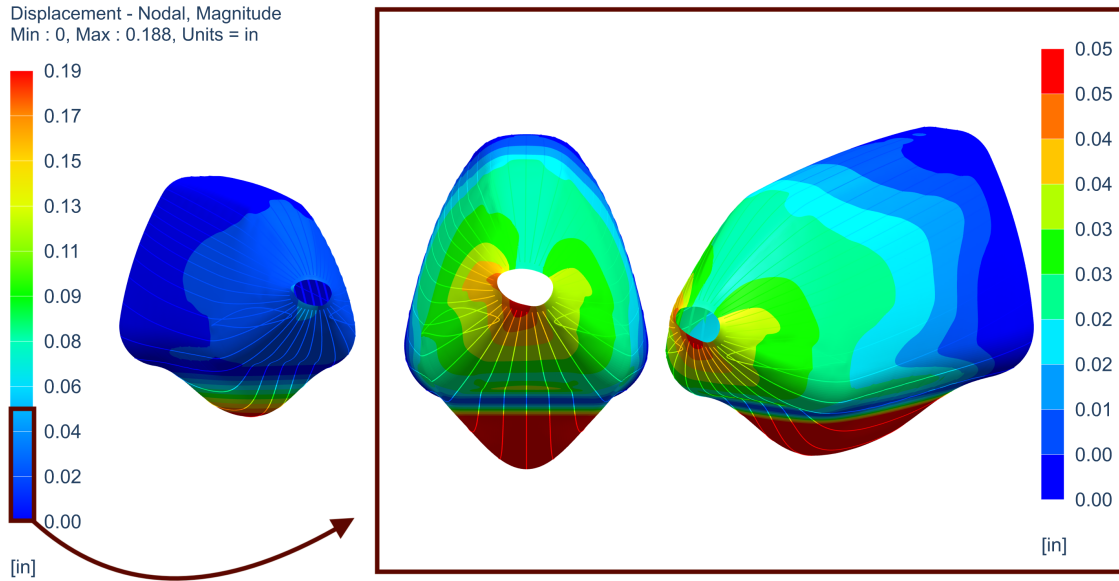


**Figure 5.28:** Displacements undergo by the fuselage structure for the most critical case. Scaling of the displacements of 10% of the model size.

Concerning the principal stress, the highest absolute value appears in the ribs and reaches 13,903.99 psi. This latter is quite close to the tensile strength of the material used for the ribs but does not exceed it.

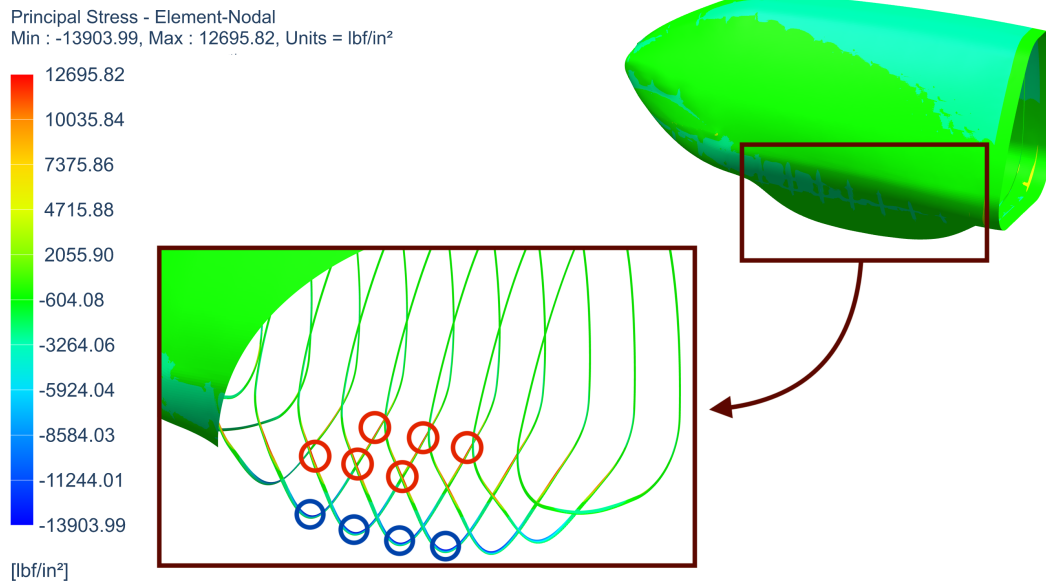


**Figure 5.29:** Principal stress distribution through the fuselage section structure for the most critical case. The maximum values reached through the skin and the structure are highlighted with thick red circles whereas the minimal ones are highlighted with thick blue circles.

#### ***D. Comparison with analytical study***

For the FE analysis, the choice is done to use stringers of bigger areas than the ones computed by the analytical study.





This choice is supported by the error margin induced by the assumptions behind the analytical study. The limitation in the choice of geometries proposed by the catalog of *Aircraft Extrusion Co.* [33] also prevents employing stringers with the exact area.

Concerning the canard and the fuselage, the results from the analytical study fit well the ones coming from the FE analysis. Indeed, leading simulations with parameters close to the minimum stringer areas and skin thicknesses returned from the analytical study provide result which assure the integrity of the structures.

Considering the wing, the observations are a bit different. Due to the complexity of its structure (i.e. tilt-wing), the analytical study does not provide relevant minimum values of stringer area and skin thickness. Indeed, the disconnection of the stringers, the spars and the skin between the fixed part of the wing and the rotating one is not take into account in the analytical study. After few simulations for different combinations of stringer area and skin thickness, it appears that the required stringer area is at least twice higher than the value predicted by the analytical study while a skin thickness of 78.74  $\mu\text{m}$  is sufficient.

## 5.4 Static stability

The static stability of the Duckcampus aircraft (i.e. a canard-body-wing aircraft) is investigated through the static margin  $K_n$  which stands for the mean-geometric-chord-normalized distance between the aircraft center of gravity (CG) and the neutral point (NP). The aircraft is statically stable if  $K_n \in [5 \ 15] \%$  for enough maneuverability and stability according to FAA requirement. All calculations are carried out for a trim configuration with a fixed elevator deflection  $\delta_e$ . Thereby, the engine contribution is ignored for this study.

### 5.4.1 Neutral point

The neutral point is defined as the aerodynamic center of the full aircraft. Eq. (20) gives its position [34]:

$$\frac{\text{NP}}{\bar{c}} = \frac{S_c h_{c0} C_{Lc\alpha} + S_w C_{Lw\alpha} \left(1 - \frac{d\varepsilon}{d\alpha}\right) \left(\frac{\partial C_{mfus}}{\partial C_L} - h_{w0}\right)}{S_w C_{Lw\alpha} \left(1 - \frac{d\varepsilon}{d\alpha}\right) + S_c C_{Lc\alpha}} \quad (20)$$

where  $h_{w0} \bar{c}$  and  $h_{c0} \bar{c}$  are the distances from the wing leading edge to the canard and wing aerodynamic centers, respectively. Moreover, by employing empirical expression [29] the effect of the fuselage is accounted for:

$$\frac{\partial C_{mfus}}{\partial C_L} = \frac{K_f (w_{fus})_{\max}^2 (l_{fus})_{\max}}{S \bar{c} C_{L\alpha}} \quad (21)$$

The downwash induced by the canard on the wing is modelled as a linear relationship between downwash angle and angle of attack with slope:  $\frac{d\varepsilon}{d\alpha}$  which is determined from the Tranair simulation at cruise conditions. Fuselage downwash





effects on the wing is calculated from the empirical expressions of USAF DATCOM [35].

When the geometries of all the components are fixed in the design section, the only remaining parameter to choose corresponds to  $h_{c0}\bar{c}$ . When this parameter varies, there are impacts on the CG and on the NP position. Then,  $h_{c0}\bar{c}$  must be chosen such that the static margin is in the admissible domain.

## 5.4.2 Static margin estimations

The center of gravity of the AEVTOL Duckampus aircraft depends only on the payload. Fig 5.30 plots the position of the neutral point and the range of positions of the center of gravity, between two extremes denoted by 1 and 2. These extremes correspond to the cases where only the front seats are occupied and only the rear seats are occupied, respectively. All other payload cases result in CG position between these two extremes. Therefore, the aircraft is stable in all configurations.

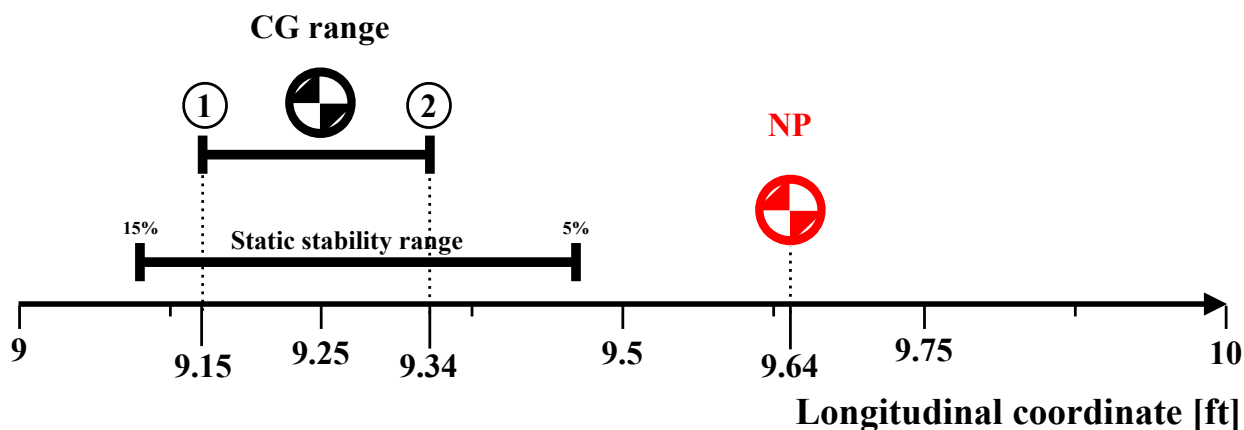


Figure 5.30: CG range, aircraft aerodynamic center and comparison with the static stability range.

## 5.5 Dynamic stability

This section is dedicated to the the dynamic stability of the Duckampus aircraft. All the stability and control derivatives are computed for the cruise phase at 1,500 ft and Mach 0.19 with the maximum take-off weight. The USAF DATCOM employed and adapted to a canard-body-wing configuration by treating the canard as the wing and the main wing as the horizontal tail [35]. Then, the linearized longitudinal and lateral equations of motion are set up and solved.

### 5.5.1 Stability derivatives

The values of all the stability derivatives are given in Table 5.6:





Longitudinal derivatives	Cruise phase	Lateral Derivatives	Cruise phase
$C_{L_\alpha}$	5.72	$C_{n_\beta}$	0.0959
$C_{D_\alpha}$	0.99	$C_{l_\beta}$	0
$C_{m_\alpha}$	-0.6890	$C_{y_\beta}$	-0.7161
$C_{L_u}$	0.026	$C_{y_v}$	-0.7844
$C_{D_u}$	0	$C_{l_v}$	0.0167
$C_{m_u}$	0	$C_{n_v}$	0.0725
$C_{L_q}$	-3.97	$C_{y_p}$	-0.0763
$C_{D_q}$	0	$C_{l_p}$	-0.4649
$C_{m_q}$	-24.96	$C_{n_p}$	0.0195
$C_{L_{\dot{\alpha}}}$	3.97	$C_{y_r}$	0.1918
$C_{D_{\dot{\alpha}}}$	0	$C_{l_r}$	0.2111
$C_{m_{\dot{\alpha}}}$	-6.21	$C_{n_r}$	-0.0707

**Table 5.6:** Longitudinal and lateral stability derivatives at maximum take-off weight.

The linearized equations can be rewritten in the following matrix form :

$$\dot{\mathbf{x}} = \mathbf{Ax} + \mathbf{Bu} \tag{22}$$

where  $\mathbf{A}$  is the matrix constructed by the stability derivatives and  $\mathbf{B}$  by the control derivatives which are computed in the control derivative section 5.5.2. The control inputs are contained in the vector  $\mathbf{u} = [\delta e, \tau, \delta A, \delta R]^T$  where  $\delta e, \delta A, \delta R$  are the deflection angle of elevator, aileron and rudder, respectively and  $\tau$  is the thrust perturbation. Finally, when Eq. (22) is solved, the vector  $\mathbf{x}$  is computed at each time step and the response of the system to a perturbation is characterized by the eigenvalues of matrix  $\mathbf{A}$ . Therefore, the system is dynamically stable when the eigenvalues of the system have negative real parts and that is confirmed as shown in Table 5.7 :

Longitudinal	Lateral
-0.4424 - 0.4156 i	-0.1948 - 1.1283i i
-0.4424 + 0.4156 i	-0.1948 + 1.1283i
-0.0052 - 0.0143 i	-3.8538 + 0.0000i
-0.0052 + 0.0143 i	-0.0672 + 0.0000i
	0.0000 + 0.0000 i

**Table 5.7:** Eigenvalues of matrix  $\mathbf{A}$  for longitudinal and lateral derivatives.





## 5.5.2 Control derivatives

In this section, all the control derivatives with respect to the elevator deflection  $\delta e$ , rudder deflection  $\delta R$  and aileron deflection  $\delta A$  are computed. The first step consists in sizing the control surfaces. The considered primary control surfaces are : elevator on the canard, ailerons on the wing and rudder on the fin. In that sense, their moment arm (Fig. 5.31) and their geometry (control surface span to lifting surface span ratio  $b_{Cont}/b_{Lift}$  and control surface chord to lifting surface chord ratio  $c_{Cont}/c_{Lift}$ ) are listed in Table 5.8.

	Ailerons	Elevator	Rudder
$b_{Cont}/b_{Lift}$ [-]	0.13	0.7	1
$c_{Cont}/c_{Lift}$ [-]	0.22	0.24	0.2
$b_{Cont}$ [ft]	2.391	5.755	4.63
Moment arms [ft]	$l_A = 13.12$	$l_e = 6.56$	$l_{R,1} = 3.55$ $l_{R,2} = 9.22$

**Table 5.8:** Characteristics of control surfaces.

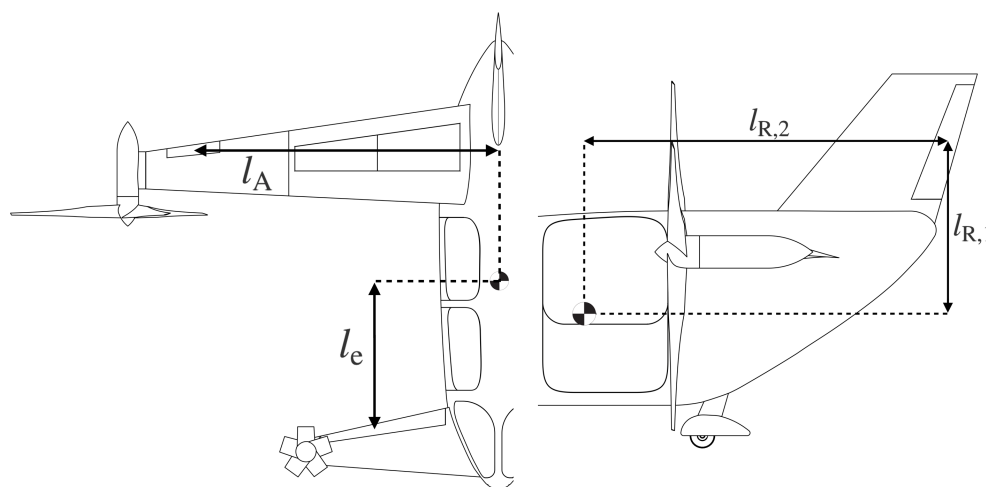


**Figure 5.31:** Moment arms of control surfaces.

Control surface design takes into account three fundamental requirements : stability, controlability and occupant comfort. Therefore, it must be designed such that the aircraft possesses an acceptable flying qualities anywhere in its flight envelope. Note that the handling qualities are directly linked to the desired hinge moment applied to overcome the aerodynamic moments produced by the control surface deflection. Then, the recommendations MIL-STD-1797 are followed to design the surface control.





CLASS I	Small, light aircraft with low manoeuvrability
CATEGORY B-C	Different flight phases
LEVELS OF ACCESSIBILITY 1-2-3	Ability to complete the mission

1. **Ailerons:** Roll or lateral control requirements define the aileron design. According to MIL-F-8785C, the design requirements specify that the aircraft must achieve a bank angle of  $45^\circ$  after 2.5 seconds in response to a step function in roll command. Note that the roll rate requirement is governed by section 23.157 of Part 23 of FAR for a GA aircraft. These requirements lead to the aileron dimensions in Table 5.8 and to the control derivatives in Table 5.9. Note that the side force due to aileron deflection is usually small and is neglected [36] and the yawing moment  $C_{n_{\delta_A}}$  arises from the drag due to the ailerons and experimental data.
2. **Elevator:** The elevator is designed from the trim requirements within flight envelope. When the canard lift changes, the total aircraft lift is also modified and the aircraft adopts a new trim configuration.

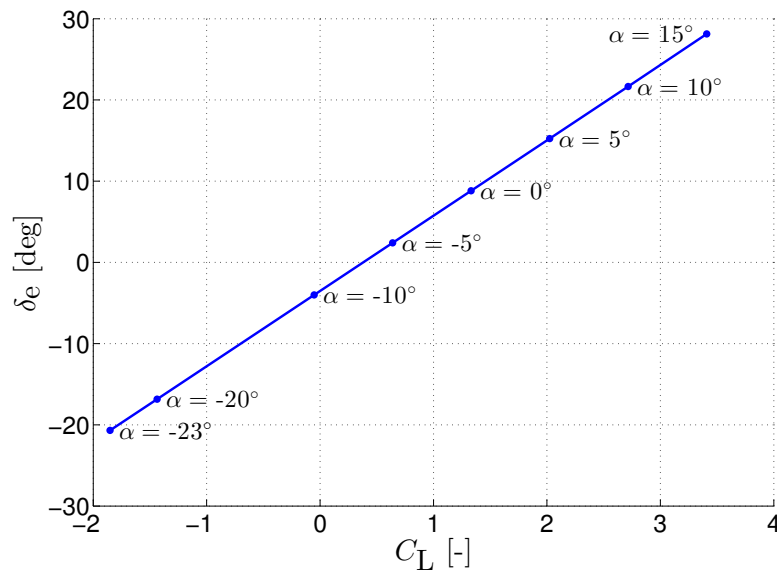


Figure 5.32: Trim Analysis ( $C_m = 0$ ) for different angle of attack within the flight envelope.

Then, in Figure 5.32,  $\delta_{e_{max}}$  is determined from the limits of the flight envelope. Then, the elevator geometry is determined to have  $C_{m_{\delta_e}}$  to trim the aircraft in the entire flight envelope.

3. **Rudder:** The rudder is designed using the regulation for GA aircraft in FAR 23. The most critical case corresponds to an engine failure (asymmetric thrust case). Then, the rudder dimensions are computed to recover the yawing moment due to the asymmetric thrust.







Ailerons	Elevator	Rudder
$C_{y_{\delta A}} = 0$	$C_{m_{\delta e}} = 0.53$	$C_{y_{\delta R}} = -0.1863$
$C_{L_{\delta A}} = 0.0763$	$C_{m_{\delta e}} = 1.19$	$C_{l_{\delta R}} = -0.0199$
$C_{n_{\delta A}} = /$		$C_{n_{\delta R}} = 0.0499$

**Table 5.9:** Control derivatives.

and these derivatives complete the matrix **B** in Eq. (22).

### 5.5.3 Longitudinal flying qualities

The longitudinal response of the Duckampus aircraft comprises two modes: short-period mode and a long-period mode (phugoïd mode). The levels of accessibility are determined based on the analysis of flying qualities according to Mil-F-8785c [37].

	Short-period	Phugoïd
Frequencies	$\omega_s = 0.607$	$\omega_p = 0.015$
Damping ratio	$\zeta_s = 0.729$	$\zeta_p = 0.342$
Levels of accessibility	1	1

**Table 5.10:** Characteristics of longitudinal mode of vibration and associated flying qualities.

### 5.5.4 Lateral flying qualities

The lateral response of Duckampus aircraft comprises oscillatory mode and two non-oscillatory modes: Dutch-roll mode, Roll subsidence mode and spiral mode, respectively which are represented through the eigenvalues of the lateral matrix **A** in Table 5.7.

- Dutch-roll mode:  $\lambda_{1,2} = -0.1948 \pm 1.1283i$  ( $\omega_{dr} = 1.145rad/s$ ,  $\zeta_{dr} = 0.170$  and  $\omega_{dr} \zeta_{dr} = 0.195rad/s$ ).
- The non-oscillatory mode is associated to the roll subsidence mode (High damping mode  $\lambda_3 = -3.8538$ ) and the spiral mode (Light damping and unstable mode  $\lambda_4 = -0.0672$ ). For the roll mode, the predicted time to get the half amplitude is 0.18 s. Thereby, for the spiral mode, it takes 10.31 s to double the amplitude.

By considering the Dutch roll flying qualities with  $\omega_s \zeta_s$  value, the aircraft does not encounter any problem with the Dutch roll mode according to Mil-F-8785c. And this is also the case when considering the roll mode. Then, a level of accessibility for these modes is 1 and finally, for the spiral mode, the level of accessibility is 2.





## 5.6 Transition phase

### 5.6.1 Transition phase parameters variation

Among the different phases of the flight, in the case of an EVTOL, the transition phase from hovering to vertical flight or climb is the most critical one (Top of hovering). The variation of the relevant parameters is computed in order to design the rotation system. First, the true airspeed variation is imposed to a trigonometric function respecting some important conditions. For example the variation must be smooth and the derivatives at the boundaries must be equal to zero. The acceleration is thus also fixed. These two functions are given in Fig. 5.33 in function of time. From this, the aerodynamic forces are deduced and Newton's law is applied on the overall system. This equation takes into account the lift increase as the aircraft accelerates (also considering the orientation of the tilt wing). The main goal of this study is to determine the rotation speed of the propeller at the back. To do so, the required thrust must first be computed.

The solved Newton's law along the vertical and horizontal directions are given by Eq. (23) and Eq. (24).

$$L + T_{\text{back}} \sin(\Psi) + T_{\text{front}} - W = 0 \quad (23)$$

$$-D + T_{\text{back}} \cos(\Psi) + M a = 0 \quad (24)$$

where  $T_{\text{back}}$  is the thrust of the back propellers and  $T_{\text{front}}$  is the thrust of the front propellers,  $\Psi$  is the tilt angle,  $W$  and  $M$  are the weight and mass of the aircraft,  $L$  is the lift and  $D$  is the drag of the aircraft.

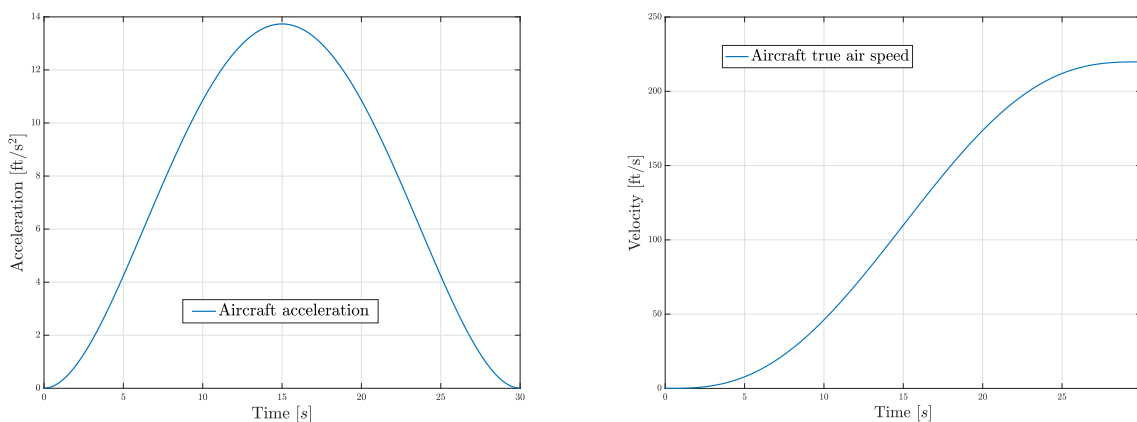


**Figure 5.33:** Variation of the speed and acceleration of the aircraft during the transition phase.



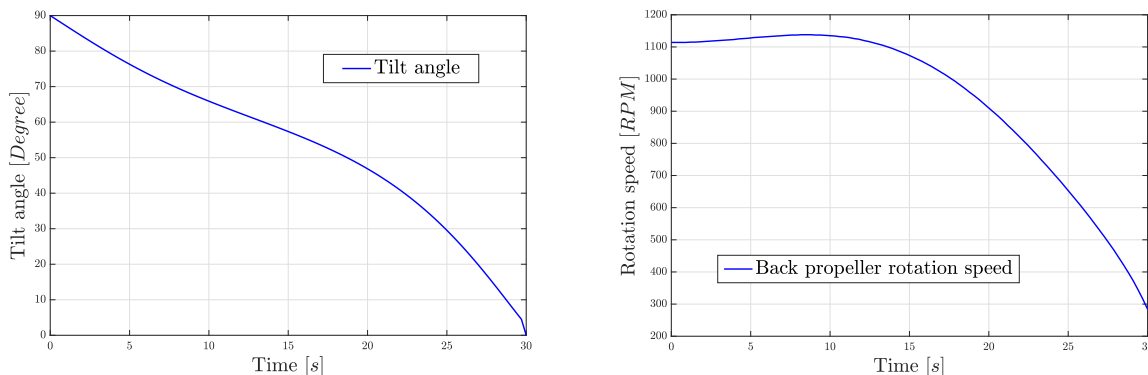


Figure 5.34: Variation of the propeller parameters during the transition phase.

In order to reach the imposed acceleration, the tilt angle variation is also imposed from Newton’s law. This angle is described as the angle between the longitudinal axis of the aircraft and the rotation axis of the propeller. In this way, it is equal to 90° during the hovering phases and is equal to 0° in cruise. From this, the propeller parameters are computed. In particular, the rotation speed is given in Figure 5.34. These different parameters are intended to be automatically set by the autonomous system of the aircraft.

## 5.6.2 Shaft sizing

The rotation of the two tilt wing parts will be performed by an additional electrical motor inside the aircraft, through a shaft. The design of these elements needs to be carried out considering the transition parameters found previously. In particular, the torque that the motor has to produce to tilt the shaft needs to be computed. The two rotors turn in opposite directions in order to induce zero net torque in the roll direction on the aircraft, as shown in Figure 5.35. The tilt-wing motor’s torque is thus really small since it just needs to rotate the static inertia of the shaft and the motors. Eq. (25) gives the mathematical expression of the conservation of the angular momentum.

$$\mathbf{L} = I \mathbf{w} \quad w_1 = w_2 \quad |\mathbf{L}_1 + \mathbf{L}_2| = I (w_2 - w_1) = 0 \quad (25)$$

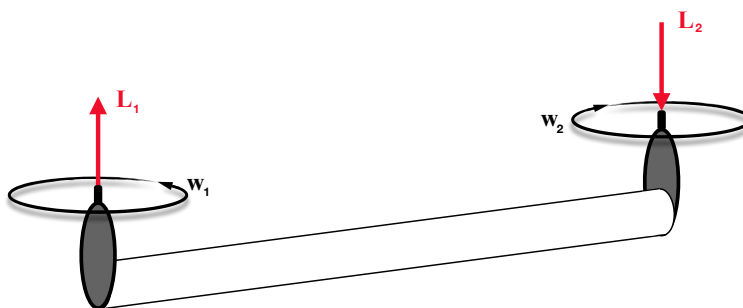
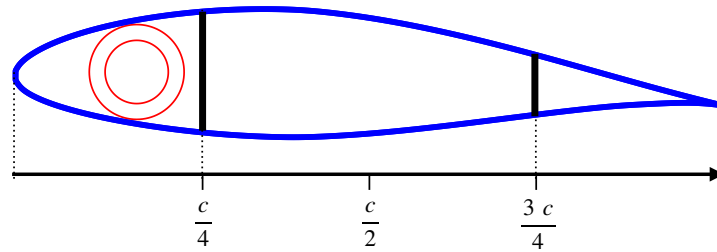


Figure 5.35: Illustration of the compensation of the kinetic momenta.





In addition to this, the diameter and shape of the shaft also need to be designed. Thanks to the thick airfoil, the space inside the wing is big enough to contain the shaft. From the previous calculation, a hollow cylinder with an external diameter of 4.72 in and thickness of 0.787 in is chosen. The material chosen for this shaft is High Strength Carbon fibers / Epoxy composite [38]. The mass of this shaft is computed (132 lb) and previously integrated into the total weight calculation. In order to verify the integration of the shaft into the wing, the section located at the wingtip and the shaft are plotted in Figure 5.36.



**Figure 5.36:** Illustration of the integration of the shaft into the wing.

The only part of the structure that is making the connection between the fixed part and the rotating part of the wing is the shaft. The moving part of the wing could bend and come in contact with the fixed part of the wing at the interface. At this point, the shaft is reinforced: the shaft is filled and a complete bearing system is used in order to make the transition from fixed to rotating wing. This enables to avoid the problem of the contact described previously and also enables the wing to sustain one part of the load created by the tilted part.

## 6 Autonomous flight and navigation

### 6.1 Safety justification

According to a study realized by the Boeing Company [39], 80 % of the accidents are caused by human errors. Tactical errors caused by fatigue, inebriation or lack of experience and operational errors related to problems with training of the pilots are the main issues that are considered as human errors. Even if some additional issues (software failure, software hacking, overheating) could be linked to the integration of an autonomous system in the aircraft, they are counterbalanced by an important increase in safety. Concerning the remaining 20 %, electrical motors are generally safer than combustion motors due to the reduced number of moving parts and the simplicity of the system. To conclude, if a very sharp maintenance process and an evolution in the autonomous modules safety are taken into account, such an aircraft would be very safe.





## 6.2 Market justification

The expansion of the autonomous sector has been estimated in a global forecast for 2030 [40]. It turns out that the autonomous aircraft market is projected to grow from \$3.6 billion in 2018 to \$23.7 billion in 2030. This corresponds to a compound annual growth rate of about 17 %. Knowing this growth estimation, the concept of a future aircraft cannot be imagined without the integration of an autonomous module.

The specific economic aspect linked to the business model of an aircraft is also very important. An autonomous aircraft means that the pilot can be removed. This has three fundamental consequences. Firstly, the weight of the pilot and all the weight linked to him can be removed. This means a reduction of the flight equipment and display systems as well as a reduction of the cockpit length. A reduction of the weight of an element in the aircraft means a general larger reduction of the weight and the price. Secondly, the pilot salary, that is about \$85, 418 per year [41] in the USA, is not necessary. Thirdly, the pilot can be replaced by an additional passenger which will pay for the flight and thus contribute to the general source of revenues.

## 6.3 Existing autonomous vehicles

The world most popular autonomous vehicle is the Tesla car [42]. Equipped with a large number of panoramic video cameras and twelve ultrasonic sensors, this car is able to see through heavy rain, fog, dust and even through another car. Even if they currently offer only an autopilot service, Tesla will soon release a fully autonomous system with an integrated decision center. It will only require the destination as well as some mission parameters. As already mentioned previously, existing aircraft are already partially autonomous with their autopilot systems.

## 6.4 Level of autonomy

The choice of a decisional autonomous plane is made. A summary of all tasks that are thus operated autonomously is presented in Table 6.1. On the other side, the information required to perform efficiently the mission is provided by a ground station. Among the information that is provided, there are different requirements, localization and a basic path. However, the plane is able to define autonomously intermediate points in order to avoid any traffic or obstacles that would eventually not be defined by the operator at the ground station. Moreover, an embedded decision center unit allows the plane to land safely without having any information about the landing location. This requires numerous sensors, cameras and embedded technologies. A full description of each subsystem is defined in this report as well as an architecture that allows the plane to reach this level of autonomous flight.





Task	Embedded functionality	Autonomous control
Stabilization	Flight control	Actuators control
Piloting	Automatic pilot	Attitude control
Guidance	Trajectory planning	Trajectory control
Navigation	Path planning	Path definition
Strategy	Action planning	Mission

**Table 6.1:** Autonomous tasks presentation.

## 6.5 Stabilization and piloting

Currently, every commercial aircraft is equipped with an electronic autonomous stabilizer that is activated as the automatic pilot is engaged. In the particular case of the Duckampus system design, it consists in the motion of control surfaces during cruise and the control of the main engines power, but also the balance of the four AC motors during hovering configurations.

This aspect of autonomous flight requires a full system of actuators and a central unit that is able to control them individually. It also requires a description of its attitude in 3D thanks to a set of gyroscopes that will be defined later.

## 6.6 Navigation and guidance

Unmanned aircraft navigation is achieved using a Global Positioning System. The aircraft's position is then sent to the decision center which corrects the trajectory by changing the attitude in order to follow the path. The desired path is known from the mission, but can be temporarily changed or adapted for general safety reasons.

## 6.7 Takeoff and landing requirements

Takeoff and landing are the most critical phases of the flight in terms of autonomy. In particular, the landing phase requires the biggest amount of information. The autonomous system is thus designed considering this crucial phase.

Autonomous landing of unmanned vehicles has already been achieved using two methods. The first method consists in a landing on a site equipped with differential GPS guidance systems [43]. Landing can be carried out safely and automatically but it requires ground equipment and can thus not be performed everywhere [44]. Emergency landings are impossible with this system.

In addition to this, researchers demonstrated autonomous landing capability at an unknown site using only video cameras [45]. This system can be used for emergency situations.





These two systems are complementary and allow precise landing at equipped sites as well as emergency landing in the case of any unexpected failure of the airplane. The combined systems require a set of video cameras and a full GPS navigation system. As observed in the Tesla equipment, a set of ultrasonic sensors will also be required as complementary system to the video cameras. The aircraft will thus be completely operational with any weather conditions, using weather sensors.

## 6.8 Flight requirements

Traditional external equipment such as Pitot tubes and static pressure taps are necessary in order to compute the True Air Speed and the altitude. In addition, a set of gyroscopes are mandatory for the stability of the aircraft.

For safety reasons, redundancy of the equipment must be imposed. In this way, two sets of three gyroscopes and two sets of Pitot tubes/static pressure intakes are placed on the Duckampus.

## 6.9 Safety equipment

As an autonomous aircraft is integrated in traditional air traffic, it has to be equipped with the traditional avionics systems. In particular, a transponder allows the air traffic controller to collect information about the aircraft. With the "Sierra" mode<sup>2</sup> that is nowadays mandatory on all aircraft, the identification as well as the pressure-altitude data are directly sent to the air traffic ground base.

In addition to this, an Airborne Collision Avoidance System is essential. This equipment operates independently of the ground base and is essential in emergency situations. In case of imminent collision with another aircraft, this system will maneuver the aircraft in order to reduce the collision risks as much as possible.

A large set of sensors has to be used in order to detect any failure of a system or a malfunction. For example, a continuous mapping of the charge of the batteries must be sent to the decision center. A failure in the discharge would then be detected and a safe emergency landing could be performed in the best conditions.

## 6.10 Communication module

Mission information must be sent to the autonomous system through an external telecommunication module. Landing location, weather conditions, changes in the schedule or air traffic information are some examples of information that would be sent to the aircraft. As a reminder, the decisional autonomous aircraft that was chosen is able to operate without any human help, but it still requires mission information.

---

<sup>2</sup>Secondary surveillance radar process that allows selective interrogation of aircraft according to the unique 24-bit address assigned to each aircraft (also known as mode S of a transponder.)





In addition, an aircraft that flies in a controlled airspace must execute the orders of the air traffic controller. In this way, a communication link between the autonomous system and the controller must be maintained. Note that this constraint is one of the biggest challenges for autonomous aircraft.

## 6.11 Embedded systems

An autonomous aircraft requires a decision center that calculates the priorities and operates in order to ensure a safe and efficient flight. It has to manage inputs coming from the avionics and from the receiver and establish a strategy. From this, it will define a relevant path and adapt the trajectory of the aircraft on this path. To do so, it must control the actuators in order to change the attitude of the airplane. All these decisions are taken by an embedded system that is designed for this purpose. It is linked to the other parts by the bus. The architecture is given in the next section.

## 6.12 Architecture

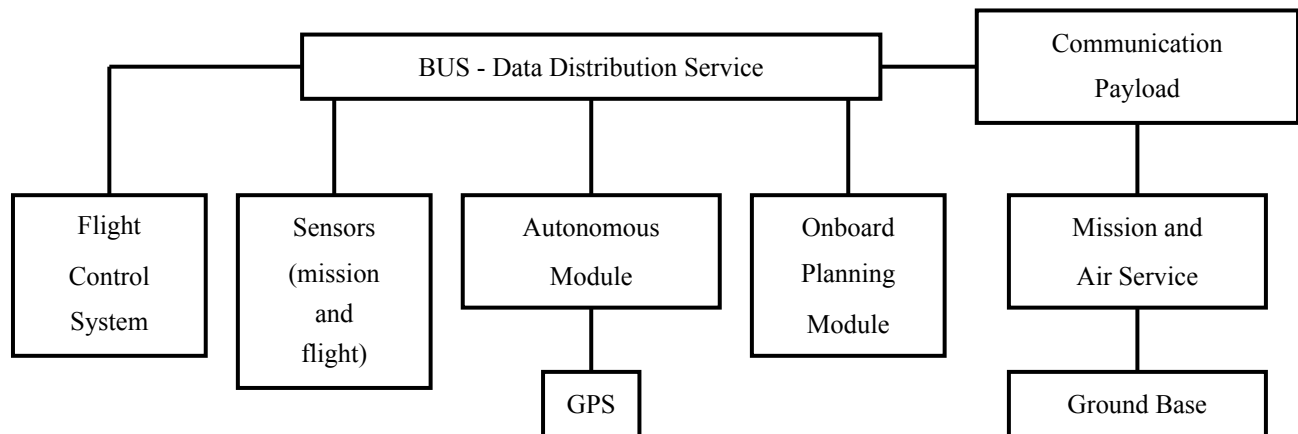


Figure 6.1: Architecture design of the autonomous system.

# 7 Trade-off study

The aim of this section is to alter parameters in order to study other configurations in terms of mass, battery requirements and stability. To that end, an increase and a decrease by about 10% are carried out in parameters. However, all quantities are not modified but this study is only restricted in 3 major aspects:

- The distribution of lift produced by the wing and the canard;
- The diameter of the propellers  $d_{prop}$ ;
- The distance between the canard and the main wing  $l_{c-w}$ .







For the sake of simplicity, the trade-off study is performed with four passengers, as it is the most likely to occur.

	Mass [lb]		Stability [%]
	Total	Batteries	Static margin
Initial	4263	500	9.64
Wing lift -10%	+0.73%	+0.63%	- 4.6
Wing lift +10%	-0.61%	+0.23%	22.07
$d_{prop}$ -10%	+0.3%	+2.33%	9.33
$d_{prop}$ +10%	-0.24%	-1.87%	9.9
$l_{c-w}$ - 10%	-0.01%	-0.13%	15.63
$l_{c-w}$ + 10%	-0.03%	-0.22%	23.7

**Table 7.1: Trade-off results.**

Firstly, Table 7.1 shows that the variation of lift has an impact on every result. Indeed, a decrease by 10% in the lift produced by the wing leads to an unstable configuration. This is due to the reduction of the wing mass and to the increase in the mass of the canard which will move the CG forward. On the other hand, an increase by 10% in the wing lift provides a configuration that is "too stable", which is not recommended for the aircraft since the equilibrium moment is too significant and will lead to an overshoot of the original state.

Concerning the propellers, the trade-off study reveals that the variation of the diameter impacts mostly the weight. Hence, by diminishing their diameter by 10%, the propellers require more power in order to provide the same thrust, which leads to an increase in the mass of the batteries. That also accounts for the growth (resp. diminishing) in the total mass of the aircraft by a decrease (resp. an increase) in diameters of the propellers. Moreover, the trade-off study highlighted that the configuration remains stable for both increasing and decreasing diameter. This is logical since the influence of the propeller is not taken into account when computing the stability.

For the last part of the trade-off study, when the wing is brought closer to the canard, the influence of the canard on the wing is more important. The perturbation of the air flow behind the canard induces a loss of lift produced by the wing, leading to a decrease in mass. Moreover, bringing the wing closer to the canard moves the CG forward which leads to an increase in the static margin.

## 7.1 Combinations of modifications

Up to this point, only one design parameter has been altered. In order to identify potentially better configurations, combinations of modifications are explored. After combining every parameter with another, two relevant combinations are retained and are depicted in Table 7.2. Finally, a last combination is computed where the three available parameters are modified in the aim of coming up with a structure that weights less and that remains stable.





Combination	Weight modification	Static margin
$d_{prop}$ : +10% & $l_{c-w}$ : -6%	-0.25%	13.49%
Wing lift : +3.6% & $d_{prop}$ : +10%	-0.47%	14.52%
Wing lift : +3.9% & $d_{prop}$ : +10% & $l_{c-w}$ : +10%	-0.6%	13.53%

**Table 7.2:** Combination of parameters for which some weight is saved.

From the results displayed in Table 7.2, it can be noticed that some configurations are, at a first glance, better than the baseline design since they are less heavy and stable. However, they all require an increase in the diameter of the propellers. And this is the main concern since there are some geometrical limitations that prevent such an increase.

In conclusion, the trade-off study allows to confirm the choices made about three major factors of the design. Concerning the wing lift and the distance between the wing and the canard, the study confirms that our configuration is well-chosen, as a variation of  $\pm 10\%$  pushes the design outside the recommended range of stability [5-15].

## 8 Cost analysis

The aircraft is now conceived but the design process is not over yet. Indeed, it is still needed to determine if the aircraft is worth the effort and cost to manufacture. This is why a cost analysis is performed in this section.

The methodology developed hereinafter to estimate the production and operating costs of the aircraft is based on the DAPCA-IV method [29]. It establishes special Cost Estimating Relationships (CERs), which are a set of statistical equations that predict aircraft acquisition costs using only basic information such as empty weight and maximum air-speed. These CERs are adjusted with a coefficient to consider the inflation of the dollar and represent its current value (2019).

### 8.1 Development and production costs

First of all, development and production costs of the Duckampus are assessed in order to determine the selling price in the next section. They are calculated considering a production of 500 aircraft over a 5-year period. This choice will be justified subsequently in the market study. Results for the non-recurring costs are displayed in Table 8.2. These values are estimations furnished by the DAPCA method and a more accurate cost model still needs to be built to account for the features of the Duckampus. That is why some changes are done regarding the method:

- To consider the use of electric motors, engine costs are determined based on comparable electric motors prices provided by *Siemens* [46]. \$20,000 (x2) and \$10,000 (x2) prices are retained for the back and for the front engines





respectively.

- Labor costs of engineers, tooling and manufacturing workers are computed for a factory located in the United States. The average wages are high compared to other countries but, as the aircraft is designed to meet FAA requirements, it is clear that the first factory will be built in the USA. In the future, other factories will be built in Asia, where lower wages are present and nearest to the biggest market, i.e. China.
- Material costs are calculated considering a whole airframe in composite materials, which increases drastically their price. Nevertheless, manufacturing and tooling costs are decreased by 30 % due to the fact that when dies are produced, less work is needed [47] and less material is used. Note that the main problem of manufacturing with composites, i.e. the time needed for production, is not problematic here as the production is assumed equal to 50 airplanes per annum.
- A product liability of 13.5 % is added, meaning that production costs are increased by this amount to consider potential additional costs.
- To consider the autonomous system required, costs of avionics are evaluated looking at component model prices (Table 8.1).

Item	Price	Function
Garmin - GTS 800 System	\$8,975	Active Traffic Surveillance
Garmin - GTX 335	\$2,589	ADS-B
SANDIA aerospace - SAC 7-35 Air Data Computer	\$2,439	Air Data
Garmin - G5 Electronic Flight Instrument	\$1,249	Attitude
Garmin - GA 35	\$353	GPS antenna
Garmin - GWX 75	\$18,889	Weather Radar
<b>Total avionics costs</b>	<b>\$34,494</b>	

**Table 8.1:** Avionics component model prices.

- Costs for the internal layout (seats, flooring, cooling, ...) are not considered by the DAPCA method and it is recommended from [29] that an amount of \$950 per passenger should be added. However, Duckampus designers are willing to offer optimal quality flights to their customers. In that way, the cabin has to provide sufficient comfort and luxury to the passengers. The Duckampus thus provides:
  - **WIFI connectivity** to stay in touch anytime, anywhere.
  - An **iPad** per passenger for in-flight entertainment. It allows to watch movies, go to the Internet, ... The clientele of the Duckampus no longer wastes time when they are on the move as these tablets enable the





organization of conference calls for business. An application will also be developed and installed on each iPad so that passengers can find information about the flight such as speed, altitude, moving map, . . .

- Four **transparent OLED screens** connected to the corresponding iPad for a high-quality display. The screens are transparent to let the passengers appreciate the view during flight when not using them.
- **USB ports** and **plugs** to recharge the client phones during the flight.
- A **PAC** to cool down the cabin by times of hot temperatures.

The cost for these items is evaluated to \$21,951.

- Costs of engines, propellers, batteries and entertainments options are considered with their current prices on the market and must thus be lowered by a factor to acknowledge the increased experience of technicians with the production and time.

	Cost per unit		Cost per unit
	(in thousand \$)		(in thousand \$)
Engineering	52.16	Materials/equipment	68.85
Development support	3.48	Engines	8.11
Flight test operations	0.16	Propellers	1.91
Tooling	44.79	Batteries	1.23
Manufacturing labor	224.78	Avionics	4.67
Quality control	58.44	Entertainment	3.48
Product liability	68.433	<b>PRODUCTION COSTS</b>	<b>540.383</b>

**Table 8.2:** Non-recurring costs per aircraft calculated for a production of 500 Duckampus over 5 years.

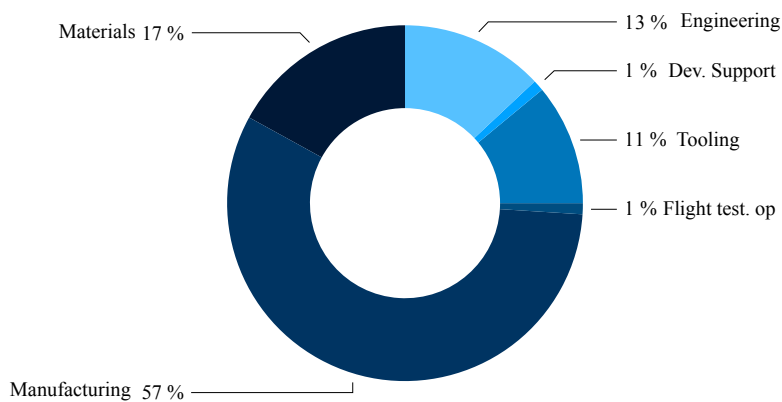


**Figure 8.1:** Proportion of non-recurring costs for the production of 500 Duckampus.





## 8.2 Determination of a selling price

The aim of this section is to determine the optimal price at which the EVTOL will be sold. It is assumed in the current section that the objective is the maximization of profits.

Three different pricing strategies are compared and the higher price will be taken as a final price:

- Competitive analysis
- Cost-based pricing
- Price-based costing

The first strategy is the **competitive analysis**. As no other existing solutions are present on the market. A market analysis and comparison to competitors is thus impossible in this case.

The second strategy, the **cost-based pricing**, consists of adding all the costs calculated in Section 8.1 and add a profit to it. As the AIAA proposal required 15 % of margin. The price will be

$$\text{Price} = \text{Cost} + 15\% \text{ margin} = \$540,383 \times 1.15 = \$621,441$$

This pricing strategy, even if, at first sight looks very simple, leads to non optimal prices. Most American and practically all European companies use this strategy to arrive at their prices. However, as soon as the product is introduced in the market, they have to start cutting the price, redesign components at enormous expenses and finally take losses of dropping a perfectly good product because it is priced incorrectly. Also, if costs suddenly grow up by more than your current margin, you will become unprofitable, and two choices will remain: stop selling your products or increase your price, at the expense of your market share.

The third strategy is the **price-based costing**, also known as **value pricing**, for which the client's willingness to pay for the product is assessed. An optimal price will lead to improvements in profitability through higher prices without having any influence on sales volumes. This strategy is the optimal one in this case as the Duckampus will enter on a niche market, where the Duckampus is designed to satisfy market needs, such as an environmentally-friendly, autonomous mean of transportation and a way to prevent traffic jams.

Moreover, the Duckampus is a breakthrough in the future of eco-mobility, using cutting-edge technologies. Its fast implementation plan (see Fig. 8.2) will enable the Duckampus company to enter among the firsts on the market. Henceforth, the first mover advantage can be optimally used in order to maximize profits.



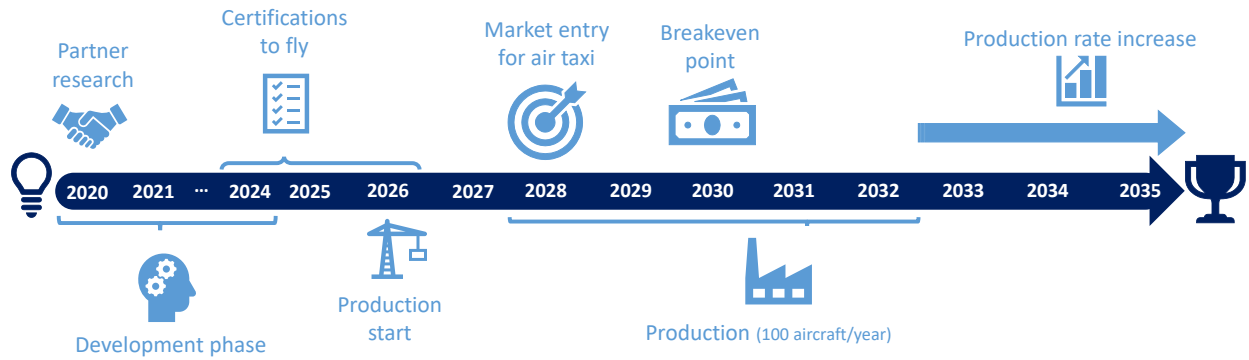


**Figure 8.2:** Duckampus go-to-market timeline.

To assess the willingness to pay of the buyer, let us assume that our main clients will be privately held companies (such as Uber) located in several cities that have a large amount of inhabitants and a high average level of revenues. Let us put our shoes in the client side to see what will be their sources of revenues and costs. First, on the revenues side, the only source retained here will be the transportation of passengers. However, additional sources of revenues could be mentioned such as public funding, publicity inside the aircraft, aerial publicity, cargo transportation, medical transportation,... A comparison of different transportation means currently existing is realized in Table 8.3.

Transportation means are compared using two different routes inside New York City. In addition to purely transit means, the Duckampus can take market share in the tourist helicopter market. Thus, this is also assessed.

Itinerary route	Transportation Mean	Distance Travelled [mi]	Time [min]	Price
JFK Airport → Times Square	Bike	16	96	\$0
	Public Transport	17.3	57	\$12.25-\$15/person
	Uber X	16	45-80	\$61/car
	Helicopter	13	8-12	\$950/person
	<b>Duckampus</b>	<b>13</b>	<b>16<sup>3</sup></b>	<b>\$59.5/person</b>
North Central Park → Battery Park	Bike	9.1	46	\$0
	Public Transport	10.4	38	\$2.75 /person
	Uber X	10	60	\$80/car
	<b>Duckampus</b>	<b>9</b>	<b>14.6<sup>3</sup></b>	<b>\$53.5/person</b>
Tourist Round Trip	Helicopter	≈ 45	25	\$380/person
	<b>Duckampus</b>	<b>≈ 45</b>	<b>29</b>	<b>\$107.5/person</b>

**Table 8.3:** Analysis of the time and cost of typical transportation means in New-York.

The bike and public transports are the cheapest transportation means, but have less convenience. Our service is de-

<sup>3</sup>Including 5 minutes boarding and 5 minutes unboarding.





signed for high-end customers, for whom the convenience is really a key to buy when choosing a transportation mean. One main advantage of an EVTOL with comparison to other transports is the reduction of time and independence of the transit time with respect to the period of the day, e.g. no additional time during peak hours. One can assure that, due to the gain of time, high-end customers are willing to pay more than for a taxi or a Uber. However, the price should be quite low to attract more people. Comparing mainly with a Uber, the price of the ticket is fixed to \$100 for a typical economical mission of 40 miles. For other distances, the fixed fee is \$40 per trip, with a variable fee of \$1.5 per additional mile, based on taxi fare principle. Fixed routes will be created between vertiports and air traffic management will be optimize to gather people that make similar routes. For comparison, taxis in New-York have a starting fee of \$2 and an extra expense of \$2 per additional mile.

Here, a fixed ticket pricing was chosen for the sake of simplicity. However, a next step for an operator will be to implement a dynamic ticket pricing. With this option, the price of a journey is adjusted according to the demand. In this case, the main challenge is to evaluate the market in real time. For instance, Fig. 8.3 presents a projection of what could be the price of a ticket throughout a week day (the curve should be adapted for week-ends) where prices are at their highest during peak hours. This strategy should really be adopted as it has the advantage to promote the Duckampus to the middle class during off-peak periods with more attractive prices. Dynamic ticket pricing is thus a first step towards the growth of the market.

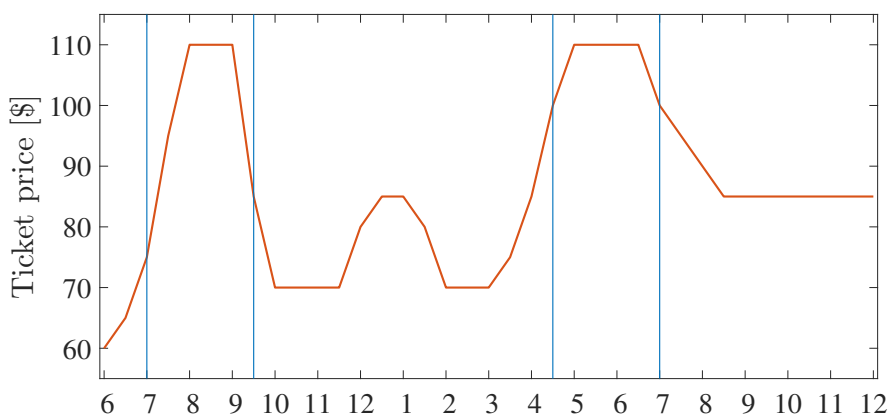


**Figure 8.3:** Example of dynamic ticket pricing adapted for a week day in a city similar to New-York.





It is almost certain that a lot of people will choose Duckampus as a new mobility mean with a great convenience as they only need to choose the destination. And then they just have to enjoy the experience and the breathless view on the top of cities.

In New-York, the average speed of a car is about 17.6 mph and the route only needs to exceed 7.5 miles for the Duckampus to be faster. The comparison of the timeline of a typical journey is presented in Fig. 8.4.

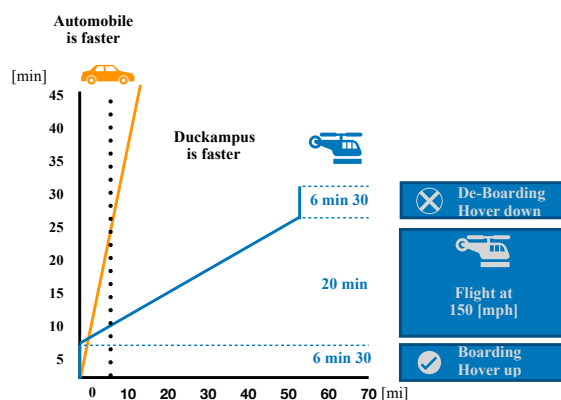


**Figure 8.4:** Comparison of a typical journey with a car and the Duckampus.

According to a Porsche consulting study [48], 500 EVTOLs will be in service by 2025, with a CAGR of about 32 %, leading to 2,000 in service by 2030. A reasonable assumption is thus to take 25 % of market shares and so, a number of 500 airplanes. Most of the demand will come from the United States, Asia and Middle East countries. Due to the high number of flights and quick technological improvements, the demand for new EVTOLs and replacements of existing ones will be high in the next few years.

### 8.3 Trip cost

For the economical mission, the total time for the passenger experience (including boarding and unboarding of 5 minutes each) is 28 minutes, for a trip of 40 statute miles. The time needed to charge the battery is 9 minutes <sup>4</sup> based on cutting-edge existing technologies. The in-flight time is less than 50 % of the time of a full cycle. It is assumed that the aircraft is used from 6 A.M. to midnight (18 hours/day) and 300 operating days per year, when excluding bad weather days. As the total time of a full cycle from boarding to full charge is 37 minutes, we can reasonably assume that the plane averages one trip per hour. Eventually, this leads to a total of 2,700 flight-hours per year, which is very similar to what Uber is expecting [49].

Now, let us assess the costs of our client, the operating firm. Some vertiports need to be built to serve as main base and storing place for 5 EVTOLs. Other vertistops will be built, only for charging, take-off and landing places. These constructions are the main barrier in the construction of a network of places interconnected by Duckampus aircraft. Several assumptions need to be stated to drive the analysis:

- Each AEVTOL is replaced every 5 years

<sup>4</sup>Assuming a charging power of 450 kW [50]







- Each vertiports costs \$4M
- There are 5 planes per vertiports
- Each plane has a charging device, which costs \$100k
- The cost of electricity is \$0.13 per kWh, based on the 2019 US Price for electricity. Note that other targeted markets such as Asia and Middle East have lower fares of electricity [51].
- Air traffic management (ATM) cost are 6 % of total cost
- SG& A (Selling, General & Administrative Expenses) costs account for 10 % of total cost
- Insurance costs are computed using a flat rate of \$500 and a variable part of 1.5 % of the production cost
- Labor cost on the vertiports account for 10 % of total cost
- Engine overhaul fund, Maintenance and storage costs were determined using the DAPCA method

The annual costs per unit aircraft are presented in Table 8.4.

	Annual cost per unit aircraft		Annual cost per unit aircraft
Maintenance	\$42.93k	Labor cost	\$14.3k
Storage	\$3k	Air traffic management	\$21.45k
Electric energy consumption	\$42k	Marketing	\$35.75k
Battery replacement	\$98k	SG&A	\$35.75k
Engine Overhaul Fund	\$54k	Insurance	\$9.82k
Inspection cost	\$500	<b>Operating Costs</b>	<b>\$357.534k</b>

**Table 8.4:** Operating costs per year.

Finally, the cost per hour of flight is \$132.42. The price is chosen per person instead of price per trip as the traffic management will be done such that people going to the same place will be gathered. On average, it is assumed that 3 people will travel on average per plane. However, as the price for a typical mission that occurs one per hour is less than the price of the ticket of a lonely passenger, the flight remains profitable. The management of the trips must not be underrated as it is really the key to make huge profits.

The price of the aircraft was chosen to have a margin for the operator of almost 50 %. In a competitive landscape, the best way to attract clients is to promise them a huge profit. Then, the price of the aircraft is chosen to \$1,500,000. All the costs are represented in the waterfall graph in Fig. 8.5, and are put into perspective with the associated revenues. The price of the aircraft can be seen as over-evaluated. However, as the Fig. 8.5 shows, the price of the aircraft is not





the main driver of the cost for the operating company. As the price of the battery is a key driver of cost, a partnership with a battery company can be seen as an additional source for profits.

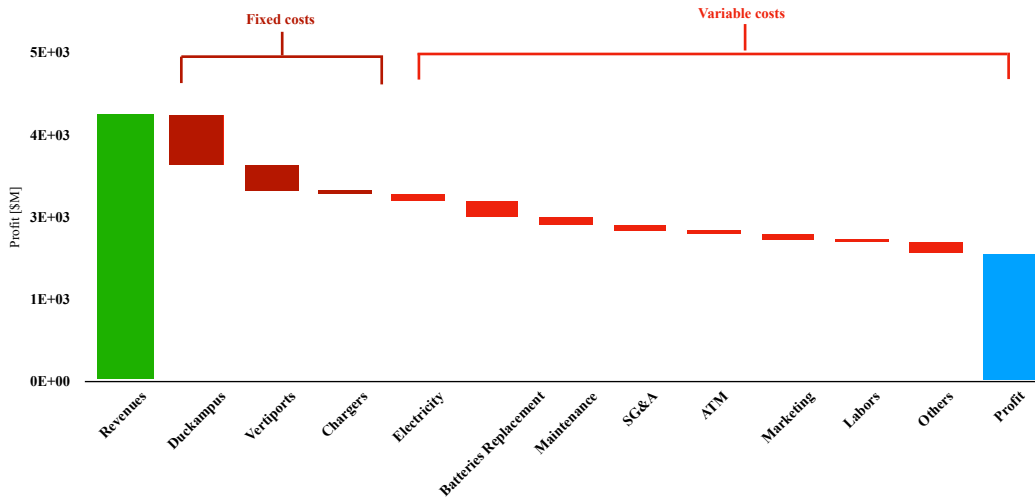


Figure 8.5: Waterfall graph of costs and revenues of the Duckampus.

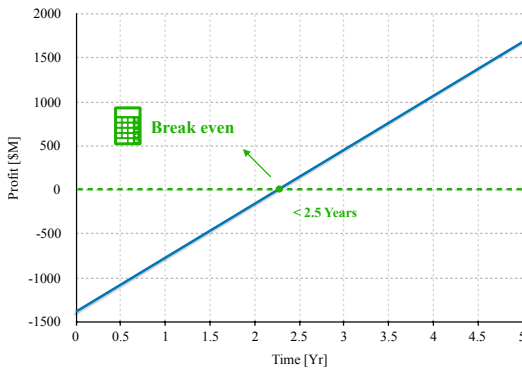
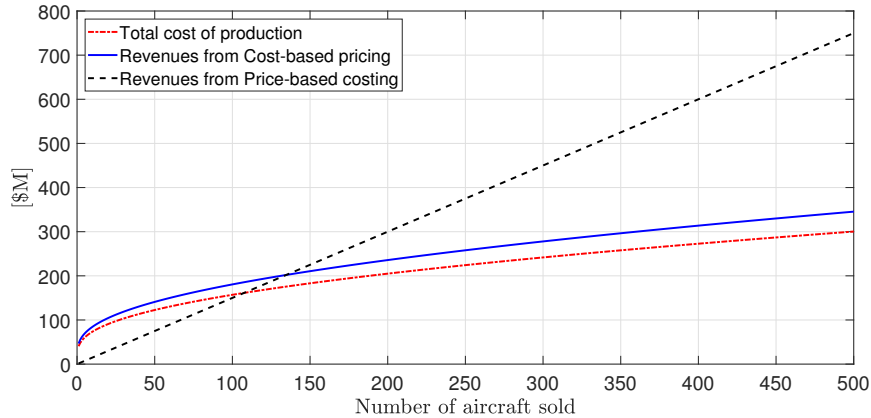


Figure 8.6: Profit analysis for the operator.

After less than 3 years, the company have break-even and finally, the total profit after 5 years is \$1.95B with an initial investment of \$1.2B. The initial investment is relatively high, especially for buying the aircraft and vertiports, meaning that the operating company need high investing capabilities and must be already well developed. However, the return on investment is relatively high and companies need to position on this market, in the dawn of a new mobility era.

Revenues obtained over 5 years with different pricing strategies are compared in Fig. 8.7. If the number of aircraft sold is lower than 150, meaning a market share of 7.5 %, the cost-based pricing is advantageous over the price-based costing. Over this bottom line, the profits are maximized using a selling price of \$1,500,000.





**Figure 8.7:** Comparison of revenues for different pricing strategies with respect to the number of aircraft sold over a 5-year period.

As it is assumed that Duckampus can capture 25 % of market share in the transportation EVTOL market between 2025 and 2030, the price-based costing is clearly the best way to determine the price of the aircraft. Moreover, value pricing is associated of a feeling of pride and belonging to a special brand, which is beneficial in a long-term view.

Price-based costing compels Duckampus to know well the clients and defines the right persona. With price sensitivity measurements and feature analysis you are only going to get approximations of the right pricing, packaging, and positioning for your product. In the good case, the price is underestimated and the product can be repriced higher to meet the willingness to pay of clients (quite aggressive pricing strategy). If the price was overestimated, the repricing does not affect the company as margin are quite high at the beginning.

*When price-based costing says “ here’s how these tools will help you”, cost based pricing says “here’s a bunch of tools—maybe they can help you” [52].*

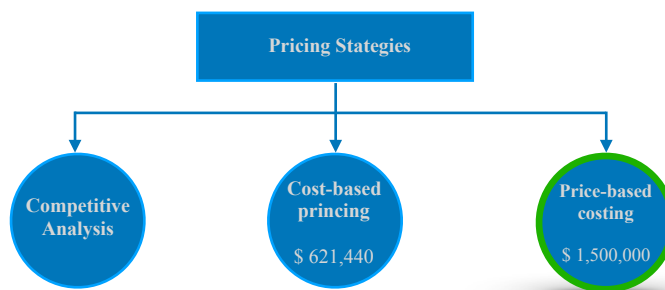


**Figure 8.8:** Decision tree of the pricing strategy.





## 8.4 Profit analysis

As the price of the aircraft and the cost of production are now both determined, a profit analysis is run and the profit margin is computed.

Selling price of the Duckampus	\$1,500,000
Cost of production of the Duckampus <sup>5</sup>	\$540,000
<hr/>	
Profit per Duckampus sold	\$960,000
<b>Profit for 500 Duckampus sold</b>	<b>\$ 480,000,000</b>

The margin can be computed from :

$$\text{Margin} = \frac{\text{Price} - \text{Cost}}{\text{Price}} = \frac{1,500,000 - 540,000}{1,500,000} = 64\% \text{ margin}$$

This amount is far beyond the bottom line of 15 % profit fixed by the AIAA proposal. This huge profit enable our company to decrease their price in case of a competitive landscape or to decrease the price when the number of command is increased. The money will be further reinvest for the development of a similar aircraft for private users at a more affordable price.

Clearly, with this pricing strategy and the long-term view of the market, Duckampus will position itself as a breakthrough in transportation and undoubtedly shape the future of the urban mobility.

---

<sup>5</sup>Based on 500 units sold





## 9 Conclusion

In answer to the request for proposal submitted by the American Institute of Aeronautics and Astronautics, the Duckteam, from the University of Liège, is very delighted to introduce the design of its autonomous electrical vertical takeoff and landing air taxi: the Duckampus. With reinvented design features and cutting-edge technologies, this EVTOL is not only an evolution in the urban mobility, it is a revolution!

In the next decades, the amount of EVTOL flying over large cities is expected to increase really fast. With the expansion of the urban air mobility, the Duckampus concept will undoubtedly be a reality in the nearest future.

New technologies such as tilt-wing, autonomous pilot, stall-proof configuration, lighter fast-charging batteries, vertical takeoff and landing to reduce spatial requirements, the Duckampus demonstrates optimal general performances. The full composite airframe reduces weight and decreases the manufacturing cost for an increased rate of production.

This new mean of transportation is an opportunity for operators. By meeting the requirements using a combination of ambitious but feasible technologies and by offering a very large revenue on investment to this operator, the Duckampus will be a very suitable option.

The Duckampus is dedicated to a premium quality air transportation. With an elegant design and a pleasant internal layout, passengers can enjoy a comfortable autonomous flight. The Duckampus prevents to be stuck in traffic jam, in a fully electric solution that is as affordable as a traditional Uber. Proposing a very safe journey and a gain of time to its passengers, this aircraft will shape the future in air mobility, as well as general urban mobility.

The next step of the Duckampus concept evolution is the continuation of the ongoing development phase, in parallel with the partner research. In a few years, flight tests will be carried out and the process will end with the certification of the aircraft. In term of development, the detail design phase would be following the conceptual and preliminary design stages developed in this report. From there, the next part will be the beginning of production, followed by the market entry. In a long term perspective, the huge profits generated from the selling of this aircraft will enable the company to significantly increase the cash flow that will be reinvested in the development of a more affordable solution for individuals.





## References

- [1] INRIX, “2018 global traffic scorecard.” <https://inrix.com/scorecard/>, 2018.
- [2] F. A. Administration, “Small airplanes regulations, policies and guidance.” [https://www.faa.gov/aircraft/air\\_cert/design\\_approvals/small\\_airplanes/small\\_airplanes\\_regs/](https://www.faa.gov/aircraft/air_cert/design_approvals/small_airplanes/small_airplanes_regs/).
- [3] A. technology, “Lilium jet engine and performance details.” <https://www.aerospace-technology.com/projects/lilium-jet/>.
- [4] T. V. F. Society, “Rotorcraft handling qualities.” <https://vtol.org/events/rotorcraft-handling-qualities>, 2017.
- [5] T. E.-U. I. A. S. Conference, “Erica - the european tiltrotor,” 2005.
- [6] E. Fradenburgh, “Variable length blade.” <https://patents.google.com/patent/US3768923A/en>, 1973.
- [7] J. A. W. Mark H. Dawson, “Fast-forwarding to a future of on-demand urban air transportation.” <https://patents.google.com/patent/US6902370B2/en>, 2005.
- [8] E. A. F. U. A. Corporation, *DYNAMIC MODEL WIND TUNNEL TESTS OF A VARIABLE-DIAMETER TELESCOPING-BLADE ROTOR SYSTEM (TRAC ROTOR)*. National Technical Information Service (U.S. Department of commerce), 1973.
- [9] L. Noels, “Lecture slides: Conceptual design,apri0004-1 aerospace design project,” 2018.
- [10] J. D. A. Jr., *Introduction to flight, 7th edition*. McGraw-Hill International Edition, 2012.
- [11] J. Stack, “Tests of airfoils designed to delay the compressibility burble,” *National Advisory Committee for Aeronautics*, 1943.
- [12] A. Manchin, W. Lafta, and D. V. Dao, “Smart variable pitch propeller system for unmanned aeria vehicles,” *International Journal of Engineering and Technology*, pp. 5238 – 5242, 10 2018.
- [13] P. L. Daan Moreels, “White paper magnax axial flux machines,” V1.9 Nov 2018.
- [14] M. Delgado Gosalvez, J. Van Ham, S. Joosten, D. Juschus, G. Nieuwerth, T. Pelt, L. Smit, M. Takken, Y. Wang, T. Ziere, F. Leverone, P. Groen, and M. Delgado Schwartz, “The greenliner, green flying final report dse group 8,” tech. rep., 07 2018.
- [15] FramoMorat, “Planetary gears.” <https://framo-morat.com/products/planetary-gears/>, 2019.





- [16] C. Jung, “Power up with 800-v systems: The benefits of upgrading voltage power for battery-electric passenger vehicles,” *IEEE Electrification Magazine*, vol. 5, pp. 53–58, 2017.
- [17] R. Semiconductor, “Rohm’s latest sic technology achieves excellent performance for electric vehicles,” July 13, 2018.
- [18] S. Schulz, “Exploring the high-power inverter: Reviewing critical design elements for electric vehicle applications,” *IEEE Electrification Magazine*, vol. 5, pp. 28–35, 2017.
- [19] E. V. G. Ortolani, *Manuale di Elettrotecnica e Automazione, seconda edizione*. Hoepli, 2014.
- [20] L. T. C. Spa, “Fg70r-0,6/1 kv,” tech. rep., January 23, 2018.
- [21] D. Eroglu, K. R. Zavadil, and K. G. Gallagher, “Critical link between materials chemistry and cell-level design for high energy density and low cost lithium-sulfur transportation battery,” *Journal of the Electrochemical Society*, vol. 162, pp. A982–A990, 02 2015.
- [22] C. Y. Nagata Hiroshi, “A lithium sulfur battery with high power density,” *Journal of Power Sources*, p. 206–210, 10 2014.
- [23] A. Fotouhi, D. J. Auger, L. O’Neill, T. Cleaver, and S. Walus, “Lithium-sulfur battery technology readiness and applications—a review,” *Energies*, vol. 10, p. 1937, 11 2017.
- [24] G. Li, X. Wang, M. H. Seo, M. Li, L. Ma, Y. Yuan, T. Wu, A. Yu, S. Wang, J. Lu, and Z. Chen, “Chemisorption of polysulfides through redox reactions with organic molecules for lithium-sulfur batteries,” *Nature Communications*, vol. 9, 12 2018.
- [25] S. Hoerner, *Fluid-Dynamic Drag: theoretical, experimental and statistical information*. 1965.
- [26] E. Torenbeek, *Advanced aircraft design*. 2013.
- [27] A. E. v. d. H. Abbott and J. Louis S. Stivers, *National advisory committee for aeronautics*. AIAA Education Series, Reston, VA, 1945.
- [28] S. Gudmundsson, *General aviation aircraft design: applied methods and procedures*. Butterworth-Heinemann, 2014.
- [29] D. P. Raymer, *Aircraft Design: A Conceptual Approach*. AIAA Education Series, Reston, 2012.
- [30] R. F. S.RanaR, “Advanced composites in aerospace engineering.” <https://www.sciencedirect.com/science/article/pii/B9780081000373000018>, 2016.
- [31] M. F. Ashby, “Ces edupack,” July, 2018.





- [32] A. P. Mouritz, *Introduction to Aerospace Materials*. Woodhead Publishing, 2012.
- [33] Extruco, "Aircraft extrusion." <https://extruco.com/>, April, 2018.
- [34] S. Gudmundsson, "Design of canard aircraft." [https://booksite.elsevier.com/9780123973085/content/APP-C2-DESIGN\\_OF\\_CANARD\\_AIRCRAFT.pdf](https://booksite.elsevier.com/9780123973085/content/APP-C2-DESIGN_OF_CANARD_AIRCRAFT.pdf), 2013.
- [35] P. D. C. P. for the Aeronautical Engineer, "Usaf stability and control datcom." <http://www.pdas.com/datcomTable1.html>.
- [36] H. Thomas, *Estimation of stability derivatives*. Ministry of aviation London, 1963.
- [37] U. Military, "Military specification : Flying qualities of piloted airplanes," 1969.
- [38] A. Chaitanya G Rothea, *Design and Analysis of Composite Material Drive Shaft*. International Journal of Innovative and Emerging Research in Engineering, 2015.
- [39] Boeing, "Meda investigation process." [http://www.boeing.com/commercial/aeromagazine/articles/qtr\\_2\\_07/article\\_03\\_2.html](http://www.boeing.com/commercial/aeromagazine/articles/qtr_2_07/article_03_2.html).
- [40] A. Reports, "Autonomous aircraft market - global forecast 2030." <https://www.asdreports.com/market-research-report-482553/autonomous-aircraft-market-global-forecast>.
- [41] P. E. Aviation, "What do airline pilots earn?." <https://www.pea.com/airline-pilot-salary/>.
- [42] Tesla, "Autopilot." [https://www.tesla.com/fr\\_BE/autopilot?redirect=no](https://www.tesla.com/fr_BE/autopilot?redirect=no).
- [43] R. Collins, *Athena 311 Integrated Flight Control System*. MicroPilot,.
- [44] E. navipedia, "Ground-based augmentation system." [https://gssc.esa.int/navipedia/index.php/Ground-Based\\_Augmentation\\_System\\_\(GBAS\)](https://gssc.esa.int/navipedia/index.php/Ground-Based_Augmentation_System_(GBAS)).
- [45] M. C. Paul Williams, *INTELLIGENT LANDING SYSTEM FOR LANDING UAVS AT UNSURVEYED AIRFIELDS*. BAE Systems Australia, 2012.
- [46] S. AG, "Simotics low-voltage motors," 2015.
- [47] R. K. P. Shama Rao N., Simha T. G. A. and R. K. G. V. V., "Carbon composites are becoming competitive and cost effective." <https://www.infosys.com/engineering-services/white-papers/Documents/carbon-composites-cost-effective.pdf>, 2018.
- [48] P. Consulting, "The future of vertical mobility: Sizing the market for passenger, inspection, and goods services until 2035." <https://fedotov.co/wp-content/uploads/2018/03/Future-of-Vertical-Mobility.pdf>, 2018.







- [49] U. Elevate, “Fast-forwarding to a future of on-demand urban air transportation.” [http://www.boeing.com/commercial/aeromagazine/articles/qtr\\_2\\_07/article\\_03\\_2.html](http://www.boeing.com/commercial/aeromagazine/articles/qtr_2_07/article_03_2.html), 2016.
- [50] Y. Möller, “Moniteur automobile belge : Porsche et bmw dévoilent un chargeur rapide de 450 kw... et le taycan cross turismo.” <https://www.moniteurautomobile.be/actu-auto/innovation/porsche-bmw-fastcharge.html>, 12/16/2018.
- [51] Statista, “Global electricity prices in 2018, by select country.” <https://www.statista.com/statistics/263492/electricity-prices-in-selected-countries/>, 2018.
- [52] J. Locke, “Value pricing vs cost based pricing.” <https://www.lockedownseo.com/value-pricing-vs-cost-based-pricing/>, 2019.

